Government of **Western Australia**
Department of **Mines, Industry Regulation and Safety**

RECORD 2018/4

A NEW MESOPROTEROZOIC MAFIC INTRUSIVE EVENT IN THE CAPRICORN OROGEN

by
OA Blay, SP Johnson, MTD Wingate, AM Thorne, CL Kirkland, SG Tessalina, and HN Cutten

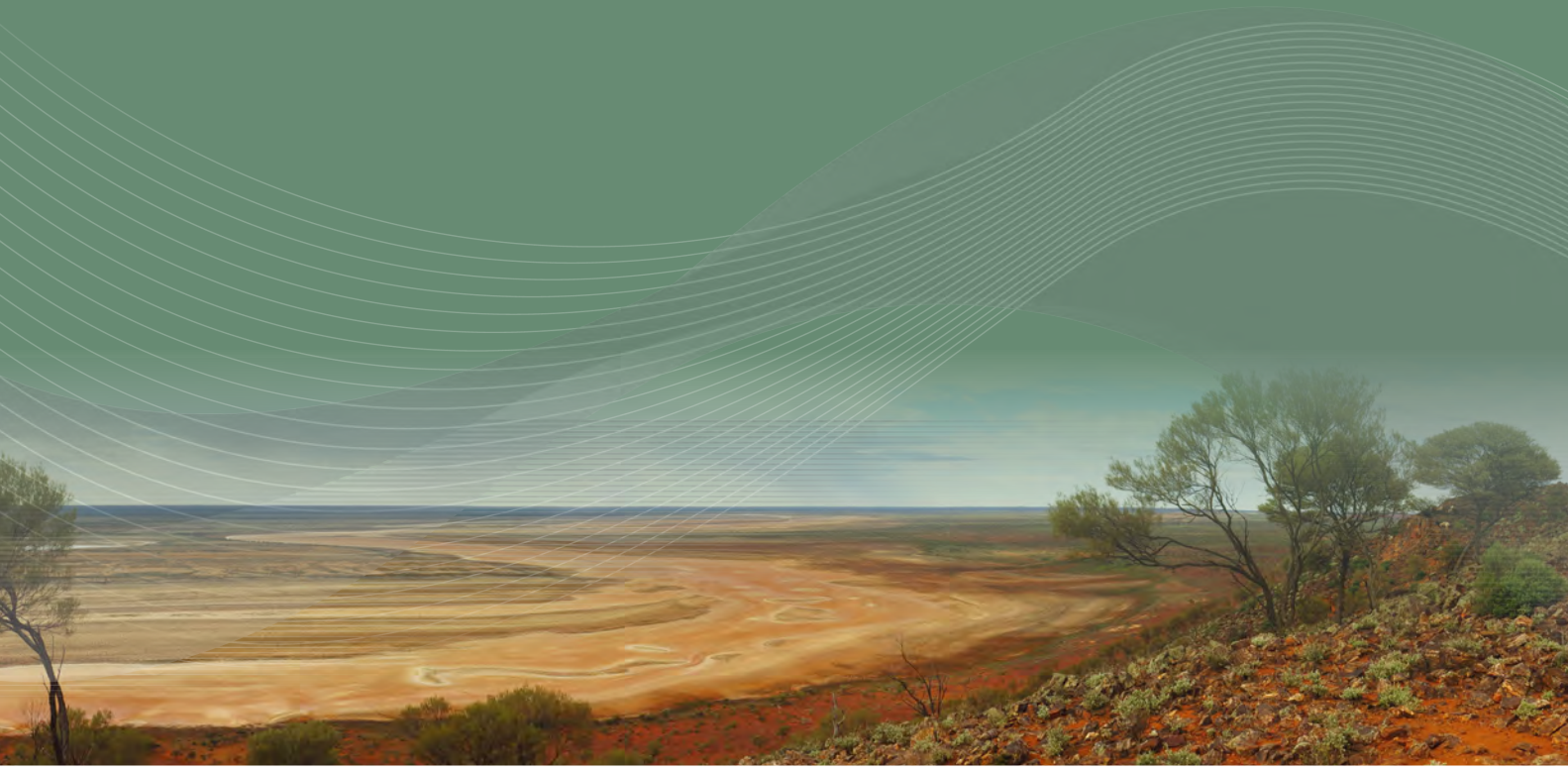

Geological Survey of Western Australia

John de Laeter Centre

EIS EXPLORATION INCENTIVE SCHEME

GEMOC

CCFS

Government of **Western Australia**
Department of **Mines, Industry Regulation and Safety**

RECORD 2018/4

A NEW MESOPROTEROZOIC MAFIC INTRUSIVE EVENT IN THE CAPRICORN OROGEN

by
OA Blay, SP Johnson, MTD Wingate, AM Thorne, CL Kirkland[1], SG Tessalina[2], and HN Cutten

1 Centre for Exploration Targeting (CET), Curtin Node, School of Earth and Planetary Sciences, Curtin University, Bentley WA 6845

2 John de Laeter Centre, Faculty of Science and Engineering, Curtin University, Bentley WA 6845

PERTH 2018

Geological Survey of Western Australia

MINISTER FOR MINES AND PETROLEUM
Hon Bill Johnston MLA

DIRECTOR GENERAL, DEPARTMENT OF MINES, INDUSTRY REGULATION AND SAFETY
David Smith

EXECUTIVE DIRECTOR, GEOSCIENCE AND RESOURCE STRATEGY
Jeff Haworth

REFERENCE
The recommended reference for this publication is:
Blay, OA, Johnson, SP, Wingate, MTD, Thorne, AM, Kirkland, CL, Tessalina SG and Cutten HN 2018, A new Mesoproterozoic mafic intrusive event in the Capricorn Orogen: Geological Survey of Western Australia, Record 2018/4, 41p.

ISBN 978-1-74168-794-1

Grid references in this publication refer to the Geocentric Datum of Australia 1994 (GDA94). Locations mentioned in the text are referenced using Map Grid Australia (MGA) coordinates, Zone 50. All locations are quoted to at least the nearest 100 m.

John de Laeter Centre
EXPLORATION INCENTIVE SCHEME
GEMOC
CCFS

U–Pb measurements were conducted using the SHRIMP II ion microprobes at the John de Laeter Centre, Curtin University, operated with the financial support of the Australian Research Council and Auscope NCRIS. Isotope analyses were funded in part by the Western Australian Government Exploration Incentive Scheme (EIS). Lu–Hf measurements were conducted using LA-ICPMS at the ARC National Key Centre for Geochemical Evolution and Metallogeny of Continents (GEMOC), via the ARC Centre of Excellence in Core to Crust Fluid Systems (CCFS), based in the Department of Earth and Planetary Sciences at Macquarie University, Australia.

Published 2018 by the Geological Survey of Western Australia
This Record is published in digital format (PDF) and is available online at <www.dmp.wa.gov.au/GSWApublications>.

Further details of geological products and maps produced by the Geological Survey of Western Australia are available from:
Information Centre
Department of Mines, Industry Regulation and Safety
100 Plain Street
EAST PERTH WESTERN AUSTRALIA 6004
Telephone: +61 8 9222 3459 Facsimile: +61 8 9222 3444
www.dmp.wa.gov.au/GSWApublications

Cover image: Elongate salt lake on the Yilgarn Craton — part of the Moore–Monger paleovalley — here viewed from the top of Wownaminya Hill, 20 km southeast of Yalgoo, Murchison Goldfields. Photograph by I Zibra, Geological Survey of Western Australia

Contents

Appendices

Figures

Tables

A new Mesoproterozoic mafic intrusive event in the Capricorn Orogen

by

OA Blay, SP Johnson, MTD Wingate, AM Thorne, CL Kirkland[1], SG Tessalina[2], and HN Cutten

Abstract

Geochronology, field observations, petrography and geochemistry of Proterozoic dolerite sills in the Capricorn Orogen reveal a new suite of sills: the 1514–1505 Ma Waldburg Dolerite. The new data also refine the ages of the previously recognized 1465–1450 Ma Narimbunna Dolerite and the 1083–1075 Ma Kulkatharra Dolerite. For each dolerite suite, the isotopic ages include a significantly older or younger outlier, which implies that some sills in each suite intruded at different times. Waldburg Dolerite sills were emplaced in a structural corridor between two major crust-cutting faults: the Lyons River Fault and the Ti Tree Shear Zone. The Waldburg Dolerite has distinctive geochemical characteristics, including low concentrations in most rare earth elements (REE), high field strength elements (HFSE) and weakly fractionated REE. Sm–Nd and Lu–Hf isotopes indicate that the Waldburg Dolerite was derived from a radiogenic source similar to depleted mantle, but which also underwent minor interaction with evolved (unradiogenic) crustal material. A low degree of crustal contamination is also indicated by the weak correlation between $\varepsilon_{Nd(i)}$ and SiO_2, $(La/Sm)_{CN}$, Mg#, and Nb/La. The geochemistry and isotope compositions of the mafic rocks show that the Waldburg, Narimbunna and Kulkatharra Dolerites were sourced from similar, relatively shallow, depths within a heterogeneously subduction-modified lithospheric mantle. Differences in the petrographic and whole-rock geochemical compositions of the three sill suites are mainly the result of interaction with evolved crustal material and by fractionation during magma transport and emplacement.

KEYWORDS: dolerite, geochemistry, geochronology, lutetium–hafnium isotopes, samarium–neodymium isotopes, Proterozoic, sills

Introduction

Mafic sills and dykes are widespread features of Proterozoic orogenic belts (Hanski et al., 2006; Srivastava, 2011; Peng and Ernst, 2016). Mafic magmas are commonly emplaced over short time intervals (Tarney, 1992), making mafic rocks an important record for constraining geological processes and the changing compositions of magmatic source materials; particularly, the subcontinental lithosphere and upper mantle (Zhao et al., 1994; Ernst and Buchan, 2001; Pirajno and Hoatson, 2012; Peng and Ernst, 2016). Mafic rocks also provide important clues to the drivers of orogenesis; the role of deep-mantle plumes; and the nature of plate tectonic processes. They may also serve as key tools in supercontinent reconstructions (Glikson et al., 1996; Morris and Pirajno, 2005; Li et al., 2006; Wang et al., 2014; Pirajno and Santosh, 2015; Howard et al., 2015). The Capricorn Orogen of Western Australia (Figs 1, 2) is a 500 km-wide zone of variably deformed rocks located between the Archean Pilbara and Yilgarn Cratons (Cawood and Tyler, 2004; Johnson et al., 2013). The orogen includes Proterozoic medium- to high-grade meta-igneous and metasedimentary rocks of the Gascoyne Province and various low-grade, variably deformed metasedimentary rocks (mainly the Edmund and Collier Groups) that unconformably overlie both the Gascoyne Province and the deformed margins of the Archean cratons (Johnson et al., 2011a, 2013).

The orogen is intruded by numerous mafic dykes and sills. Based on geochronology, paleomagnetism, petrography and geochemistry (Wingate, 2002, 2003; Wingate et al., 2004; Morris and Pirajno, 2005), mafic sills within the Edmund and Collier Groups were previously divided into the c. 1465 Ma Narimbunna Dolerite and the c. 1070 Ma Kulkatharra Dolerite (Martin et al., 2005, 2007; Thorne and Martin, 2007). Recent geochronology, field mapping, geochemistry and isotope analysis by the Geoscience and Resource Strategy Division (GRSD) in the western Capricorn Orogen have identified a third suite of sills: the c. 1514 Ma Waldburg Dolerite.

This Record summarizes and examines the petrographic, geochronological, geochemical and isotopic characteristics of all three suites of dolerite sills. It also examines the effects of fractionation and crustal contamination on the whole-rock geochemical and isotopic variations present within each of the three suites and interprets the sills' mantle sources, depths of melting and tectonic settings.

Geological setting

The Capricorn Orogen (Figs 1, 2) is the product of at least seven major orogenic events and therefore provides a record of nearly two billion years of orogenic activity, including continental collision and subsequent intraplate reactivation (Sheppard, 2004; Cawood and Tyler, 2004;

1 Centre for Exploration Targeting (CET), Curtin Node, School of Earth and Planetary Sciences, Curtin University, Bentley WA 6845

2 John de Laeter Centre, Faculty of Science and Engineering, Curtin University, Bentley WA 6845

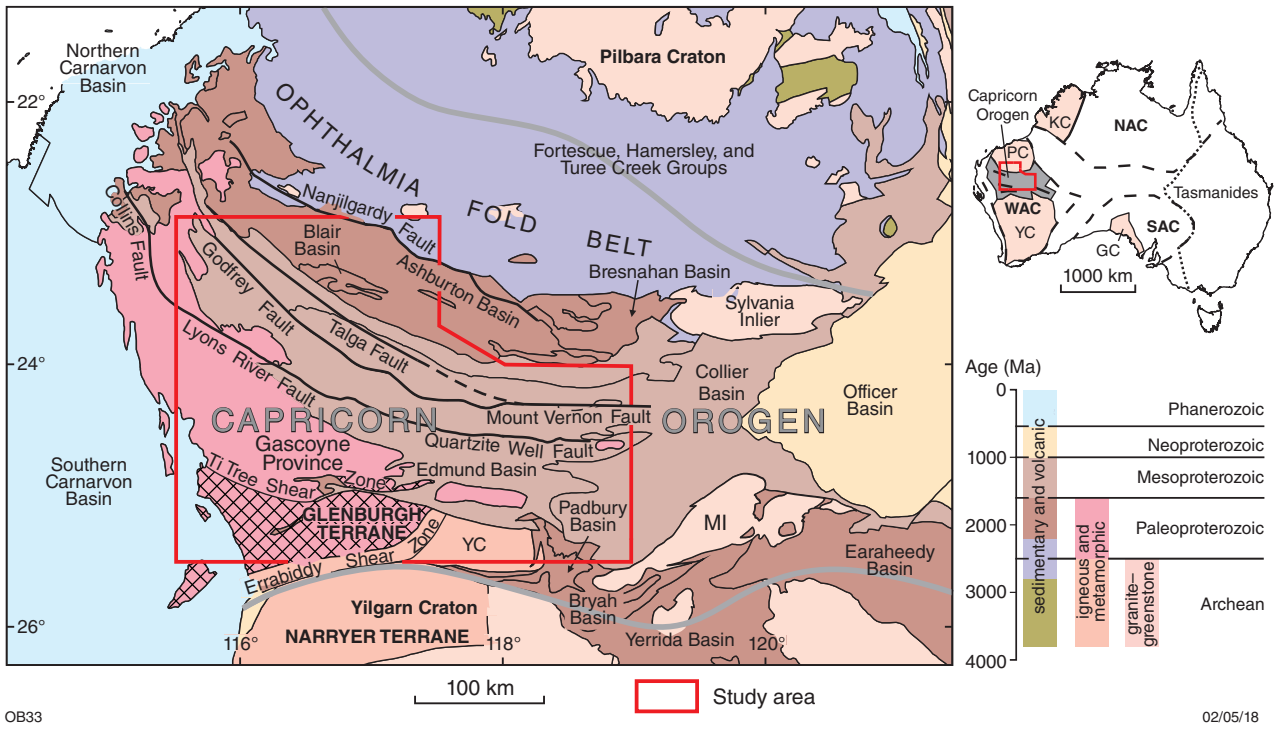

Figure 1. **Map showing the principal elements of the Capricorn Orogen, its surrounding cratons and basins, and the location of the study area (modified after Johnson et al., 2011a). Abbreviations: MI, Marymia Inlier; YC, Yilgarn Craton**

Sheppard et al., 2005, 2007, 2010; Johnson et al., 2011a; Korhonen et al., 2015, 2017). The 2215–2145 Ma Ophthalmia and 2005–1950 Ma Glenburgh Orogenies (Rasmussen et al., 2005; Johnson et al., 2010, 2011b) record the punctuated assembly of the Pilbara and Yilgarn Cratons with the Glenburgh Terrane to form the West Australian Craton. Following craton assembly, the orogen was multiply reworked during several intraplate events, including the 1820–1770 Ma Capricorn Orogeny, the 1680–1620 Ma Mangaroon Orogeny, the 1321–1171 Ma Mutherbukin Tectonic Event, the 1030–955 Ma Edmundian Orogeny and the c. 570 Ma Mulka Tectonic Event (Sheppard, 2004; Cawood and Tyler, 2004; Sheppard et al., 2005, 2007, 2010; Johnson et al., 2011a,c; Korhonen et al., 2015, 2017). The oldest two reworking events were accompanied by voluminous granite magmatism with little to no evidence for mafic magmatism (Johnson et al., 2017). However, following the Mangaroon Orogeny, the character of the orogen changed to more rigid behaviour (Johnson et al., 2017) allowing for the formation and stabilization of the deep intracontinental Edmund and Collier Basins (Martin and Thorne, 2004; Martin et al., 2008; Cutten et al., 2016) and the emplacement of abundant mafic dykes and sills into the shallow crust (Wingate, 2002, 2003; Wingate et al., 2004; Morris and Pirajno, 2005); apparently, with minimal associated felsic magmatism (GSWA 143440, Wingate et al., 2012a).

The two older suites of sills, the Waldburg and Narimbunna Dolerites, were emplaced only within the 1679–1455 Ma Edmund Basin, whereas the younger Kulkatharra Dolerite was emplaced within both the Edmund and the 1171–1067 Ma Collier Basins (Figs 1, 2). Field relationships and geochronological data suggest that all sills were emplaced shortly after or during sedimentation (Cutten et al., 2016), implying links between extensional tectonics, basin formation and mafic magmatism.

Although the Waldburg and Narimbunna Dolerites appear to be restricted to the Capricorn Orogen, the Kulkatharra Dolerite is a component of the c. 1075 Ma Warakurna Large Igneous Province (WLIP; Wingate et al., 2004), which extends well beyond the orogen, across the Pilbara Craton, the northern Yilgarn Craton and much of central Australia, and has an areal extent of $>2 \times 10^6$ km^2 (Wingate, 2017). The WLIP consists mainly of mafic igneous rocks, including abundant and widespread dolerite sills, dyke swarms and layered mafic–ultramafic intrusions, together with locally voluminous bimodal volcanic rocks, granitic sills, and plutons in the Musgrave Province (Wingate et al., 2004; Howard et al., 2011, 2016). The c. 1070 Ma dolerite sills and dykes in the Glenayle area of the eastern Capricorn Orogen (Wingate, 2003; Morris and Pirajno, 2005), which are also part of the WLIP, are located about 200 km east of the present project area and are not included in this Record. The WLIP has been interpreted to be the result of a mantle plume (Glikson et al., 1996; Wingate et al., 2004; Morris and Pirajno, 2005). However, recent work reveals that the short-duration (1080–1070 Ma) WLIP represents a major magmatic pulse during the 1084–1040 Ma Giles magmatic event in the Musgrave Province and suggests that this mantle-derived magmatism may instead reflect a long-lasting, extreme thermal anomaly at the junction between the West, North, and South Australian Cratons (Maier et al., 2014; Smithies et al., 2015; Howard et al., 2015).

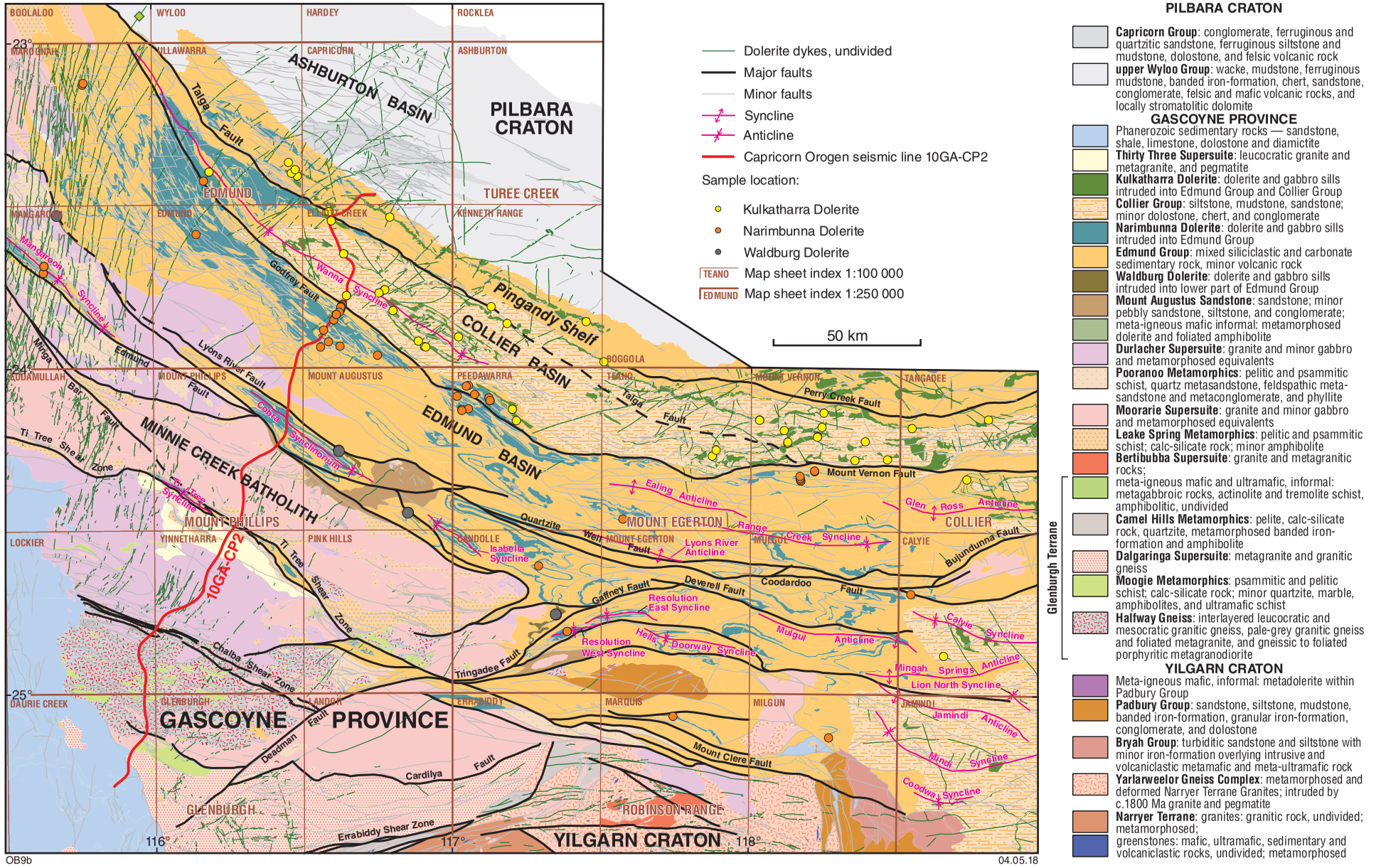

Figure 2. Geology and major structural elements of the western Capricorn Orogen (modified after Cutten et al., 2016) showing dolerite sill sample locations. A complete list of samples, coordinates and host rocks codes is provided in Appendix 1

Analytical methods

Petrography

Thirty-six outcrop and four drillcore samples were collected during fieldwork between 2010 and 2014. Polished thin sections of each sample, together with 32 additional samples from the GSWA collection, were examined using optical microscopy.

Geochronology

Several crystallization ages have been determined for each suite of mafic sills in the Capricorn Orogen (Fig. 3; Table 1). All results are U–Pb ages on zircon or baddeleyite, or both, and all are published by GSWA, most as part of the Geochronology Record Series (references are provided in Table 1). Geochronology was conducted using the Sensitive High-Resolution Ion Microprobe (SHRIMP) instruments at the John de Laeter Centre at Curtin University. Details of each sample, including analytical parameters, are included in each cited Geochronology Record and procedures are similar to those described by Wingate and Lu (2017). The sections below summarize and interpret the geochronology data for each suite of dolerite sills. All dates discussed in this Record are based on $^{207}Pb^*/^{206}Pb^*$ ratios (Pb*, radiogenic Pb) and quoted with 95% confidence intervals ($t\sigma\sqrt{MSWD}$) unless noted otherwise (MSWD, mean square of weighted deviates).

Geochemistry

A total of 102 samples of fine- to medium-grained dolerite was analysed for whole-rock geochemistry and trace and rare earth elements (REE). All results have been published (GeoChem Extract: GSWA, 2017) and some have been interpreted previously (Morris and Pirajno, 2005). Weathered surfaces and veins were removed and the samples were washed, dried, crushed and milled to a very fine powder (90% passing <75 microns). A 50 gram split was used for geochemical analysis by standard X-ray fluorescence (XRF) spectroscopy and inductively coupled plasma mass spectrometry (ICP-MS) techniques (Morris, 2000; Morris and Pirajno, 2005). Results for major oxides, trace elements, LOI and calculated values are tabulated in Appendix 1.

Isotope analyses

Thirty-three whole-rock samples were analysed for their Sm–Nd isotope compositions (Appendix 4). Measurements were conducted on a separate split from each of the rock powder samples used for whole-rock geochemistry analyses and were determined by isotope dilution thermal ionization mass spectrometry (IDTIMS) or by laser ablation multi-collector inductively coupled plasma mass spectrometry (LA-MC-ICPMS) techniques (e.g. Stern, 2001; Kirkland et al., 2011). Thirteen of these results were previously published in Morris and Pirajno (2005). Although fractionation of Sm and Nd in mafic rocks is assumed to have occurred mainly during melt extraction from the mantle, isotope ratios can be modified by processes such as partial melting, fractional crystallization, magma mixing, assimilation and alteration (Champion, 2013). We have calculated two-stage depleted-mantle model ages (T_{DM}^2), which yield more consistent results and allow model ages to be calculated for samples with high measured $^{147}Sm/^{144}Nd$ ratios (c. 0.15) as shown in Appendix 4 (Champion and Cassidy, 2008; Champion, 2013). Model ages use the depleted-mantle model of Goldstein et al. (1984), where $^{147}Sm/^{144}Nd = 0.2136$, $^{143}Nd/^{144}Nd = 0.513163$ and with an average crustal $^{147}Sm/^{144}Nd$ ratio of 0.11. Present-day CHUR values of $^{143}Nd/^{144}Nd = 0.512650$ and $^{147}Sm/^{144}Nd = 0.1967$ are from Wyborn et al. (1988) and Mole et al. (2013).

A total of 101 Lu–Hf isotope measurements (Appendix 5) was conducted on 73 dated zircon and 28 baddeleyite crystals from six samples using a New Wave/Merchantek LUV213 laser ablation microprobe attached to a Nu Plasma MC-ICPMS at Macquarie University, Sydney. Calculation of initial $^{176}Hf/^{177}Hf$ is based on the ^{176}Lu decay constant (1.867×10^{-11} yr^{-1}) of Scherer et al. (2001). Because $^{176}Hf/^{177}Hf$ departures from the CHUR evolution line are very small, epsilon (ε) notation is used (one ε unit represents a one part per 10 000 deviation from the CHUR composition). Calculations of ε_{Hf} values employ the ^{176}Lu decay constant of Scherer et al. (2001) and the CHUR values of Blichert-Toft and Albarède (1997). Detailed methods are described in Payne et al. (2016) and Haines et al. (2016). Single-stage (T_{DM}) model ages are calculated from measured $^{176}Hf/^{177}Hf$ ratios, assuming that the magma in which zircon and baddeleyite crystallized was derived from a depleted-mantle source (Griffin et al., 2000, 2004).

Waldburg Dolerite

The Waldburg Dolerite (Blay et al., 2016) comprises four, mainly northwest-striking dolerite sills on Mangaroon, Mount Augustus, Mount Phillips, and Candolle (map sheet names refer to 1:100 000 Geological Series map sheets unless indicated otherwise). The sills intrude the middle and lower strata of the Edmund Group — Depositional Packages 1 to 3 (Thorne, 2015a–c). They have limited exposure but appear to be laterally continuous (up to 36 km long) and range in thickness from 100 to 500 m. The sills were emplaced in a structural corridor between two major fault structures, the Lyons River Fault and the Ti Tree Shear Zone (Fig. 2) at, or near, fault contacts between different lithologies, within silicified siltstone units and sedimentary successions dominated by carbonate rocks. The dolerite generally outcrops as brownish-black rounded boulders, with thick colluvial scree at the top of low hills and ridges, within small creeks, or at the bases of low slopes. The Waldburg Dolerite is typically altered, strongly fractured, and exhibits spheroidal weathering.

Petrography

The Waldburg Dolerite is highly altered and typically has a greenish colour on fresh surfaces. On Mangaroon, Candolle, and Mount Augustus, the sills consist mainly of medium- to coarse-grained dolerite containing patches of very coarse-grained dolerite to leucogabbro that contain rare anorthosite veins. These dolerites also contain fine- to medium-grained felsic veins of predominantly granophyric quartz–plagioclase, up to 3–4 cm thick (Fig. 4a,b). In most cases, these veins are interpreted as late-magmatic

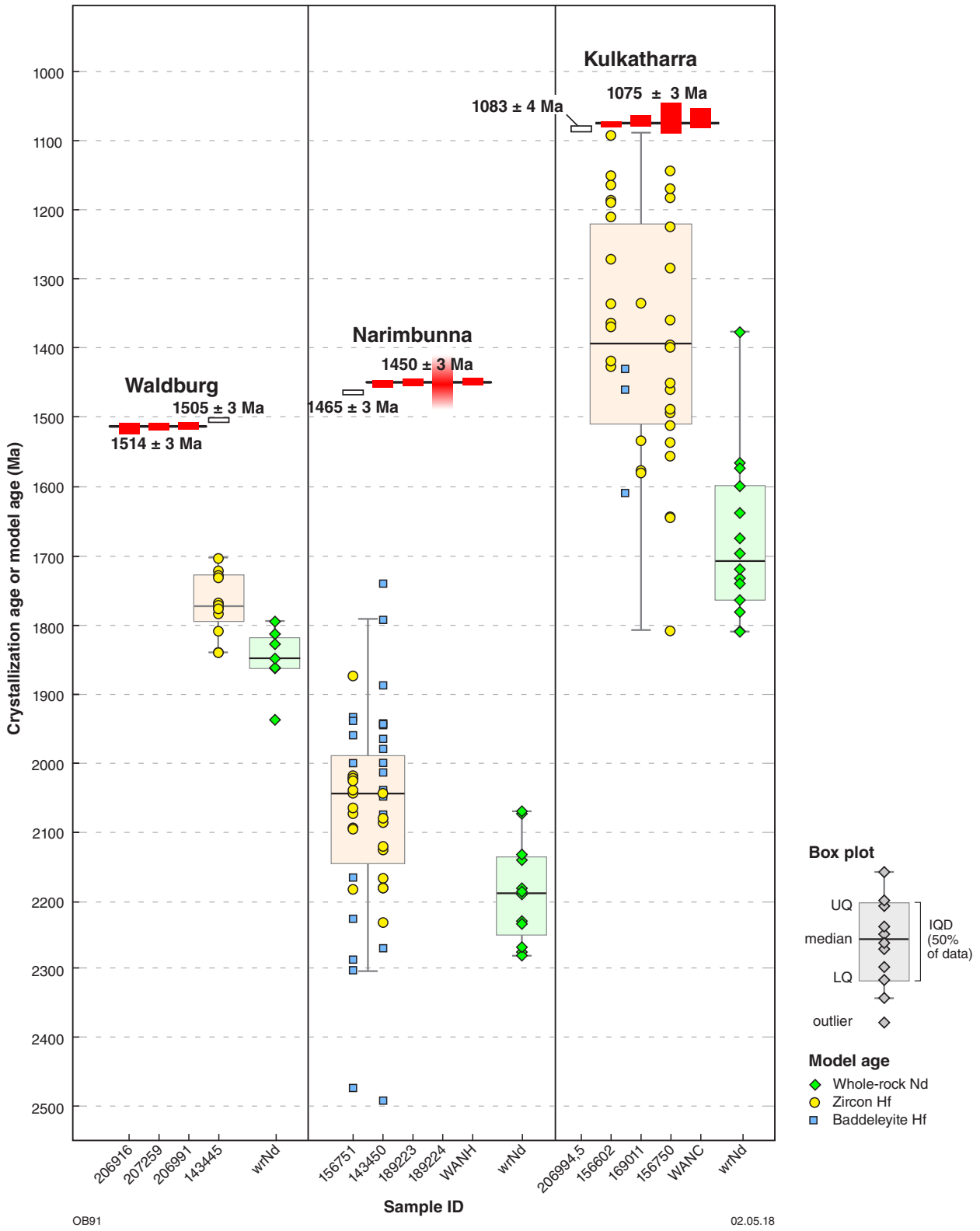

Figure 3. **Summary of crystallization ages and model ages for dolerite sills. U–Pb crystallization ages are quoted with 95% uncertainties (details are in Table 1). Depleted-mantle model ages for baddeleyite and zircon Lu–Hf zircon (T_{DM}) and whole-rock Sm–Nd (T_{DM}^{2}) samples (Appendices 4 and 5) are plotted individually and summarized in box plots. The box between the upper and lower quartiles (UQ, LQ) contains 50% of the data; outliers are >(UQ + 1.5 × IQD) or <(LQ – 1.5 × IQD) from the median value. Abbreviation: IQD, interquartile distance**

Table 1. Geochronology of the Waldburg, Narimbunna and Kulkatharra Dolerites

Sample ID	*Crystallization age (Ma)*	*Minerals dated*	*Rock type*	*100k map sheet*	*Latitude (°)*	*Longitude (°)*	*Reference*
Kulkatharra Dolerite							
WANC	1067 ± 14	z,b	dolerite	Elliot Creek	-23.80583	116.63306	Wingate, 2002
156750	1068 ± 22	b	dolerite	Ullawarra	-23.39844	116.18967	Nelson, 2001a; Wingate, 2002
169011	1071 ± 8	z,b	dolerite	Elliot Creek	-23.51958	116.58677	Nelson, 2001c; Wingate, 2002
156602	1076 ± 4	z	dolerite	Kenneth Range	-23.81968	117.13454	Wingate and Bodorkos, 2007
206994,5	1083 ± 4	z	altered dolerite	Peedawarra	-24.16340	117.21361	Wingate et al., 2015c,d
Narimbunna Dolerite							
WANH	1449 ± 5	z	leucogabbro	Elliot Creek	-23.81389	116.62917	Wingate, 2002
189224	c. 1450	b	dolerite	Marquis	-25.07039	117.74374	Wingate et al., 2014
189223	1450 ± 5	z	dolerite	Milgun	-25.13315	118.26857	Wingate et al., 2013b
143450	1452 ± 5	z,b	dolerite	Candolle	-24.81112	117.38602	Wingate et al., 2012c
156751	1465 ± 3	z,b	dolerite	Mangaroon	-23.68472	115.63778	Nelson, 2001b; Wingate, 2002
Waldburg Dolerite							
143445	1505 ± 3	z	dolerite	Candolle	-24.75967	117.34894	Wingate et al., 2012b
206991	1513 ± 5	z	felsic vein	Mount Augustus	-24.25715	116.62012	Wingate et al., 2015b
207259	1514 ± 5	z,b	leucogabbro	Mangaroon	-23.53186	115.68296	Wingate et al., 2013a, 2017
206916	1517 ± 8	z	felsic vein	Mount Augustus	-24.44712	116.85024	Wingate et al., 2015a

NOTES: U–Pb crystallization ages are quoted with 95% confidence intervals. Abbreviations: z, zircon; b, baddeleyite

fractionates that filled cooling fractures in the dolerite host (e.g. GSWA 206916, Wingate et al., 2015a). These veins were targeted for zircon or baddeleyite geochronology.

Waldburg Dolerite samples typically display well-preserved ophitic to allotriomorphic-granular textures. Clinopyroxene and plagioclase are the major mineral phases, with lesser orthopyroxene and intergranular granophyric and myrmekite segregations, or both, that are typically enriched in fine-grained acicular apatite and zircon. Interstitial anhedral quartz forms a trace constituent.

Iron–titanium oxide minerals typically form skeletal crystals and are extensively replaced by titanite. Granophyre is commonly nucleated around euhedral prisms of plagioclase. Clinopyroxene is commonly twinned. The modal proportions of primary mineral phases vary only a few percent between outcrops. On Mangaroon, plagioclase (mainly andesine to labradorite) is the dominant mineral phase (40–45%) together with 20–25% quartz–microcline granophyre and 10–12% clinopyroxene (diopside). On Mount Augustus, dolerite contains about 40% plagioclase (oligoclase–andesine, An_{28}–An_{34}) which is recrystallized but retains subhedral to euhedral form and, in some grains, relict albite twinning. The dolerite on Mount Augustus is crosscut by rare anorthositic veins consisting of about 70% fine-grained euhedral albite prisms which are heavily clouded by microcrystalline clinozoisite and actinolite. On Candolle, the dolerite is dominated by two pyroxenes; whereas on Mount Augustus, the sills contain roughly equal proportions of plagioclase and pyroxene.

Most primary minerals in the Waldburg Dolerite are partially to extremely altered. Up to 40% of plagioclase is extensively replaced by epidote or polyphase pseudomorphs composed of saussurite–clinozoisite group minerals, and saussurite–sericite–albite (Fig. 5). Pale green clinopyroxene is partially replaced by secondary amphibole, chlorite and saussurite, or by acicular-to-bladed actinolite–tremolite pseudomorphs up to 10 mm long and which are commonly oriented parallel to the main axis of the original minerals. Coarse-grained orthopyroxene phenocrysts are typically pseudomorphed by microcrystalline aggregates of tremolite, actinolite and chlorite. Brown hornblende, pleonaste and small flakes of secondary biotite (replacing amphibole) are commonly interstitial to plagioclase and pyroxene. On Mount Augustus, interstitial minerals are locally dominated by about 10% microcrystalline chlorite. Locally, on Candolle, thin veinlets of microcrystalline tremolite and chlorite intergrowths crosscut massive dolerite.

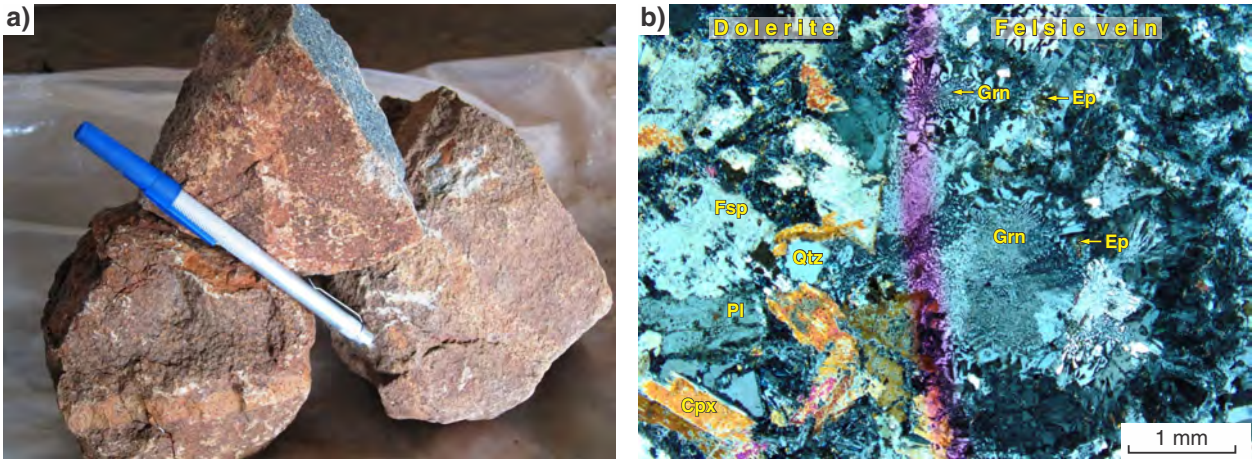

Figure 4. **Felsic veins in Waldburg Dolerite samples: a) vein in geochronology sample GSWA 206916, 1.0 – 1.5 cm wide, crosscutting medium-grained Waldburg Dolerite; b) photomicrograph (cross-polarized light) of a fine-grained quartz–feldspar vein from the same sample showing patchy granophyre intergrowths and minor epidote alteration. Abbreviations: Grn, granophyre; Ep, epidote; Fsp, feldspar; Pl, plagioclase; Cpx, clinopyroxene; Qtz, quartz. The pink line outlines the margin between dolerite (left) and the felsic vein**

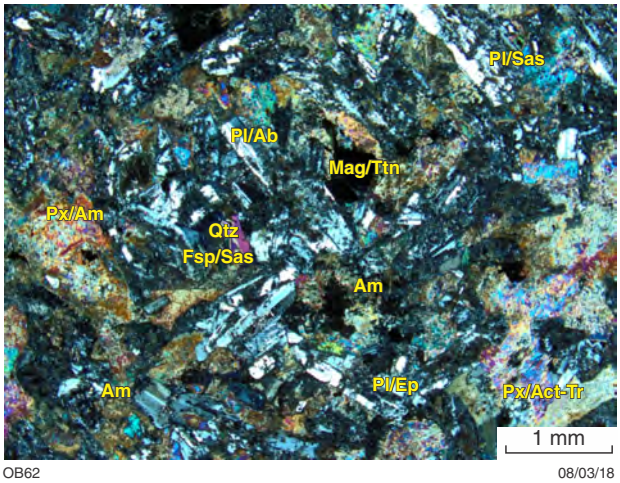

Figure 5. **Photomicrograph (cross-polarized light) of Waldburg Dolerite sample GSWA 207259 (MGA 365554E 7396984N) showing replacement of primary pyroxene (Px) by amphibole (Am) or actinolite–tremolite(Act–Tr). Plagioclase is extensively replaced by epidote (Ep) or pseudomorphed by saussurite (Sas) or albite (Ab); magnetite (Mag) is partly replaced by titanite (Ttn). Abbreviations: Qtz, quartz; Fsp, feldspar**

Geochronology

Four samples of Waldburg Dolerite sills yielded U–Pb zircon and/or baddeleyite crystallization ages of 1517–1505 Ma (Fig. 3; Table 1). Two sills, sampled about 31 km apart near Mount Augustus, intruded Depositional Package 3 (Kiangi Creek Formation). These are dated at 1517 ± 8 and 1513 ± 5 Ma (GSWA 206916, Wingate et al., 2015a; GSWA 206991, Wingate et al., 2015b) using zircons recovered from thin, granophyric quartz–plagioclase veins interpreted as late-magmatic fractionates. A similar crystallization age of 1514 ± 5 Ma was obtained from 43 combined analyses of zircon and baddeleyite extracted from very coarse-grained leucogabbro within mainly medium-grained dolerite (GSWA 207259, Wingate et al., 2013a; 2017) in a sill intruded at the base of Depositional Package 1 (Yilgatherra Formation), about 140 km to the northwest, on Mangaroon. Medium- to coarse-grained dolerite of the fourth sill (GSWA 143445, Wingate et al., 2012b), which also intruded Depositional Package 1 (Irregully Formation), was sampled about 68 km southeast of Mount Augustus, on Candolle, and yielded zircons that indicated a crystallization age of 1505 ± 3 Ma.

The ages for the three older sills (Fig. 3; Table 1) agree closely and yield a weighted mean of 1514 ± 3 Ma (MSWD = 0.43). At 1505 ± 3 Ma, the sill on Candolle is significantly younger and, presumably, represents a separate episode of dolerite intrusion; although, it could represent the younger end of a prolonged intrusive event between 1514 and 1505 Ma. However, the geochemistry, isotope characteristics, petrography and geological settings do not indicate significant differences between the sills of different ages.

Geochemistry

The Waldburg Dolerite has a distinctive geochemical composition in terms of its major, trace and REE concentrations which are significantly different from those of other mafic igneous rocks within the western Capricorn Orogen (Table 2; Appendices 1, 3).

Alteration

Rocks can be affected by postmagmatic processes which may potentially induce mobility of major and trace elements. Several geochemical studies of altered igneous rocks have suggested that the large-ion lithophile elements (LILE), such as K, Na, Rb, Cs, Sr and Ba, are generally more mobile than the high field strength elements (HFSE), such as Zr, Nb, Hf, Ta, Ti, U and Th or REE during low-grade metamorphism (Cann, 1970; Pearce, 1975, 1996; Rollinson, 1993; Blundy and Wood, 2003); therefore, geochemical comparisons based on LILE have been avoided here. Loss on ignition (LOI) is a useful indicator of the degree of alteration (Winchester and Floyd, 1976; Hynes, 1980; Gelinas et al., 1982; Ludden et al., 1982; Morris and Pirajno, 2005).

Samples of Waldburg Dolerite have moderate-to-high (average of 1.86%) LOI values (Appendix 1), suggesting intense alteration and possible geochemical modification. However, both Ti and Zr are typically considered to be relatively immobile during alteration and can therefore be used as markers to evaluate the mobility of other elements. For the Waldburg Dolerite, Ti and Zr are positively correlated, whereas there is no correlation between Ti/Zr and LOI. This, coupled with the relatively consistent values of Ti/Zr, regardless of volatile content (Fig. 6), indicates that both Ti and Zr were not significantly affected by postmagmatic processes. Similarly, Zr shows a positive correlation with HFSE and REE elements (Fig. 6), suggesting that the HFSE and REE have also not been significantly modified. This is in contrast to the LILE, which exhibit a significantly wider variation between Na_2O, K_2O, Rb, Sr, Cs, Ba, and LOI. Together with a lack of correlation between LILE and Zr (Fig. 6; Appendix 2), this suggests LILE mobility during alteration.

Major, trace and rare earth element composition

The Waldburg Dolerite is tholeiitic in composition (Fig. 7) and equivalent to high-Fe tholeiitic basalt and sub-alkaline basalt (Figs 8, 9). The dolerites typically have relatively low average concentrations (Table 2) of SiO_2 (48.85%), K_2O (0.39%), P_2O_5 (0.13%); moderate concentrations of Na_2O (2.16%); relatively high CaO (10.89%) and MgO (7.06%); and a moderate Mg# of 51.

The Waldburg Dolerite has notably low concentrations of most REE and HFSE (Table 2); for example, La (4.87 – 8.30 ppm, average = 7.21 ppm); Yb (1.51 – 2.51 ppm, average = 2.05 ppm); and Nb (3.7 – 6.4 ppm, average = 5.3 ppm). The dolerite shows slightly negatively sloping HFSE–REE profiles in primitive mantle-normalized spider diagrams of immobile elements (Fig. 10) that are marked by slight negative Nb anomalies. The degree of REE fractionation is very weak in terms of both light REE $(La/Sm)_N$ = (1.30 – 1.54) and heavy REE $(Gd/Yb)_N$ = (1.42 – 1.94) displaying only very minor light REE versus heavy REE enrichment (Appendix 1). The low REE abundances and flat profiles, together with high MgO concentrations (Table 2), may reflect a higher degree of melting of a relatively refractory mantle source (Howard et al., 2007). As shown in Appendix 1 the dolerites have low trace element ratios of Th/La (0.10 – 0.13, average = 0.11), La/Nb (1.24 – 1.46, average = 1.36), Th/Nb (0.13 – 0.17, average = 0.15) and low-to-moderate La/Sm (1.99 – 2.39, average = 2.14) , indicating that their chemical characteristics reflect their mantle source and melting conditions and, therefore, that they have not been significantly modified by crustal contamination (Sun and McDonough, 1989; Farmer, 2005). Relatively shallow trends between Zr and La/Sm, Th/Tb (Appendix 3a) suggest crystal fractionation was the main process responsible for magmatic differentiation.

Bivariate diagrams showing major oxides, Cr and Ni, versus Mg# (Fig. 12a) display characteristic correlation patterns. The increase of $Fe_2O_3^T$ and decrease of Al_2O_3 with decreasing Mg# indicate that olivine + plagioclase were involved in magma crystallization (Fig. 12a). The AFM diagram (Fig. 7) also shows a typical tholeiitic trend, indicating that fractionation was controlled by early olivine and clinopyroxene fractionation (decreasing MgO) and that magnetite fractionated late (increasing FeO).

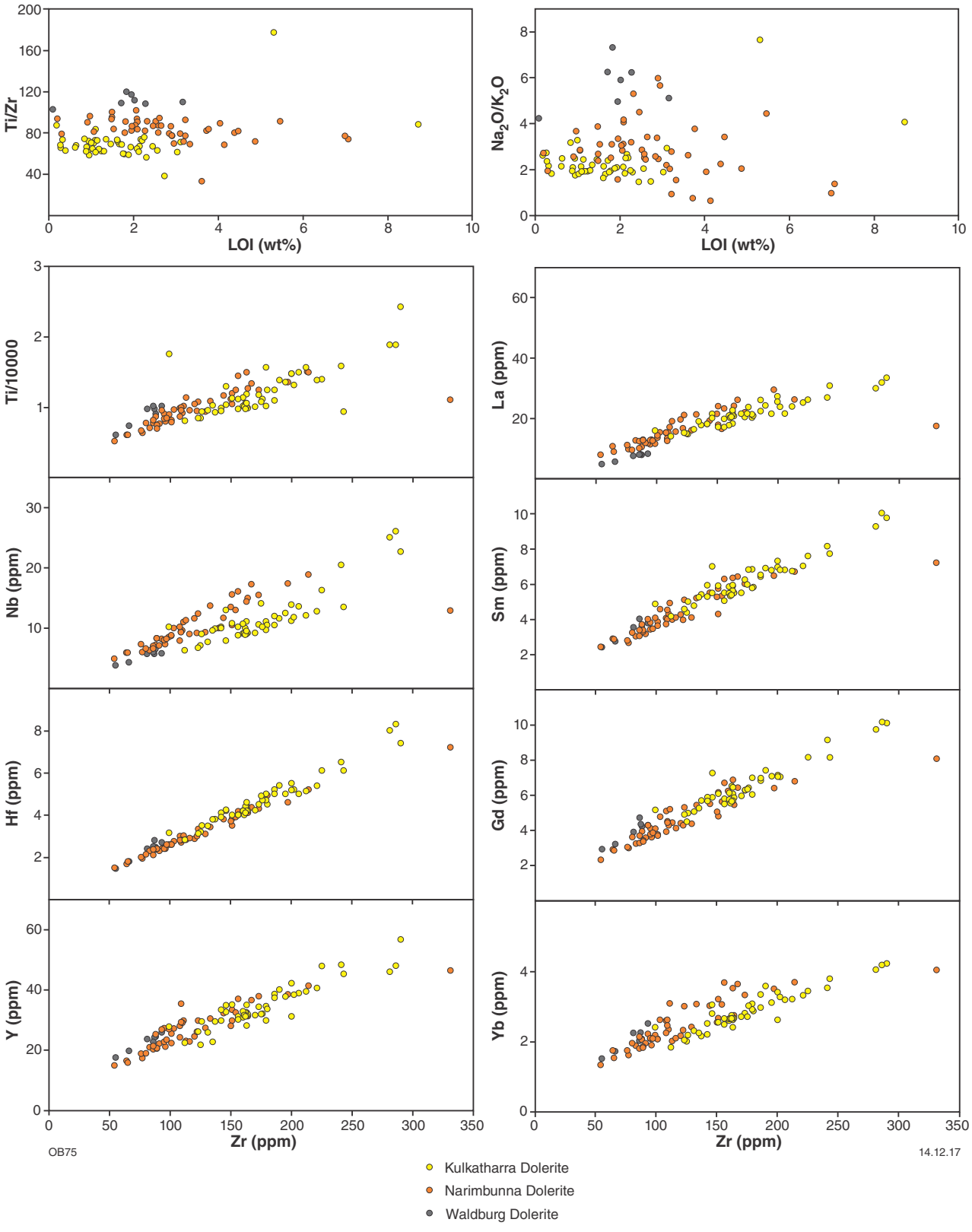

Figure 6. Bivariate diagrams assessing the influence of postmagmatic processes on mobility of major and trace elements plotted against Zr concentration and loss on ignition (LOI)

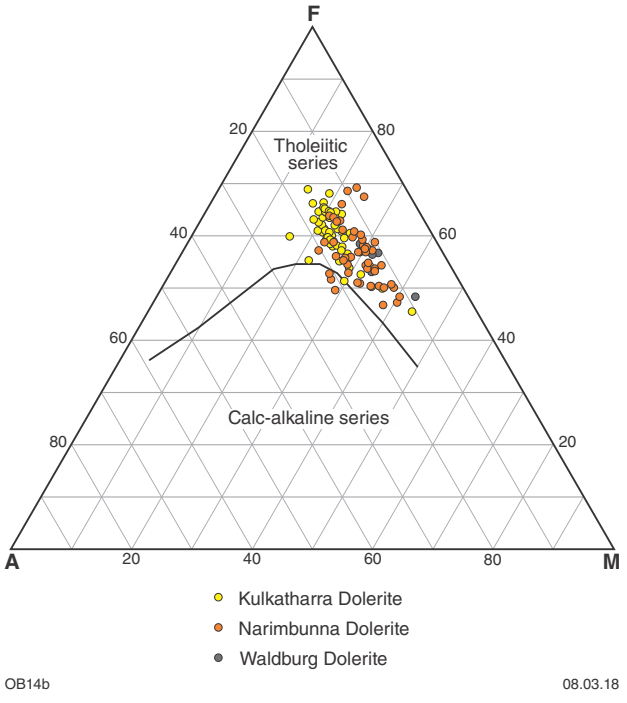

Figure 7. **Ternary AFM classification diagram (Irvine and Baragar, 1971) showing the tholeiitic character of the Capricorn Orogen dolerite sills. AFM (Alkalis–Iron–Magnesium: A, $Na_2O + K_2O$; F, $FeO + Fe_2O_3$; M, MgO)**

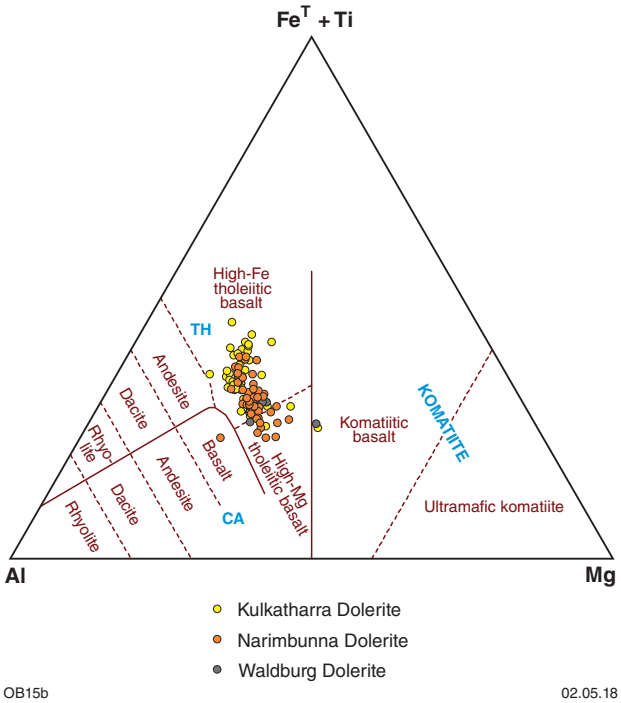

Figure 8. **Ternary cation diagram (Jensen, 1976) showing dolerite sill samples plotting mainly within the high-Fe tholeiitic basalt field and, to a lesser extent, the high-Mg tholeiitic basalt field. Abbreviations: CA, calc-alkaline basalt; TH, tholeiitic basalt; Al_2O_3 (Al); $FeO + Fe_2O_3 + TiO_2$ ($Fe^T + Ti$); MgO (Mg)**

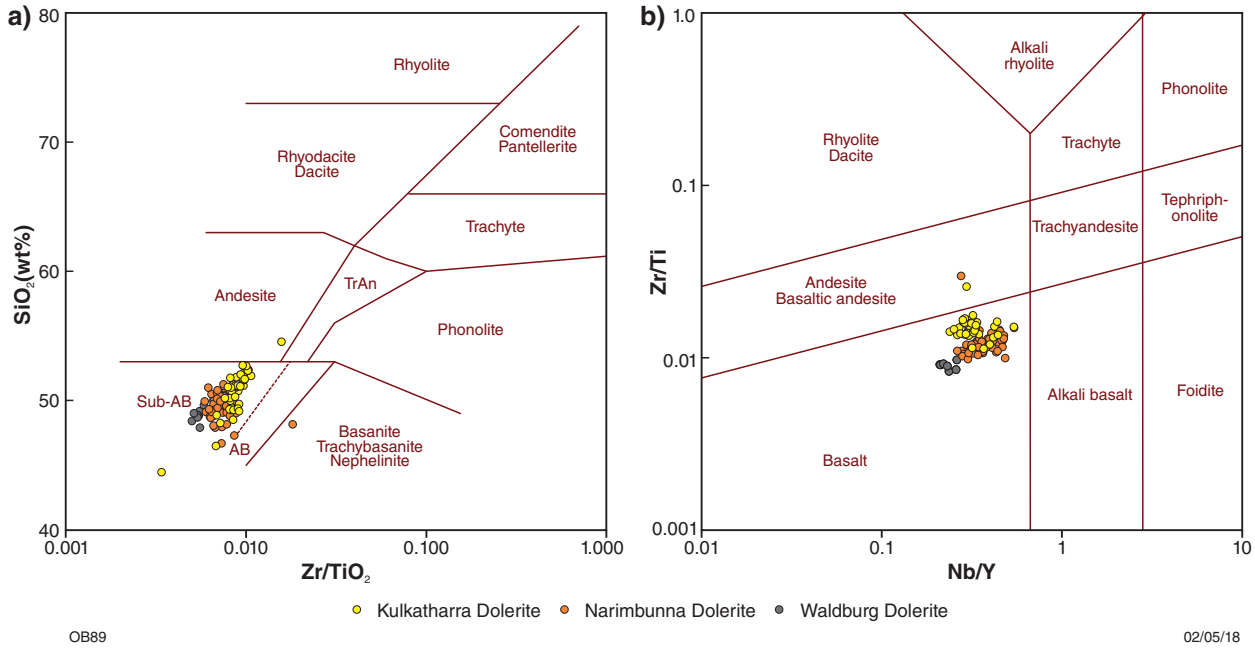

Figure 9. **Discrimination diagrams for classification of volcanic rocks using incompatible element ratios: a) Zr/TiO_2 vs SiO_2 (Winchester and Floyd, 1976) shows the position of dolerite sill samples predominantly within the sub-alkaline basalt field; b) Nb/Y vs Zr/Ti (Pearce, 1996, modified after Winchester and Floyd, 1976) displays a clear separation of samples from different dolerite sill groups. Abbreviations: Sub-AB, sub-alkaline basalt; AB, alkaline basalt; TrAn, trachyandesite**

Table 2. Ranges and average concentrations of major oxides and trace elements in dolerite samples

Elements	Waldburg Dolerite		Narimbunna Dolerite		Kulkatharra Dolerite	
	Average	Range	Average	Range	Average	Range
			Percentage (wt%)			
SiO_2	48.85	47.93 – 49.69	49.49	46.74 – 51.28	50.81	44.47 – 54.58
TiO_2	1.47	1.00 – 1.68	1.60	0.85 – 2.49	2.02	1.34 – 4.04
Al_2O_3	13.76	13.65 – 14.65	13.80	12.43 – 16.39	13.21	11.30 – 14.46
***$Fe_2O_3^T$**	13.25	11.60 – 14.20	13.28	9.96 – 16.76	14.54	10.99 – 18.33
MnO	0.20	0.18 – 0.22	0.23	0.16 – 0.48	0.19	0.16 – 0.23
MgO	7.06	6.23 – 9.85	6.17	4.46 – 8.51	5.09	3.22 – 9.74
CaO	10.89	10.18 – 11.62	9.68	4.95 – 12.34	8.95	7.15 – 11.56
Na_2O	2.16	1.75 – 2.48	2.12	1.23 – 3.65	2.43	1.63 – 3.19
K_2O	0.39	0.28 – 0.47	0.89	0.32 – 2.33	1.12	0.37 – 1.96
P_2O_5	0.13	0.08 – 0.14	0.21	0.11 – 0.62	0.23	0.14 – 0.40
			Parts per million (ppm)			
Cr	227	134–348	150	16–542	85	8–759
Ni	95	69–148	76	22–152	100	50–245
V	324	275 – 366	323	226–443	350	140–897
Pb	2.3	0.7 – 6.0	3.4	0.50 – 15.8	7.6	3.4 – 13.0
Cu	90	71–109	98	9–144	168	48–351
La	7.21	4.87 – 8.30	15.98	7.97 – 29.51	21.60	14.09 – 31.90
Ce	17.06	11.4 – 19.4	33.41	16.70 – 60.05	46.94	31.02 – 72.30
Pr	2.46	1.65 – 2.85	4.25	2.17 – 7.48	5.95	3.74 – 9.50
Nd	11.86	8.02 – 13.80	18.51	9.62 – 30.65	26.15	17.75 – 42.05
Sm	3.37	2.42 – 4.03	4.33	2.43 – 7.22	6.24	4.18 – 10.05
Eu	1.23	0.98 – 1.36	1.52	0.84 – 2.62	1.92	1.29 – 3.02
Gd	3.96	2.94 – 4.73	4.55	2.34 – 8.07	6.53	4.50 – 10.15
Tb	0.64	0.48 – 0.72	0.75	0.38 – 1.32	1.07	0.70 – 1.67
Dy	4.05	3.08 – 4.64	4.54	2.48 – 7.80	6.14	3.96 – 9.40
Ho	0.85	0.65 – 0.98	0.96	0.50 – 1.42	1.25	0.79 – 1.95
Er	2.32	1.78 – 2.60	2.68	1.57 – 4.66	3.30	2.03 – 4.74
Tm	0.38	0.36 – 0.40	0.36	0.25 – 0.52	0.51	0.29 – 0.74
Yb	2.05	1.51 – 2.51	2.45	1.33 – 4.03	2.85	1.83 – 4.21
Lu	0.32	0.23 – 0.36	0.38	0.20 – 0.60	0.43	0.27 – 0.61
Y	22.6	17.6 – 25.9	27.0	15.0 – 41.4	34.6	21.8 – 56.7
Zr	79	55–93	119	54–214	176	99–286
Nb	5.3	3.7 – 6.4	10.1	4.8 – 18.8	11.5	6.2 – 26.0
Hf	2.30	1.46 – 2.80	3.04	1.50 – 7.20	4.69	2.82 – 8.30
Th	0.78	0.60 – 0.94	1.88	0.90 – 3.90	4.88	2.68 – 8.47
U	0.16	0.12 – 0.19	0.38	0.17 – 0.72	0.69	0.34 – 1.16
Ti	8840	6019–10072	9606	5084–14904	12091	8034–18825
Ta	0.34	0.22 – 0.40	0.61	0.29 – 1.2	0.67	0.39 – 1.30
Sc	39.4	37.0 – 43.0	36.22	28.0 – 48.0	29.0	25.0 – 36.0
Ga	19.5	14.7 – 21.7	19.0	15.1 – 23.2	22.2	15.7 – 26.7

NOTE: *All Fe as Fe_2O_3

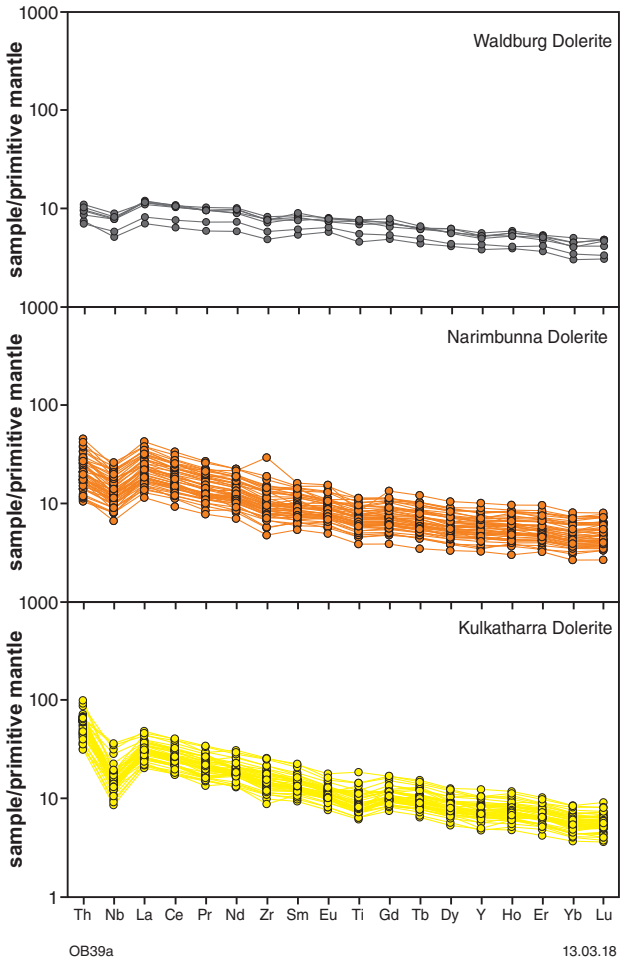

Figure 10. **(left) Primitive mantle-normalized spider diagrams of immobile elements ordered by trace element incompatibility, comparing the mafic rock chemistry of dolerite sill groups. Normalizing values are from Sun and McDonough (1989)**

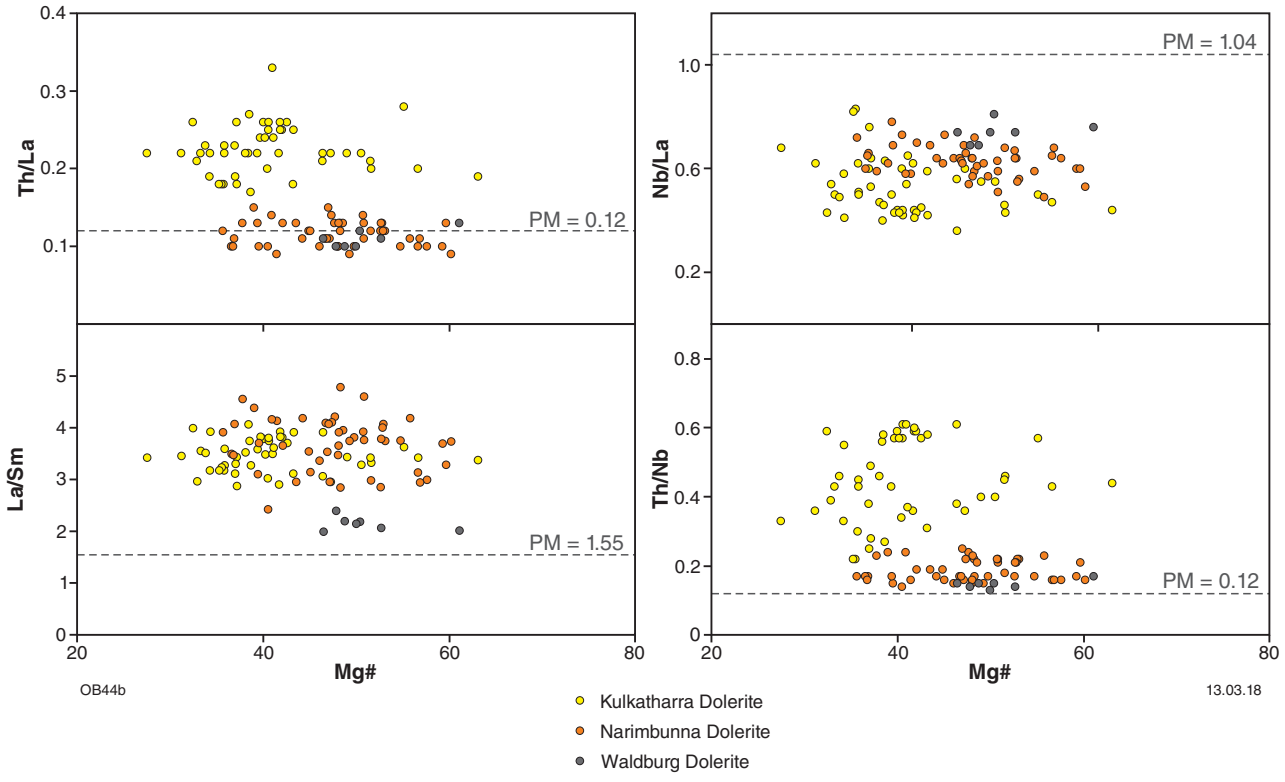

Figure 11. **Binary variation diagrams illustrating Th/La, Nb/La, La/Sm, and Th/Nb vs Mg#, and showing distinct geochemical characteristics of the dolerite sill groups in terms of REE–HFSE ratios relative to primitive mantle (PM). Mg#, molecular ratio of Mg/(Mg + total Fe)**

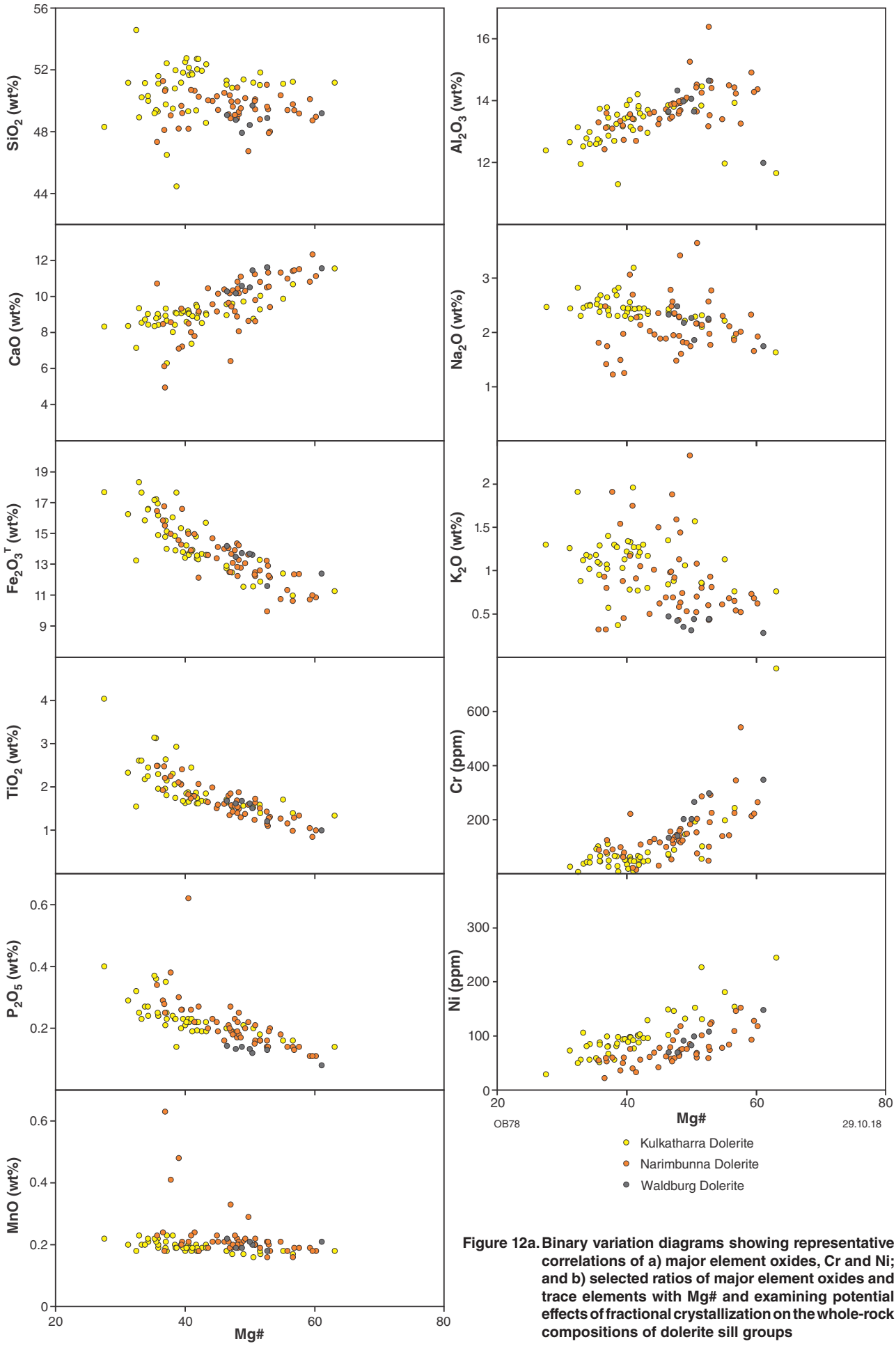

Figure 12a. Binary variation diagrams showing representative correlations of a) major element oxides, Cr and Ni; and b) selected ratios of major element oxides and trace elements with Mg# and examining potential effects of fractional crystallization on the whole-rock compositions of dolerite sill groups

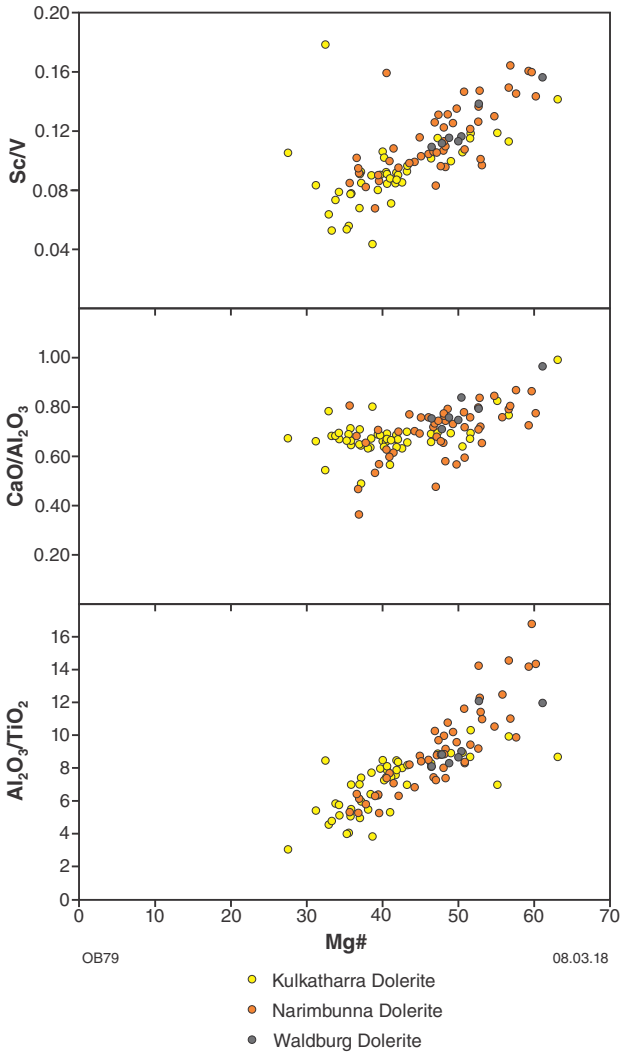

Figure 12b.

The variation in Cr/Ti, Cr/Zr, and V/Zr ratios (Appendix 1) can be explained, in particular, by the fractionation of pyroxene (Pearce and Cann, 1973; Nesbitt et al., 1984; Wilson, 1989). The correlation patterns generally show that fractionation was initially controlled by olivine, then by pyroxene and plagioclase. The trends are in agreement with petrographic observations and suggest that fractionation was a major control on geochemical composition of the Waldburg Dolerite.

Isotope analyses

The Waldburg Dolerite has relatively high $^{143}Nd/^{144}Nd_{(i)}$ ratios (Appendix 4), ranging from 0.510701 to 0.510788, with a narrow range of $\varepsilon_{Nd(i)}$ values from 0.16 to 2.08 (Appendix 4; Fig. 14). Two-stage depleted-mantle model ages (T_{DM}^{2}) range from 1.94 to 1.80 Ga, with a median of 1.85 Ga (Fig. 3). Lu–Hf analyses of 12 zircons from sample GSWA 143445 yielded a narrow range of radiogenic initial $^{176}Hf/^{177}Hf_{(i)}$ ratios between 0.281915 and 0.282019 (Appendix 5), corresponding to $\varepsilon_{Hf(i)}$ values between 3.2 and 6.7, with a mean of 5.0 (Fig.15a), and model ages (T_{DM}) between 1.84 and 1.71 Ga, with a median of 1.78 Ga (Figs 3, 15b).

The results from both isotopic systems suggest that the Waldburg Dolerite was derived from a radiogenic source with a composition between depleted mantle and CHUR and which interacted with only minor amounts of evolved crustal material, either in the source or emplacement regions. A low degree of crustal contamination is also indicated by the weak correlation between $\varepsilon_{Nd(i)}$ and SiO_2, $(La/Sm)_{CN}$, Mg#, and Nb/La, as well as positive $\varepsilon_{Nd(i)}$ values (Fig. 13; Appendix 5). Older model ages for whole-rock Sm–Nd compared to zircon Lu–Hf may indicate that the whole-rock samples reflect contribution from refractory crustal phases that did not contribute to the melt source of the zircon.

Summary

The Waldburg Dolerite consists of medium-grained to very coarse-grained, highly altered mafic rocks that are locally intruded by a network of thin, probably late-magmatic quartz–feldspar veins. Plagioclase and pyroxene are the main primary mineral phases and are partially replaced by low- to medium-grade metamorphic minerals; typically, epidote, actinolite, tremolite, amphibole, chlorite, clinozoisite group minerals, and saussurite. Crystallization ages for four dated sills range from 1517 to 1505 Ma, with three samples yielding a mean age of 1514 ± 3 Ma. The fourth sample, dated at 1505 ± 3 Ma, presumably represents a separate episode of dolerite intrusion. However, geochemistry, isotope characteristics, petrography and geological settings do not show much difference between the sills. The Waldburg Dolerite has relatively high MgO–Cr contents and notably low concentrations in most REE and HFSE. The mafic rocks show weak REE fractionation in both light REE and heavy REE with very slight light-REE enrichment, weak negative Nb anomalies and a relatively low average La/Nb ratio of 1.36. This chemistry suggests only minor crustal input and probably reflects the mantle source and melting conditions. Low variation in Th and Yb contents and Nd and Hf isotope compositions, together with positive $\varepsilon_{Nd(i)}$ and $\varepsilon_{Hf(i)}$ values (Appendices 1,4,5), indicate that the Waldburg Dolerite was derived from a radiogenic source which interacted with minor amounts of evolved crustal material in either the source or emplacement region.

Narimbunna Dolerite

The Narimbunna Dolerite (Blay et al., 2015a) is present throughout the western Capricorn Orogen where it intrudes low-grade metasedimentary rocks of the Edmund Group — Depositional Packages 1 to 4 (Thorne, 2015a–d). Dolerite sills are particularly extensive on the Edmund and Mount Egerton 1:250 000 map sheets and also occur on the northern parts of the Mount Phillips and Robinson Range 1:250 000 map sheets. Minor occurrences have also been mapped on northwestern and southwestern Calyie and within the Mangaroon Syncline on Mangaroon (Fig. 2).

Throughout the Wanna and Mangaroon Synclines, the sills attain a maximum composite thickness of about 1000 m and intrude mixed siliciclastic and dolomitic rocks of the Edmund Group, inflating the stratigraphy by up to

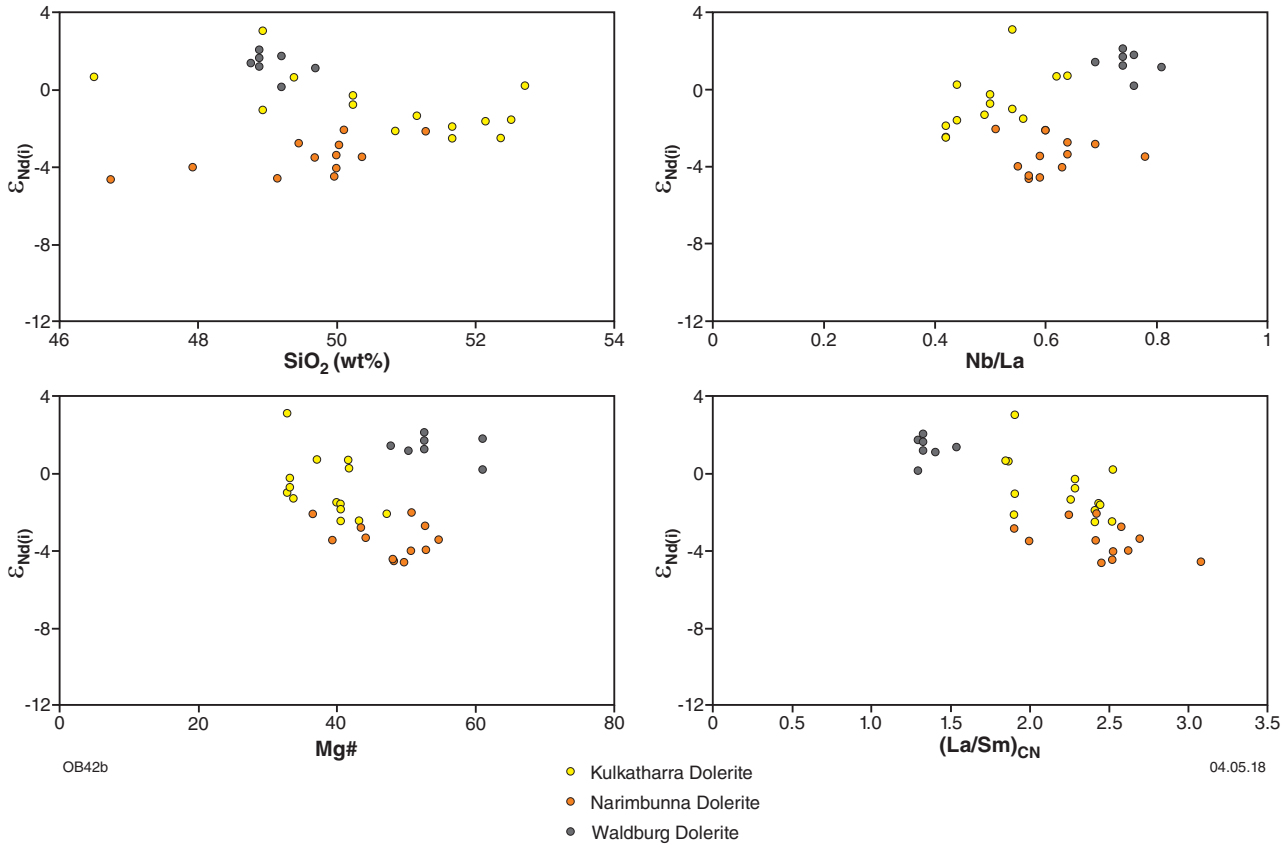

Figure 13. Binary variation diagrams of $\varepsilon_{Nd(i)}$ vs SiO_2, Nb/La, Mg# and $(La/Sm)_{CN}$, examining characteristic correlations as geochemical proxies for crustal contamination of dolerite sill groups. Note that $\varepsilon_{Nd(i)}$ is calculated using initial $^{143}Nd/^{144}Nd$ values corrected to the specified age (i.e. the $^{143}Nd/^{144}Nd$ ratio at the time of crystallization)

200% (Blay et al., 2015a). Farther south, within the Cobra Syncline on Mount Augustus, and within the Resolution West Syncline on Candolle, the sills are 600–700 m thick, progressively reducing in thickness (100–500 m) towards the eastern part of the Edmund Basin. The sills have a maximum total thickness of about 500 m within the Hells Doorway Syncline on Mount Egerton, about 350 m within the Range Creek Syncline on Mulgul and up to 150 m within the Mingah Springs Anticline on Calyie. Reflecting the orientation of regional-scale fold hinges throughout the Edmund Fold Belt, the sills mostly trend northwesterly; although, within the Resolution West and Resolution East Synclines on Candolle and Mount Egerton, they trend northeasterly (Fig. 2). The Narimbunna Dolerite is mainly exposed as pebbly to bouldery colluvium or as blocky rounded outcrops that locally form pinnacles or columns on low ridges and flat hills. The dolerite also outcrops in stream beds and on riverbanks or at the foot of low slopes. The rocks are commonly fractured or cleaved and strongly weathered, with spheroidal weathering in places.

Narimbunna Dolerite sills were emplaced into sedimentary rocks at all stratigraphic levels within the Edmund Group below the Coodardoo Formation (the uppermost unit of Depositional Package 4). Although most sills are locally conformable with bedding, they are regionally discordant along strike, and locally step upwards through the stratigraphy (Martin et al., 2005). Throughout the Edmund Basin, sill contacts with host rocks are sharp

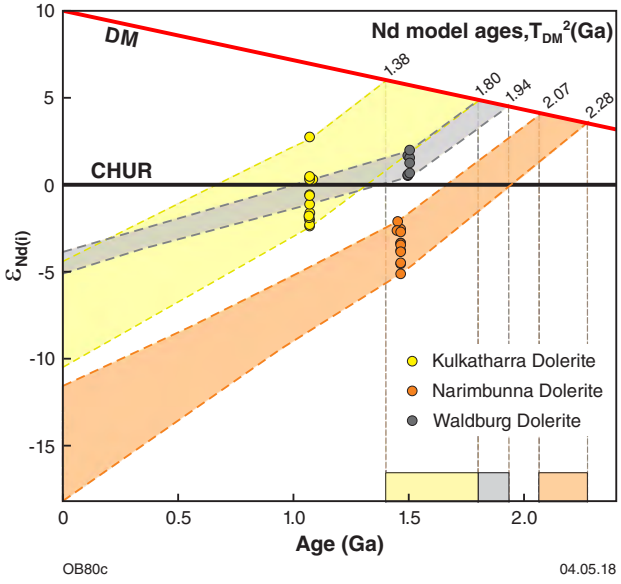

Figure 14. Nd isotope evolution diagram comparing the isotopic evolution of the Kulkatharra, Narimbunna and Waldburg Dolerites and indicating the range of two-stage depleted-mantle model ages (T_{DM}^2) in giga-annum (Ga) for each suite. Abbreviations: DM, depleted mantle; CHUR, chondritic uniform reservoir. Sm–Nd isotope data are compiled in Appendix 4

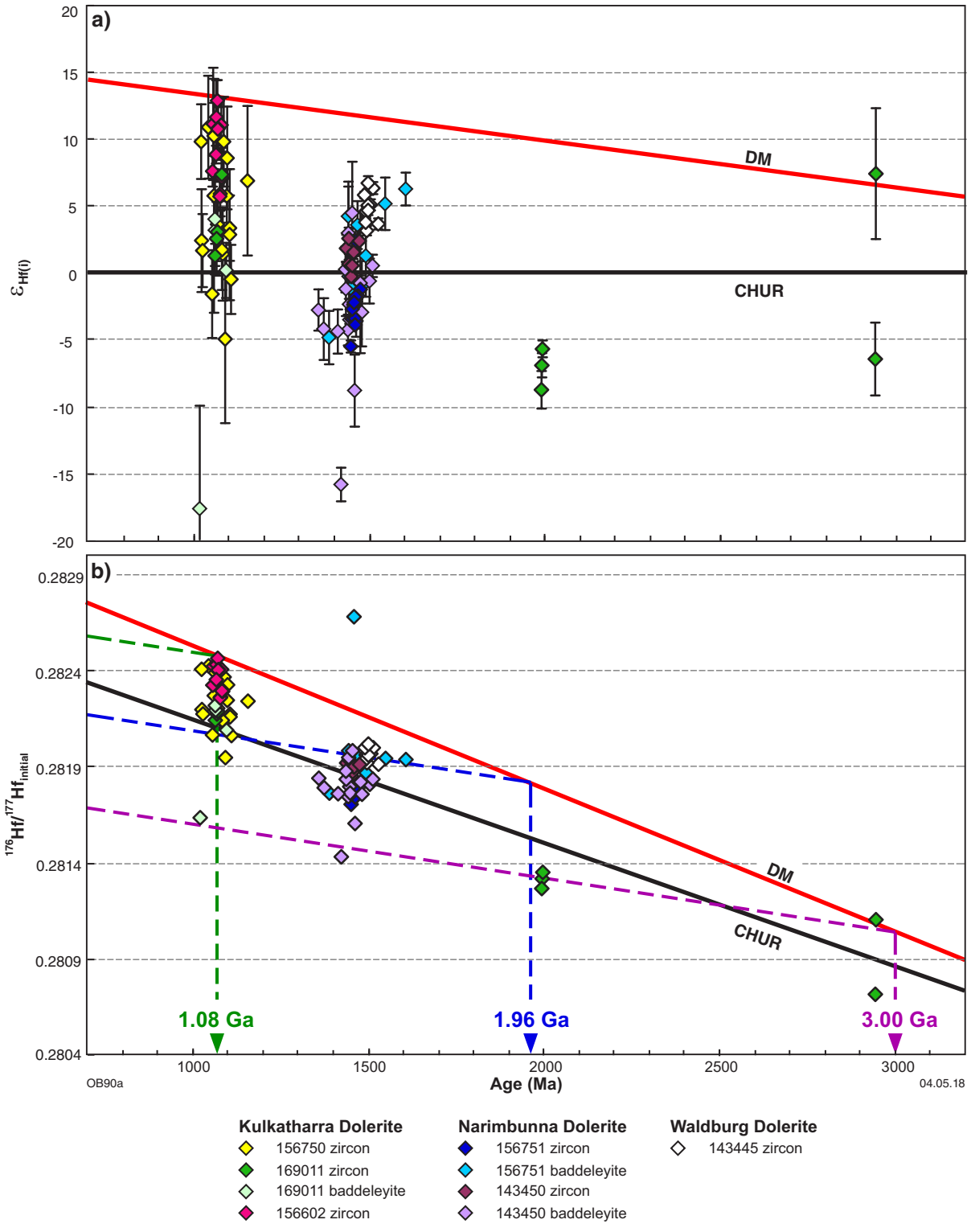

Figure 15. a), b) Hf isotope evolution diagrams for zircon and baddeleyite from the Waldburg, Narimbunna and Kulkatharra Dolerites; b) the arrows indicate depleted-mantle model ages, (as discussed in the text) for each dolerite sill suite. Abbreviations: DM, depleted mantle; CHUR, Chondritic Uniform Reservoir. Lu–Hf isotope data are compiled in Appendix 5

with (generally poorly exposed) chilled margins and 'baked' sedimentary rocks and, in some cases, are characterized by contact metamorphic aureoles metres to decimetres thick (depending on sill thickness and host-rock composition). The metamorphic aureoles are defined mainly by silicification and recrystallization to form hornfels. In some cases, contacts are marked by folding or brecciation of the host rocks. Quartz veins and locally brecciated Fe-oxide mineral phases are also associated with the contact zones and are present within both the sedimentary rocks and the dolerite. Rare variscite veinlets are also present within bleached sedimentary rocks close to the contact zones.

Petrography

The Narimbunna Dolerite is typically moderately to strongly altered which distinguishes Narimbunna sills from those of the younger and less altered Kulkatharra Dolerite (e.g. Wingate, 2002). The Narimbunna Dolerite consists of greenish, medium-grained to very coarse-grained, intergranular mesocratic dolerite or gabbro which locally exhibits igneous layering or a foliation. Locally, the dolerite contains irregular enclaves or veins of very coarse-grained to pegmatitic leucogabbro (Fig. 16a) up to 70 cm across which are interpreted as late-stage differentiates of the mafic magma. Commonly, these late-stage leucogabbros contain magmatic zircon and baddeleyite which have been targeted for geochronology. The central portions of sills are generally medium grained to very coarse grained; although, close to the upper contact, the sill margins are typically fine grained, locally chilled and, in places, composed of aphyric dolerite that may contain amygdales, vesicles or spherical-to-ovoid varioles up to 1.5 cm in diameter. Varioles are typically filled with bladed pale green amphibole and chlorite. The rims of some varioles are marked by a higher concentration of granular opaque oxide minerals. Interstices contain minor late-stage alkali feldspar, quartz, chlorite and acicular apatite (Morris and Pirajno, 2005), whereas chilled margins of amygdaloidal dolerite contain amygdales filled with aggregates of zoned K-feldspar and coarsely crystalline quartz, chlorite, epidote and carbonate (Martin et al., 2005).

The Narimbunna Dolerite is composed principally of about 50–65% plagioclase (oligoclase–labradorite, $An_{28–64}$) and 30–45% pyroxene — the latter consisting mainly of clinopyroxene (augite and, less commonly, pigeonite) and, locally, up to 10% orthopyroxene–hypersthene. Also up to 10% of fine-grained interstitial quartz–feldspar granophyre is commonly present; up to 8% ilmenite–magnetite–leucoxene–maghemite; about 1% dark olive-green hornblende; and minor olivine. Accessory minerals include quartz, alkali feldspar, apatite, zircon, baddeleyite and very fine-grained radioactive inclusions in amphibole. Muhling and Brakel (1985) reported an unusual dolerite sill on the Robinson Range 1:250 000 map sheet that has a high proportion of plagioclase near its upper contact.

The Narimbunna Dolerite typically displays intergranular and subophitic to less common ophitic textures in which both plagioclase and pyroxene typically form extensively altered prismatic crystals (Fig. 16b,c). Pyroxene forms granular, anhedral to subhedral prisms 0.2 – 7 mm long

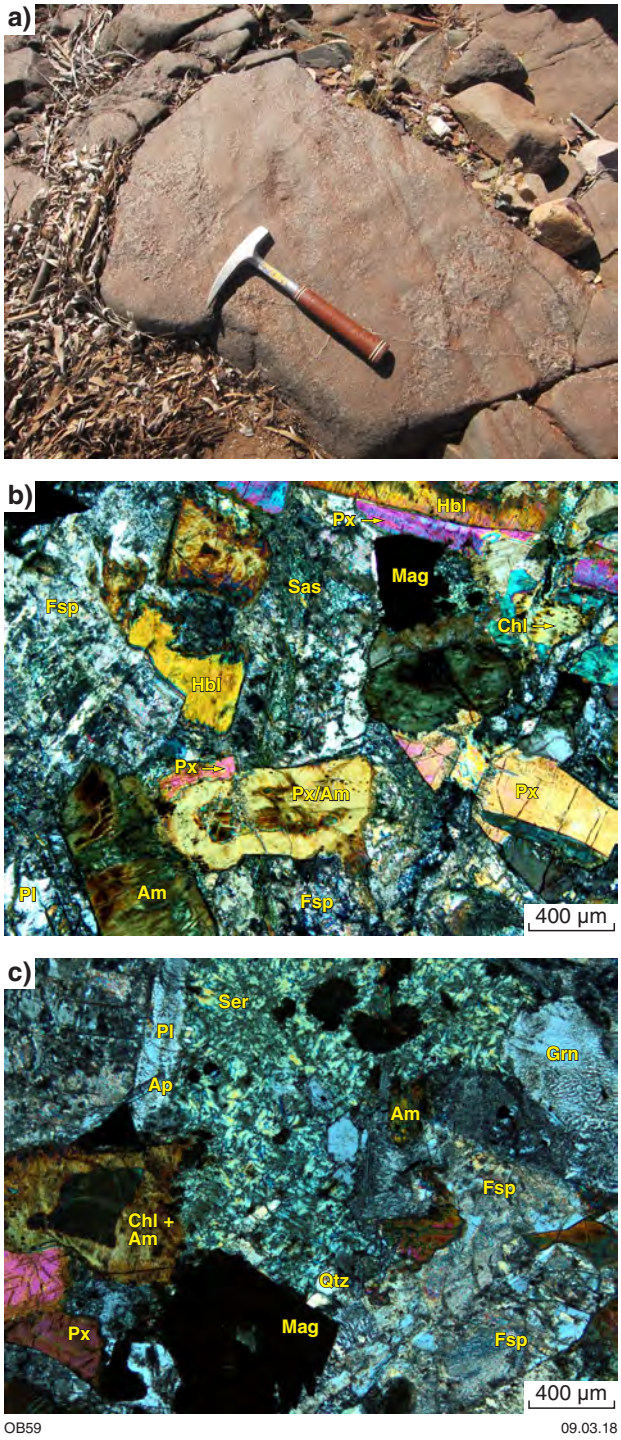

Figure 16. Images of Narimbunna Dolerite sample GSWA 206918: a) coarse-grained dolerite sill containing irregular enclaves of coarse-grained to pegmatitic leucogabbro; b) a photomicrograph (cross-polarized light) showing intergranular texture and intensive alteration, with pyroxene (Px) strongly overgrown by dominant amphibole (Am), chlorite (Chl) and hornblende (Hbl). Plagioclase (Pl) and partly recrystallized feldspar (Fsp) are intensively replaced by fine-grained aggregates of mainly saussurite (Sas) and amphibole + chlorite; c) a photomicrograph (crossed-polarized light) showing granophyric intergrowths (Grn) interstitial to intensively altered feldspar and most sericite-altered plagioclase (Ser); cross-polarized light. Abbreviations: Mag, magnetite; Qtz, quartz; Ap, apatite

that are typically unzoned. Muhling and Brakel (1985) recorded pigeonite inverted to orthopyroxene containing exsolved blebs of calcic clinopyroxene. Pyroxene encloses subhedral to euhedral prisms of plagioclase from 2 to 8 mm long. Locally, plagioclase laths are partly enclosed by euhedral opaque iron–titanium oxide minerals. Some plagioclase grains are zoned, with calcic cores. Pyroxene commonly nucleated on plagioclase, perhaps due to local enrichment in ferromagnesian components as plagioclase depleted the adjacent liquid in Ca, Al, and Si. The order of crystallization is likely plagioclase ± olivine followed by high-Ca pyroxene + plagioclase fractionation, late magnetite or titanomagnetite, and finally quartz + low-Ca feldspar. This sequence is reflected in the variation trends of major oxides and Cr, Ni, and Sc/V versus Mg# (Fig. 12a,b). The typical tholeiitic trend represented in the AFM diagram in Figure 7 indicates that fractionation was controlled by early olivine and pyroxene crystallization (decreasing MgO) and that magnetite was fractionated late (increasing FeO).

Plagioclase is locally replaced by green, recrystallized fibrous amphibole, as well as chlorite, albite, saussurite, sericite and epidote, particularly along cleavage and twin planes. Pyroxene is replaced by blue–green hornblende, fibrous uralitic tremolite, as well as chlorite, minor biotite, and sericite (Fig. 16b,c). There is a well-developed alteration zonation locally on the margins and along the cleavage planes of clinopyroxene crystals. Rare bastite pseudomorphs of orthopyroxene contain unaltered clinopyroxene blebs (Muhling and Brakel, 1985). Subhedral to dendritic or skeletal opaque oxide minerals are up to 6 mm long and contain ilmenite lamellae surrounded by polycrystalline leucoxene or maghemite. Fine-grained anhedral crystals and aggregates of probable late-stage magnetite are also present. Alkali feldspar forms equant anhedral grains which are interstitial to plagioclase and pyroxene. Apatite needles are present in plagioclase and quartz, whereas zircon and baddeleyite are present within chlorite and plagioclase. Very fine-grained radioactive inclusions of unknown composition are present within hornblende and recrystallized fibrous amphibole (Wingate, 2002).

Very coarse-grained to pegmatitic gabbro lenses typically contain anhedral to subhedral plagioclase prisms up to 3 cm long, together with granular to prismatic, subhedral to euhedral pyroxene up to 10 mm long. The finer grained minerals (Fig. 16c) typically include euhedral opaque oxide minerals, 10–15% interstitial quartz–feldspar (probably albite) granophyre, acicular apatite and fine-grained minerals surrounded by pleochroic haloes. Accessory phases include zircon and baddeleyite. The primary mineral phases are extensively altered, with sericite, albite, chlorite and saussurite aggregates developed in plagioclase; and brownish-green fibrous amphibole, greenish chlorite, and leucoxene over pyroxene.

On Marquis, the dolerite sills contain extensive talc and iron–titanium oxide pseudomorphs after olivine, which are now surrounded by hypersthene. Plagioclase is variably altered to saussurite and pyroxene is locally altered to actinolite.

Geochronology

Five Narimbunna Dolerite sills are dated at 1465–1450 Ma (Fig. 3; Table 1) based on SHRIMP analysis of magmatic zircons and baddeleyites extracted from medium- to coarse-grained dolerite or pegmatitic leucogabbro. A crystallization age of 1450 ± 5 Ma was obtained from zircons extracted from a medium-grained dolerite (GSWA 189223, Wingate et al., 2013b) intruded into Depositional Package 4 (Discovery Formation) on Milgun, about 3.5 km south-southeast of Mount Arapiles. About 53 km to the west, on Marquis, a similar medium-grained dolerite sill (GSWA 189224, Wingate et al., 2014) intruded into Depositional Package 3 (Kiangi Creek Formation) yielded only two baddeleyite crystals and a poorly defined date consistent with a crystallization age of c. 1450 Ma. On Candolle, zircon and baddeleyite from a medium- to coarse-grained granophyric dolerite, also within the Kiangi Creek Formation, provided a crystallization age of 1452 ± 5 Ma (GSWA 143450, Wingate et al., 2012c). Zircons from a quartz–K-feldspar leucogabbro patch within a sill in Depositional Package 4 (Ullawarra Formation) on Elliott Creek indicated a crystallization age of 1449 ± 5 Ma (sample WANH, Wingate, 2002). Excluding the imprecise result for GSWA 189224, the three reliable ages are in good agreement and yield a weighted mean $^{207}Pb^*/^{206}Pb^*$ age of 1450 ± 3 Ma (MSWD = 0.53).

Zircon and baddeleyite from the fifth sample, a medium- to coarse-grained dolerite intruded into Depositional Package 4 (Discovery and Devil Creek Formations), on Mangaroon, yielded a crystallization age of 1465 ± 3 Ma (GSWA 156751, Nelson, 2001b; Wingate, 2002). This result is about 15 Ma older than the other samples, suggesting that this sill represents a separate intrusive event.

Geochemistry

Alteration

The Narimbunna Dolerite is characterized by moderate-to-high (average = 2.72%) LOI values (Appendix 1) suggesting significant postmagmatic alteration. Titanium and Zr are moderately positively correlated, whereas there is no correlation between Ti/Zr and LOI. This, together with the relatively minor variation in Ti/Zr, regardless of volatile content (Fig. 6), indicates that both Ti and Zr were not significantly affected by postmagmatic processes. Similarly, Zr shows a positive correlation with HFSE and REE (Fig. 6), suggesting that they have also not been significantly modified. This is in contrast to the LILE, which exhibit significantly larger variations between Na_2O, K_2O, Rb, Sr, Cs, Ba, and Zr. In addition, the LILE (e.g. K_2O, Rb, Ba) typically exhibit greater dispersions with higher LOI (Fig. 6, Appendix 2) which suggests mobility during alteration. Morris and Pirajno (2005) noted that the covariance of immobile element pairs (e.g. Zr and Y) with other elements including the LILE suggests that some elemental variation may be due to crustal contamination rather than postmagmatic alteration.

Major, trace and rare earth element composition

The Narimbunna Dolerite can be classified mostly as high-Fe tholeiitic basalt in various discrimination diagrams (Figs 7–9). It has a relatively wide range of major and trace-element compositions (Table 2; Appendix 1), with generally low-to-moderate SiO_2 (average 49.49%), K_2O (average 0.89%), P_2O_5 (average 0.21%) and Na_2O (average 2.12%); moderate concentrations of MgO (average 6.16%); moderate-to-high CaO (average 9.68%); and very variable Mg# values (35.68 – 60.23, average = 47.74). Chromium concentrations are extremely variable; on average, relatively high (16–542 ppm, average = 150 ppm). Copper content is typically low at 9–144 ppm, with an average of 98 ppm (Table 2).

Compared to the Waldburg and Kulkatharra Dolerites, the Narimbunna Dolerite has a distinctive range of REE and HFSE concentrations (Fig. 10; Table 2; Appendices 3a,b). It is moderately enriched in most REE and HFSE; for example, La (7.97 – 29.51 ppm, average = 15.98 ppm), Yb (1.33 – 4.03 ppm, average = 2.45 ppm) and Nb (4.8 – 18.8 ppm, average = 10.1 ppm) as detailed in Table 2. Light REE are generally mildly enriched relative to heavy REE and show a range of moderate-to-high, negatively sloping, primitive mantle-normalized REE–HFSE profiles (Fig. 10) with $(La/Yb)_N$ = 3.11 – 6.81 (Appendix 1). Primitive mantle-normalized REE values typically indicate weak-to-moderate fractionation with $(La/Sm)_N$ = 1.56 – 3.09, whereas the heavy REE are weakly fractionated with $(Gd/Yb)_N$ = 1.39 – 1.83. Positive correlations between Zr and La/Sm, and Th/Tb (Appendix 3a) display relatively shallow trends, indicating that fractionation is likely to be the main process responsible for magmatic differentiation. Appendix 1 shows that moderate REE enrichment, coupled with typically low La/Nb ratios (1.28 – 2.05), may indicate more extensive fractionation of a relatively uncontaminated magma (Howard et al. 2007). The primitive mantle-normalized REE–HFSE profiles are marked by relatively strong negative Nb anomalies (Fig. 10) and Eu/Eu* values between 0.80 and 1.42, with an average Eu/Eu* of 1.05 (Appendix 1).

Similar to the Waldburg Dolerite, the Narimbunna Dolerite shows positive correlations between Mg# and Al_2O_3, CaO, Cr, Ni, Sc/V, and CaO/Al_2O_3 in Harker variation diagrams, whereas $Fe_2O_3^T$, TiO_2, and P_2O_5 exhibit a strong negative correlation (Fig. 12a,b). Increasing $Fe_2O_3^T$ and decreasing Al_2O_3 with decreasing Mg# indicate that olivine + plagioclase were involved in magma crystallization. The trends shown in Figure 12a,b suggest that fractionation was initially controlled by olivine (positive correlation between Mg# and Ni) then pyroxene and finally by plagioclase crystallization (Mg# vs Ca, Cr, Sc/V). Moderate-to-strong positive correlations between Mg# and Sc/V (Fig. 12b), coupled with a relatively wide range in Cr concentrations (Table 2), suggest fractional crystallization of clinopyroxene (Wang et al., 2014). Negative correlations between Mg# and TiO_2 and $Fe_2O_3^T$ indicate that magnetite or titanomagnetite were not major fractionating phases. The AFM diagram (Fig. 7) also shows a tholeiitic trend, implying that fractionation was controlled by early olivine and clinopyroxene fractionation (decreasing MgO), and that magnetite was fractionated late (increasing FeO). Inferences from geochemical trends agree with petrographic observations and are consistent with fractionation as a major control on geochemical composition, whereas the variation in Cr/Ti and V/Zr ratios (Appendix 1) can be explained by fractionation of pyroxene (Pearce and Cann, 1973; Pearce, 1975; Nesbitt et al., 1984; Wilson, 1989). Positive correlation of CaO/Al_2O_3 and Al_2O_3/TiO_2 ratios with Mg# (Fig. 12b) indicates that olivine fractionation alone cannot explain the major element variations and may signify the influence of partial melting (Stracke et al., 2003).

Isotope analyses

Narimbunna Dolerite whole-rock samples indicate a narrow range of $^{143}Nd/^{144}Nd_{(i)}$ ratios, from 0.510507 to 0.510656; $\varepsilon_{Nd(i)}$ values from –2.07 to –4.64 (Appendix 4); and model ages (T_{DM}^2) between 2.28 and 2.07 Ga with a median of 2.19 Ga (Fig. 14).

Zircon and baddeleyite Lu–Hf analyses (Appendix 5) were conducted on samples from two dolerite sills (GSWA 156751 and 143450; Fig. 15a). For GSWA 156751, thirteen analyses were conducted on 13 zircons and nine analyses on nine baddeleyite crystals. The zircons have a range of initial $^{176}Hf/^{177}Hf$ compositions from 0.281706 to 0.281920, corresponding to dispersed $\varepsilon_{Hf(i)}$ values between 2.4 and –5.5 (Fig.15a,b; Appendix 5) and depleted-mantle model ages (T_{DM}) between 2.19 and 1.88 Ga (Appendix 5). Baddeleyites from the same sample indicate initial $^{176}Hf/^{177}Hf$ compositions from 0.281764 to 0.281985, which correspond to a range of dispersed $\varepsilon_{Hf(i)}$ values between 6.3 and –4.8 (Fig.15a,b; Appendix 5) and depleted-mantle model ages between 2.48 and 1.94 Ga (Appendix 5).

For GSWA 143450, nine zircons and 16 baddeleyites were analysed (Appendix 5). The zircons have a range of initial $^{176}Hf/^{177}Hf$ compositions from 0.281853 to 0.281938, corresponding to $\varepsilon_{Hf(i)}$ values between 2.6 and –0.3 (average = 1.2) and depleted-mantle model ages between 2.23 and 2.05 Ga. Initial $^{176}Hf/^{177}Hf$ compositions for baddeleyite from the same sample have a similar range to the zircons, from 0.281433 to 0.281985 (Fig. 15b; Appendix 5), which correspond to a range of $\varepsilon_{Hf(i)}$ values between 4.5 and –15.8 (average = –2.7) and depleted-mantle model ages between 2.49 and 1.74 Ga (Appendix 5). The Narimbunna Dolerite can be modelled as originating from sources extracted from the mantle at c. 3.0 and 1.96 Ga but perhaps without a juvenile mantle component at c. 1.46 Ga (Fig. 15b).

Lu–Hf model age ranges for zircon and baddeleyite from both samples fully overlap (Fig. 3), although the Lu–Hf results (particularly for baddeleyite) are relatively imprecise and dispersed. The median Lu–Hf model age of 2.05 Ga is younger than the median Nd model age of 2.19 Ga (Fig. 3).

The results from both isotope systems indicate that the Narimbunna Dolerite was derived from a radiogenic source between depleted mantle and CHUR that interacted with significant amounts of evolved (or old) crustal material, either in the source region or by crustal contamination. The Hf isotope compositions are comparable to those of felsic rocks in the underlying Gascoyne Province basement (Johnson et al., 2017). However, geochemical

proxies for crustal contamination, including positive or negative correlations between $\varepsilon_{Nd(i)}$ and SiO_2, $(La/Sm)_{CN}$ Nb/La, and Mg# (e.g. Morris and Pirajno, 2005; Wang et al., 2014), do not yield arrays consistent with significant crustal contamination (Fig. 13). Therefore, it is possible that the isotope compositions reflect heterogeneity in the composition of the mantle source region.

Summary

The Narimbunna Dolerite consists of moderately to distinctly altered, medium- to coarse-grained, equigranular dolerite, locally containing veins or irregular patches of very coarse-grained to pegmatitic leucogabbro. Plagioclase and pyroxene are the primary minerals and are extensively replaced by low- to medium-grade metamorphic minerals, typically amphibole, chlorite, hornblende and tremolite. Crystallization ages for dated sills range from c. 1465 to 1449 Ma, with three samples yielding a mean age of 1450 ± 3 Ma. One sample that yielded a significantly older age of 1465 ± 3 Ma may represent a separate episode of dolerite intrusion. Narimbunna Dolerite samples yield moderate but highly variable Cr–Ni concentrations and MgO contents of 4.46 to 8.51 wt%. They are light REE-enriched with average La/Sm = 3.68 versus a weakly fractionated heavy REE (average Gd/Yb = 1.86) and low La/Nb ratios (average = 1.6) with a slight negative Nb anomaly. Their chemistry indicates relatively extensive fractionation of either a relatively uncontaminated magma or insignificantly enriched mantle source. However, both Sm–Nd and Lu–Hf isotope data suggest that the mafic rocks were derived from a radiogenic source between depleted mantle and CHUR but which interacted with significant amounts of older evolved crustal material, either in the source or emplacement region; whereas Hf isotope compositions are comparable to those of felsic rocks in the underlying Gascoyne Province basement.

Kulkatharra Dolerite

The Kulkatharra Dolerite comprises voluminous, laterally continuous (up to 210 km long) dolerite sills (Fig. 2) emplaced within sedimentary rocks of the Edmund and Collier Groups (Wingate, 2002; Blay et al., 2015b). The sills are particularly extensive on the Pingandy Shelf, as well as within the core and along the northern limb of the Wanna Syncline on the Edmund, Mount Egerton, Collier, and Turee Creek 1:250 000 map sheets. In the western Capricorn Orogen, the sills attain a maximum thickness of 450 m, whereas in the eastern part, they may be up to 600 m thick. Although the sills generally trend in a northwesterly direction, their orientation is principally controlled by the orientation of regional fold axes, so in the central and eastern parts of the orogen (e.g. on Cardawan, Three Rivers, Lofty Range, and Ilgarari), the sills trend easterly to northeasterly. Although most sills are locally conformable with the host sedimentary rocks, they are regionally discordant along strike and are characterized by step-and-stair geometry (Martin et al., 2005). The dolerite sills are exposed as rounded boulders and blocky outcrops on low ridges and flat hills, in stream beds and saddles, or on hill slopes. They are commonly very ferruginous on weathered surfaces.

Kulkatharra Dolerite sills were emplaced into sedimentary rocks dominated by fine-grained siliciclastic and dolomitic successions within both the Edmund and the Collier Groups. However, intrusions within the Edmund Group — Depositional Packages 1–4 (Thorne, 2015a–d) — are only evident in the northwestern part of the Capricorn Orogen. Elsewhere, the Kulkatharra Dolerite intrudes across large areas of the Collier Group — Depositional Packages 5 and 6 (Thorne, 2016a,b) — which is dominated by siltstone of the Ilgarari Formation on Calyie and Three Rivers. It also intrudes across siltstone to fine-grained sandstone of the Backdoor Formation on Cardawan. On Lofty Range and Ilgarari, the dolerite sills intrude dolomite, siltstone and fine-grained sandstone of the Backdoor and Calyie Formations. Most intrusive contacts with the host sedimentary rocks are sharp, with the dolerites locally showing chilled margins with a recrystallized interstitial matrix. The rock increases in grain size towards the centres of sills to become medium- to coarse-grained, equigranular dolerite. In rare cases, dolerite margins show macro-scale textures, such as peperite, amygdales and plastically deformed fragments of host sedimentary rocks. This implies that some of the sills were emplaced at relatively shallow depths, possibly into variably lithified sedimentary rocks (Martin, 2003; Morris and Pirajno, 2005). The host sedimentary rocks typically show up to several metres of silicification and recrystallization to hornfels (Martin et al., 2005). Commonly, sedimentary rocks immediately above dolerite sills display distinctive saprolitic and Fe-oxide alteration or, close to the contact, are locally silicified and ferruginous, forming dark grey or black fine-grained rocks. Key features include fine-grained amygdaloidal and vesicular tops to the dolerite sills (Daniels, 1969); rare plastically deformed fragments of the surrounding sedimentary rocks with inclusions of those rocks within dolerite (Muhling and Brakel, 1985); rare peperitic textures with associated fluidized sediments (Martin et al., 2005); and locally disharmonically folded and brecciated sedimentary rocks. Quartz veins, quartz-vein breccia and rare calcite veins are also associated with contact zones (Martin et al., 2005).

On Mount Vernon (e.g. Zone 50, MGA 626485E 7330225N), unusual features associated with the intrusion of fine- to medium-grained dolerite into recrystallized, interlayered dolomite and silicified dolomitic siltstone are preserved. About 4 m from the contact (not exposed), the dolomitic siltstone is veined by numerous fine-grained, unevenly coloured, dark grey veins (up to 5 cm wide) that are either layer-parallel, or which crosscut the sedimentary rocks. On the top surfaces of the dolomitic siltstone beds, the veins are preserved as leaf-shaped marks that resemble inverted flute casts (Fig. 17a). Petrography, supported by HyLogger-3 hyperspectral analyses, indicates the presence of prehnite, possibly after Ca-pyroxene (Fig. 17b–d). The veins have chilled margins up to 1–3 mm wide and the adjacent sedimentary rocks are locally metamorphosed to hornfels. The veins and leaf-shaped features possibly represent apophyses of the dolerite sill which were emplaced along bedding planes and fractures in the sedimentary rocks.

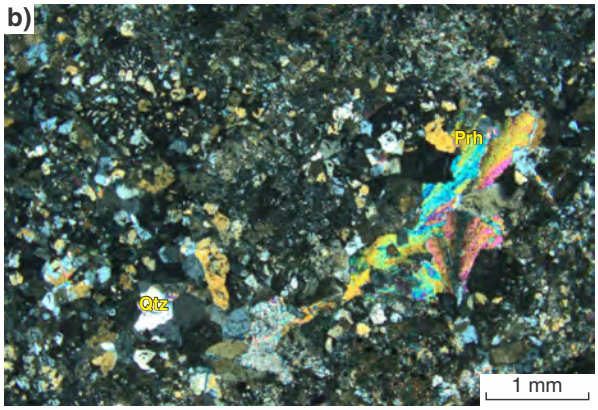

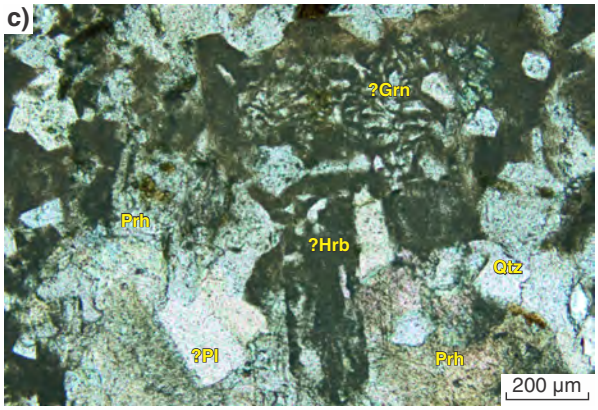

d)

Shortwave-infrared (SWIR)		Thermal-infrared (TIR)		
Min1 sTSAS	Min2 sTSAS	Min1 uTSAT	Min2 uTSAT	Min3 uTSAT
NULL	NULL	NULL	NULL	NULL
NULL	NULL	NULL	NULL	NULL
NULL	NULL	NULL	NULL	NULL
NULL	NULL	NULL	NULL	NULL
NULL	NULL	NULL	NULL	NULL
Prehnite	Actinolite	Quartz	Labradorite	Hornblende
Prehnite	Actinolite	Quartz	Hornblende	Prehnite
Prehnite	Actinolite	Quartz	Hornblende	Prehnite
Prehnite	NULL	Quartz	Hornblende	Prehnite
Prehnite	Actinolite	Quartz	Hornblende	Prehnite
Prehnite	Actinolite	Quartz	Hornblende	Prehnite
Prehnite	Actinolite	Quartz	Hornblende	Prehnite
NULL	NULL	NULL	NULL	NULL
NULL	NULL	NULL	NULL	NULL
Prehnite	NULL	Quartz	Hornblende	Prehnite
Prehnite	NULL	Quartz	Hornblende	Prehnite
Prehnite	NULL	Quartz	Oligoclase	Prehnite
Prehnite	NULL	Quartz	Oligoclase	Prehnite
Prehnite	NULL	Quartz	Oligoclase	Prehnite
Prehnite	NULL	Quartz	Oligoclase	Prehnite
Prehnite	NULL	Quartz	Oligoclase	Prehnite
Prehnite	NULL	Quartz	Labradorite	Prehnite
NULL	NULL	NULL	NULL	NULL
NULL	NULL	NULL	NULL	NULL
NULL	NULL	NULL	NULL	NULL

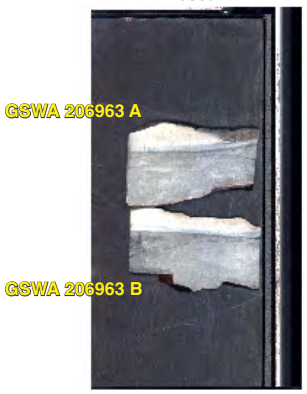

Min1 sTSAS	Min2 sTSAS	Min1 uTSAT	Min2 uTSAT	Min3 uTSAT
NULL	NULL	NULL	NULL	NULL
NULL	NULL	NULL	NULL	NULL
NULL	NULL	NULL	NULL	NULL
NULL	NULL	NULL	NULL	NULL
NULL	NULL	NULL	NULL	NULL
NULL	NULL	NULL	NULL	NULL
NULL	NULL	NULL	NULL	NULL
NULL	NULL	NULL	NULL	NULL
NULL	NULL	NULL	NULL	NULL
Prehnite	Actinolite	Amphibolite ML48	Quartz	Prehnite
Prehnite	Actinolite	Quartz	Hornblende	NULL
Prehnite	Actinolite	Quartz	Albite	Prehnite
Prehnite	Hornblende	Quartz	Albite	Prehnite
NULL	NULL	NULL	NULL	NULL
NULL	NULL	NULL	NULL	NULL
Prehnite	Actinolite	Quartz	Hornblende	Bytownite
Prehnite	NULL	Quartz	Albite	Prehnite
Prehnite	NULL	Quartz	Albite	Prehnite
Prehnite	NULL	Quartz	Albite	Prehnite
NULL	NULL	NULL	NULL	NULL
NULL	NULL	NULL	NULL	NULL
NULL	NULL	NULL	NULL	NULL
NULL	NULL	NULL	NULL	NULL
NULL	NULL	NULL	NULL	NULL
NULL	NULL	NULL	NULL	NULL
NULL	NULL	NULL	NULL	NULL

OB61 08/03/18

Figure 17. Sedimentary rocks on Mount Vernon crosscut by a network of fine-grained intrusive veins: a) leaf-shaped features on the top surface of a dolomitic siltstone bed, about 4 m from the contact with the dolerite sill (GSWA 206963); b) a photomicrograph (cross-polarized light) of a prehnite (Prh) veinlet crosscutting silicified groundmass; c) a photomicrograph (plane-polarized light) of a leaf-shaped vein showing an extensively altered intrusive rock with faint remnants of primary mineral phases; Prh, prehnite; Qtz, quartz; Grn, granophyric intergrowths; Hbl, hornblende; Pl, plagioclase; d) HyLogger-3 hyperspectral analyses (Hancock et al., 2013) in SWIR (shortwave-infrared) and TIR (thermal-infrared) of the leaf-shaped veins in samples GSWA 206963A and GSWA 206963B

Petrography

Kulkatharra Dolerite sills are typically relatively unaltered, fine to very fine grained at the margins, gradually increasing in grain size to become medium or coarse grained in the centres. The rock is typically massive quartz dolerite with intergranular to locally porphyritic (with phenocrysts of clinopyroxene and plagioclase) textures. Central and upper parts of the sills commonly contain coarse-grained to pegmatitic granophyric segregations and were preferentially targeted for geochronology.

The rocks exhibit equigranular, intergranular textures with subophitic and minor ophitic areas, and patchy glomerocrysts of plagioclase, pyroxene and opaque minerals. The primary mineral assemblage is typically plagioclase (40–60%) and clinopyroxene (30–50%), although plagioclase may locally form up to 90% of the rock. Plagioclase and pyroxene (typically augite) are intergrown with interstitial, granular, late-magmatic quartz (~5%); quartz–K-feldspar granophyre (5–20%); clouded K-feldspar (<5%); a very fine-grained crystalline matrix (5–35%); hornblende (<5%); rare biotite flakes (1–3%); and irregular opaque minerals (5–20%) (Fig. 18a). Accessory phases include apatite, zircon, baddeleyite, traces of clinozoisite and epidote, minor titanite, and very fine-grained radioactive minerals typically associated with biotite or chlorite. Disseminated irregular sulfide blebs or skeletal inclusions up to 6 mm in diameter are present locally.

Plagioclase (oligoclase–labradorite, $An_{32–62}$) forms anhedral to subhedral, equant to elongate prisms, or less commonly, xenomorphic crystals up to 7 mm long, which are typically albite-twinned or zoned. Plagioclase is generally moderately to intensely altered to sericite and saussurite, or rarely overgrown by dusty epidote, clinozoisite, prehnite, and carbonate (typically calcite). On Peedawarra, the sills locally are extensively altered and some contain plagioclase–quartz–?hornblende segregations overprinted by calcite–chlorite ± iron–titanium oxide assemblages (Fig. 18b).

Clinopyroxene (mainly augite) forms xenomorphic grains, or subhedral equant to elongate prisms up to 5 mm long which are commonly simply twinned (on 100). Some crystals exhibit hourglass zoning, reaction rims and exsolution lamellae of orthopyroxene or pigeonite, or show rare vermicular textures. Clinopyroxene is generally very fresh, although locally it is replaced by dusty amphibole–leucoxene aggregates or Fe-chlorite or, less commonly, by syntaxial pseudomorphs of brownish amphibole. Less commonly, pyroxene and rare epidote grains enclose fine-grained sulfide minerals. Augite may locally be rimmed by green–brown hornblende which, in turn, is partly intergrown with plagioclase or granophyre. Locally, areas of hornblende occur adjacent to pyroxene, with deep blue–green ?hastingsite rimming brown ?titano-pargasite. Less commonly, augite is mantled by pale-green chlorite and biotite. Some dolerite sills contain rounded, prismatic to equant oikocrysts of extensively altered former ?pigeonite or ?olivine (up to 2.5 mm in length) which are completely replaced by rusty brown bowlingite along cracks and cleavage planes.

Locally, extensive areas of mesostasis are interstitial to plagioclase, pyroxene and opaque minerals. Random patches of mesostasis up to 5 mm across exhibit microspherulitic to microgranophyric, granular and granophyric textures. Granophyre is commonly nucleated on euhedral plagioclase laths or clouded K-feldspar. Rare granular late-magmatic quartz is present within granophyric patches and, in places, biotite–chlorite intergrowths are closely associated with magmatic quartz.

Apatite is a common accessory mineral in and adjacent to granophyre and quartz and forms acicular and/or elongate crystals up to 2 mm long, less than 50 µm wide and commonly hollow. Traces of apatite are also found within plagioclase. Opaque minerals, mainly magnetite–ilmenite and minor pyrite, form interstitial grains or aggregates between plagioclase and pyroxene. Individual crystals are up to 6 mm in length and are typically anhedral. Less common dendritic–skeletal grains consist of ilmenite lamellae mantled by magnetite and are variably altered to leucoxene or maghemite.

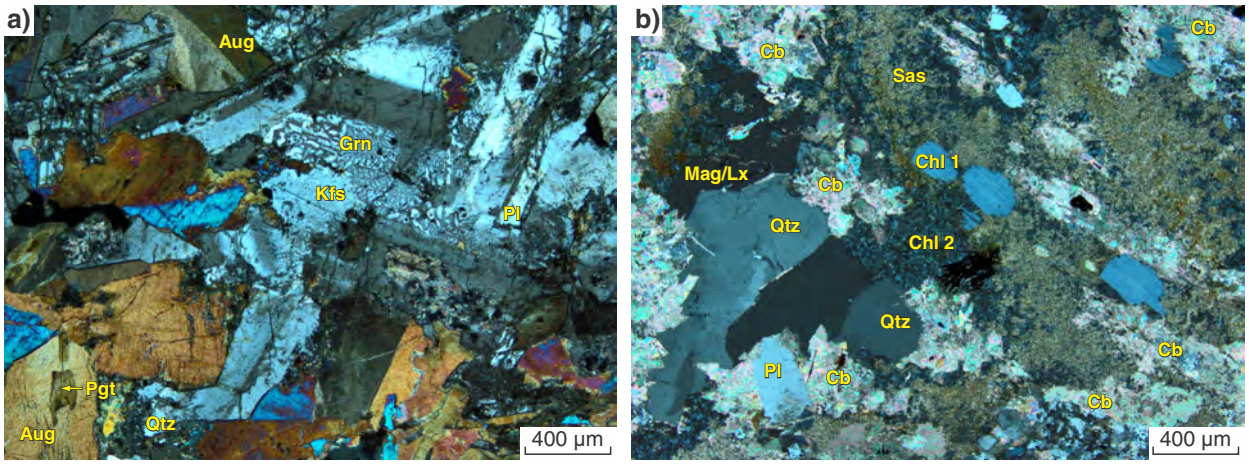

OB60 08/03/18

Figure 18. Photomicrographs (cross-polarized light) of Kulkatharra Dolerite samples: a) relatively unaltered dolerite (GSWA 156750) with subophitic texture; euhedral augite (Aug) crystals, twinned in places (top and bottom left), contain darker domains as irregular cores that may be altered pigeonite (Pgt), as can be seen in the bottom left; granophyric intergrowths (Grn) are interstitial to plagioclase (Pl) and partly altered K-feldspar (Kfs); b) coarse-grained granophyric intergrowths (GSWA 206994) are replaced extensively by carbonate (Cb); short prisms of a primary mineral (?pyroxene) pseudomorphed by chlorite (Chl 1); fine, acicular flakes of chlorite (Chl 2) developed on primary mineral phases interstitial to quartz (Qtz) and carbonate (Cb); magnetite is replaced partly by leucoxene (Mag/Lx)

Geochronology

Six samples of five Kulkatharra Dolerite sills yielded U–Pb crystallization ages of 1083–1067 Ma (Fig. 3; Table 1) using magmatic zircons and baddeleyite crystals extracted from medium- to coarse-grained granophyric quartz dolerite and pegmatitic leucogabbro with coarse-grained granophyric segregations.

On Kenneth Range, a very coarse-grained granophyric segregation (GSWA 156602, Wingate and Bodorkos, 2007), within a coarse-grained dolerite sill intruded into Depositional Package 5 (Backdoor Formation), yielded zircons that gave a crystallization age of 1076 ± 4 Ma. Zircon and baddeleyite from mesostasis-enriched quartz dolerite (GSWA 169011, Nelson, 2001c; Wingate, 2002), intruded into Depositional Package 2 (Blue Billy Formation) on Elliott Creek, yielded a crystallization age of 1071 ± 8 Ma. A medium-grained granophyric quartz dolerite (GSWA 156750, Nelson, 2001a; Wingate, 2002), collected from a sill intruded into Depositional Package 4 (Ullawarra Formation) on Ullawarra, yielded low-uranium baddeleyite crystals that produced a crystallization age of 1068 ± 22 Ma. Baddeleyite and zircon from a medium- to coarse-grained quartz dolerite sill (sample WANC, Wingate, 2002), also intruded into the Ullawarra Formation on Elliott Creek, provided a crystallization age of 1067 ± 14 Ma. The ages of these four samples agree to within uncertainty, yielding a weighted mean $^{207}Pb^*/^{206}Pb^*$ age of 1075 ± 3 Ma (MSWD = 1.1).

Older results were obtained for two samples (GSWA 206994, Wingate et al., 2015c,d; and GSWA 206995) collected about 50 m apart in a sill intruded into Depositional Package 4 (Ullawarra Formation) on Peedawarra. The rock is a highly carbonate-altered, very coarse-grained quartz dolerite to pegmatitic leucogabbro. Despite the strong alteration, the large euhedral zircons are pristine and the two samples yielded weighted mean $^{207}Pb^*/^{206}Pb^*$ dates of 1081 ± 6 and 1084 ± 5 Ma. Combining results for the two samples yields a weighted mean date of 1083 ± 4 Ma (MSWD = 1.1). This is interpreted as the age of crystallization (Fig. 3; Table 1) which is significantly older than the mean 1075 Ma age for the other four sills and may represent the age of a separate intrusive event.

Geochemistry

Alteration

The Kulkatharra Dolerite is typically significantly less altered than the Waldburg or Narimbunna Dolerites. Newly acquired geochemical data, together with those of Morris and Pirajno (2005), show that the dolerites are characterized by relatively low LOI values (average = 1.46 %), suggesting only very limited postmagmatic alteration. Titanium and Zr are positively correlated (Fig. 6), whereas there is no correlation between Ti/Zr and LOI. This, and the relatively minor correlation in Ti/Zr, regardless of volatile content, indicates that both Ti and Zr were not significantly affected by postmagmatic processes (Morris and Pirajno, 2005). Similarly, Zr shows a positive correlation with HFSE and REE (Fig. 6), suggesting that HFSE and REE have also not been significantly modified. Despite the apparent fresh appearance of the rocks, poor correlation between Zr, LOI contents and the LILE demonstrate that the concentrations of these elements have been altered. However, a weak positive correlation between K_2O, Na_2O, Rb, and Ba (Appendix 2) as well as a relatively narrow range of Na_2O/K_2O ratios (Fig. 6) suggest that some element variations may be due to crustal contamination rather than postmagmatic alteration (Morris and Pirajno, 2005).

Major, trace and rare earth element composition

The Kulkatharra Dolerite can be classified mostly as a sub-alkaline, high-Fe tholeiitic basalt (Figs 7–9). In terms of their major, trace and rare earth elements, these rocks have a distinctive geochemical composition compared with that of the Narimbunna and Waldburg Dolerites. The Kulkatharra Dolerites display the following ranges of major oxide compositions (Table 2; Appendix 1) including significant variation of SiO_2 (44.47 – 54.58%) and K_2O (0.37 – 1.96%); in general, a narrow range of Na_2O (2.10 – 2.83%); moderate concentrations of CaO (average 8.95%); relatively low MgO (average 5.09%) and P_2O_5 (average 0.23%); and (as shown in Appendix 1) highly variable Mg# (27.54 – 63.12, average = 40.81). The Kulkatharra Dolerite is also distinguished by highly variable, on average, relatively low Cr contents (8–759 ppm, average = 85 ppm) and notably high and variable Cu (48–351 ppm, average 168 ppm) as shown in Table 2.

Kulkatharra Dolerite rocks are markedly enriched in REE (particularly heavy REE) and HFSE (principally Th and U). They also have relatively restricted ranges of REE as shown in Table 2; for example, La (14.09 – 31.90 ppm, average = 21.60 ppm), Yb (1.83 – 4.21 ppm, average = 2.85 ppm) and Nb (6.2 – 26.2 ppm, average = 11.5 ppm), and have smooth, negatively sloping, primitive mantle-normalized incompatible trace element profiles which indicate moderate fractionation in both light REE $(La/Sm)_N$ = 1.85 – 2.62); and heavy REE $(Gd/Yb)_N$ = 1.70 – 2.23) as shown in Appendix 1. The dolerites also have distinct negative Nb anomalies and an average Eu/Eu* = 0.92 (Fig. 10; Appendix 1). Figure 11 illustrates that the rocks have moderately elevated trace element ratios of Th/La (0.17 – 0.33, average = 0.22), Th/Nb (0.22 – 0.61, average = 0.46), and La/Sm (2.87 – 4.06, average = 3.47) compared to primitive mantle (Sun and McDonough, 1989). This suggests either low-to-moderate enrichment of the mantle source, or crustal contamination.

Bivariate diagrams (Fig. 12a,b) show a positive correlation between Al_2O_3, CaO, Cr, Ni, Sc/V, and Mg#, whereas $Fe_2O_3^T$, TiO_2, and P_2O_5 display strong negative correlations. The increase of $Fe_2O_3^T$ and decrease of Al_2O_3 with decreasing Mg# may indicate olivine + plagioclase fractionation. Figure 12a and b shows that the positive correlation between Ni and Mg# suggests that fractionation was initially controlled by olivine, then by pyroxene and plagioclase (positive correlations between CaO, Cr, Sc/V, and Mg#). Moderate to strong positive correlations between Sc/V and Mg# (Fig. 12b), coupled with a relatively wide range in Cr concentrations (Table 2) suggest the fractional crystallization of clinopyroxene (Wang et al., 2014). A negative correlation between P_2O_5 and Mg# may

indicate that apatite was not a major fractionating phase. The AFM diagram (Fig. 7) also shows a tholeiitic trend, implying that fractionation was controlled by early olivine and clinopyroxene fractionation (decreasing MgO) and that magnetite (or titanomagnetite) was fractionated late (increasing FeO). The geochemistry trends are in good agreement with petrographic observations and consistent with fractionation as a major control on geochemical composition.

Isotope analyses

The Kulkatharra Dolerite has relatively high $^{143}Nd/^{144}Nd_{(i)}$ values, ranging from 0.511129 to 0.511414, with a moderate range of $\varepsilon_{Nd(i)}$ values between 3.07 and –2.51 (Fig. 14; Appendix 4). Two-stage depleted-mantle Nd model ages (T_{DM}^{2}) range between 1.81 and 1.38 Ga, with a median of 1.71 Ga (Fig. 3).

Zircon and baddeleyite Lu–Hf analyses were conducted on three dolerite sill samples (Appendix 5). For GSWA 156750, 18 analyses of 15 zircons yielded initial $^{176}Hf/^{177}Hf$ compositions from 0.281949 to 0.282426, which correspond to a significant range of $\varepsilon_{Hf(i)}$ values between 10.9 and –4.9 (average = 4.3) and depleted-mantle model ages (T_{DM}) between 1.81 and 1.14 Ga (Fig. 15a,b; Appendix 5). For sample GSWA 169011, five analyses were made of five xenocrysts dated at 2946–1994 Ma (Fig.15a), four analyses of three c. 1070 Ma zircons, and three analyses of three baddeleyite grains. The xenocrystic zircons yielded initial $^{176}Hf/^{177}Hf$ compositions between 0.280717 and 0.281352, corresponding to $\varepsilon_{Hf(i)}$ values between 7.4 and –8.8 (average = –4.1) and depleted-mantle model ages (T_{DM}) between 3.45 and 2.60 Ga (Fig. 15b), attesting to the presence of highly evolved, old crustal material in this sample. Three c. 1070 Ma zircons yielded a narrow range of initial $^{176}Hf/^{177}Hf$ compositions from 0.282143 to 0.282302 (Fig. 15b), which correspond to $\varepsilon_{Hf(i)}$ values between 7.4 and 1.3 (average = 3.6) and depleted-mantle model ages between 1.58 and 1.33 Ga. Baddeleyite from the same sample yielded an equally narrow range of initial $^{176}Hf/^{177}Hf$ compositions between 0.282092 and 0.282220, corresponding to a range of $\varepsilon_{Hf(i)}$ values between 4.0 and 0.2 (average = 2.5) and model ages between 1.61 and 1.43 Ga (Fig. 15b; Appendix 5). Twelve zircons in GSWA 156602 yielded initial $^{176}Hf/^{177}Hf$ compositions between 0.282259 and 0.282466, corresponding to $\varepsilon_{Hf(i)}$ values between 12.9 and 5.7 (average = 9.2) and depleted-mantle model ages between 1.43 and 1.09 Ga (Fig. 15b; Appendix 5). The Kulkatharra Dolerite can be modelled as originating from sources extracted from the mantle at c. 3.0, 1.96, and 1.08 Ga (Fig. 15b).

The Hf isotope compositions in zircon and baddeleyite from all three samples are significantly more radiogenic than CHUR, with several grains having compositions close to the depleted-mantle model (Fig. 15a,b). This, combined with the presence of magmatic zircon and baddeleyite with slightly more evolved isotopic compositions, indicates that these mafic rocks were most likely derived from a radiogenic source similar to depleted mantle but which interacted with minor amounts of evolved (or old) crustal material, as is also suggested by the presence of xenocrystic zircons in GSWA 169011 (Appendix 5). These mafic rocks are, in general, more radiogenic than the Waldburg and Narimbunna Dolerites. However, geochemical proxies for crustal contamination, such as positive or negative correlations between $\varepsilon_{Nd(i)}$ and SiO_2, $(La/Sm)_{CN}$, Mg# or Nb/La (Fig. 13), suggest only minor contamination by crustal material.

Summary

The Kulkatharra Dolerite consists of slightly weathered, fine-grained to very coarse-grained, equigranular to subophitic quartz dolerite with irregular granophyric segregations and local pegmatitic leucogabbro veins and patches. Plagioclase and pyroxene are the primary mineral phases and are incipiently to moderately replaced by low-to-medium metamorphic grade alteration minerals; typically chlorite, sericite, saussurite, carbonate, prehnite, minor biotite and epidote. Crystallization ages for five dated sills range from c. 1083 to 1067 Ma, with samples of four sills yielding a mean age of 1075 ± 3 Ma. Two samples of one sill yielded a significantly older age of 1083 ± 4 Ma and may represent a separate episode of dolerite intrusion. Kulkatharra Dolerite samples are distinguished by relatively low MgO (average = 5.09%) and Cr (average = 85 ppm) contents, and high and variable Cu (average = 168 ppm). They are enriched in most REE (particularly heavy REE) and HFSE. The samples display light REE-enriched profiles with high $(La/Sm)_N$ ratios (average = 2.24), together with relatively high $(Gd/Yb)_N$ ratios (average = 1.89). The dolerite has moderate La/Nb ratios (average = 1.97) and displays a slight negative Nb anomaly. The chemical characteristics suggest either low-to-moderate enrichment of the mantle source or crustal contamination. Sm–Nd and Lu–Hf isotope compositions indicate that the Kulkatharra Dolerite was most likely derived from a radiogenic source similar to depleted mantle, but which interacted with relatively minor amounts of evolved (or old) crust, as suggested by geochemical proxies.

Intrusive events

Geochronology of the Waldburg, Narimbunna and Kulkatharra Dolerites provides reliable crystallization ages, although in each case there is an outlying result that is significantly different (Fig. 3; Table 1). Three Waldburg Dolerite samples yielded a mean age of 1514 ±3 Ma, and a fourth sample, at 1505 ± 3 Ma, is 9.3 ± 3.3 Ma (1σ) younger. Four samples of Narimbunna Dolerite provided a mean age of 1450 ± 3 Ma, whereas a fifth sample, which yielded an age of 1465 ± 3 Ma, is 14.8 ± 3.0 Ma (1σ) older. Two identical but independently dated Kulkatharra Dolerite samples yielded an age of 1083 ± 4 Ma, which is 8.3 ± 2.1 Ma (1σ) older than the mean age of 1075 ± 3 Ma for the other three samples. The differences in age of 8 to 15 Ma are significant, implying that the outlying result in each case represents the age of a separate intrusive event.

The Narimbunna and Kulkatharra Dolerites each have an older outlier (Fig. 3; Table 1), and these outlying samples also exhibit minor isotopic and geochemical differences compared to the other samples from each suite. Zircons from the older (c. 1465 Ma) Narimbunna sill (GSWA 156751) indicate mainly negative $\varepsilon_{Hf(i)}$ values and depleted-mantle model ages of 2.10 – 1.88 Ga, compared to

more radiogenic zircons from the c. 1452 Ma sill (GSWA 143450) that yield mostly positive $\varepsilon_{Hf(i)}$ values and slightly older depleted-mantle model ages of 2.23 – 2.05 Ga (Appendix 5). In contrast, however, the $\varepsilon_{Nd(i)}$ values for all Narimbunna sills are negative, and the younger (c. 1452 Ma) sills yield younger Nd model ages (2.08 Ga) compared to the c. 1465 Ma sills (2.28 – 2.14 Ga). No significant petrographic or geochemical differences are apparent between the 1465 and 1452 Ma sills. For the Kulkatharra Dolerite, the older (c. 1084 Ma) sill shows slightly different geochemical characteristics to the c. 1075 Ma sills, such as higher Nb/Y, Sm/Nd and V/Zr ratios, and lower La/Nb, La/Sm, Th/Nb, Th/La, Zr/Y and Ce/Y values (Appendix 1).

Nevertheless, there is insufficient information to conclude with confidence that the sills represented by the outlying samples are significantly different petrographically, geochemically or isotopically from other sills in each suite. It may be that each sill suite was emplaced episodically, perhaps triggered by intermittent changes in the regional or local stress regime, allowing sills in each suite to be emplaced at slightly different times but originating as pulses from the same magma source at deeper levels of the crust.

In this regard, it is worth noting a major difference between the Kulkatharra Dolerite and the two older sill suites. The Kulkatharra Dolerite is a component of the c. 1075 Ma Warakurna LIP, which extended mainly as sills and dykes over at least 2×10^6 km^2 in central and western Australia (Wingate et al., 2004; Wingate, 2017). The mafic magma that fed the Kulkatharra Dolerite, as well as dykes and sills in adjacent regions, may have originated well outside the Edmund and Collier Basins, injected laterally in the crust for distances of up to 1200 Ma (or more) from a source likely in central Australia (Wingate et al., 2004; Smithies et al., 2015; Wingate, 2017). In contrast, the Waldburg and Narimbunna Dolerites are not known to occur outside the Edmund Basin and, presumably, tapped more proximal magma sources.

Petrogenesis

The Waldburg, Narimbunna and Kulkatharra Dolerites define distinct groups or trends on various major elements, trace elements, and REE binary plots, although there is some overlap between them (Figs 10–12a,b; Appendix 4). In particular, each of the different mafic units can be characterized by variations between La/Sm, Th/Nb and Mg# (Fig. 11); SiO_2, Nb/La, Mg#, $(La/Sm)_{CN}$ and $\varepsilon_{Nd(i)}$ (Fig. 13); and Th/La vs La/Sm; Nb/Y vs Zr/P_2O_5; $(Gd/Yb)_{CN}$ vs $(La/Sm)_{CN}$; Ce/Y vs La/Nb; Zr vs Th/Tb; and Zr vs Zr/V (Appendix 3a,b), all of which relate to the source and depth of melting, fractionation history and degree of crustal contamination.

Melt source and depth of melting can be estimated from TiO_2/Yb, Th/Yb, and Nb/Yb contents (Pearce, 2008). All analysed mafic sills in the orogen have a relatively narrow range of compositions intermediate to OIB and N-MORB, generally equivalent to those of E-MORB (Figs 19, 20), indicating derivation from a similar mantle source. However, the wider range of Nb/Yb ratios of the Narimbunna Dolerite may indicate that it was derived from a similar but slightly heterogeneous source (Fig. 19). The TiO_2/Yb compositions for all the dolerites are transitional to the MORB–OIB array (Fig. 20), suggesting that all were derived from relatively shallow-mantle melting depths. Specifically, the Waldburg Dolerite generally has slightly higher TiO_2/Yb ratios than the younger Narimbunna Dolerite, suggesting that the Narimbunna magmas were sourced from shallower portions of the mantle (Fig. 20). The Kulkatharra Dolerite has a range of TiO_2/Yb contents that are equivalent to the range displayed by the Waldburg and Narimbunna Dolerites combined (Fig. 19).

The REE data (Fig. 10) for all samples in this study show relatively flat heavy REE patterns, and $(Gd/Yb)_N$ between 1.39 and 2.23 (Appendix 1), which may reflect melting at a shallower depth. This suggests the magmas for all three dolerites were sourced from garnet-free peridotite; i.e. in the spinel facies, where garnet is not a residual phase (Schmitz et al., 2004). The Kulkatharra Dolerite probably had a greater retention of garnet in the mantle source relative to the Waldburg and Narimbunna Dolerite, as indicated by higher $(Gd/Yb)_{CN}$ values (Rollinson, 1993; Morris and Pirajno, 2005).

The Nb/Yb and Th/Yb ratios in mafic rocks can be used as a proxy for melt source and to assess the role of crustal contamination (Pearce, 2008). All mafic samples in this study plot above the MORB–OIB array, consistent with high Th and low Nb contents (i.e. negative Nb anomalies). This geochemical feature is characteristic of rocks formed in subduction zones but, in this instance — where all the mafic rocks were formed in a within-plate setting — it suggests derivation from a mantle source previously modified by subduction processes (Pearce, 2008). In terms of Nb/Yb, the three dolerite units also have compositions intermediate to OIB and N-MORB, and a narrow range of compositions that parallel the MORB–OIB array, suggesting they were derived from a mildly heterogeneous, enriched-mantle source; possibly subduction-modified subcontinental lithospheric mantle.

The Waldburg Dolerite shows the least variation in Th/Yb (Fig. 19), indicating that the mafic magmas did not interact significantly with evolved crust during their transport or emplacement history. This is consistent with their narrow range of radiogenic zircon Hf (Fig. 15a), positive whole-rock Nd isotope compositions (Appendix 4), and trace element compositions (Fig. 10; Appendix 3). The Waldburg Dolerite samples show a very narrow trend parallel to the MORB–OIB array (Fig. 19), which may indicate derivation from a mildly heterogeneous mantle source.

Narimbunna Dolerite samples have a moderate range of Th/Yb ratios, the lowest of which overlap those of the Waldburg Dolerite (Fig. 19). These mafic rocks also have the most evolved zircon Hf (Fig. 15a,b) and negative whole-rock Nd isotope compositions (Appendix 4; Fig. 14), the most radiogenic of which are equivalent to the most evolved samples of the Waldburg Dolerite. Positive correlations between some major and trace elements, such as K_2O, Rb, Ba, and Zr (Appendix 2) and relatively strong Nb anomalies, are indicative of crustal contamination. Trace element ratios, such as TiO_2/Yb, average 0.66 and isotope compositions, for example, $\varepsilon_{Hf(i)}$ average –2.4, which suggest that the Narimbunna Dolerite may have a similar, but possibly slightly shallower, source than the Waldburg Dolerite. However, it is likely that the

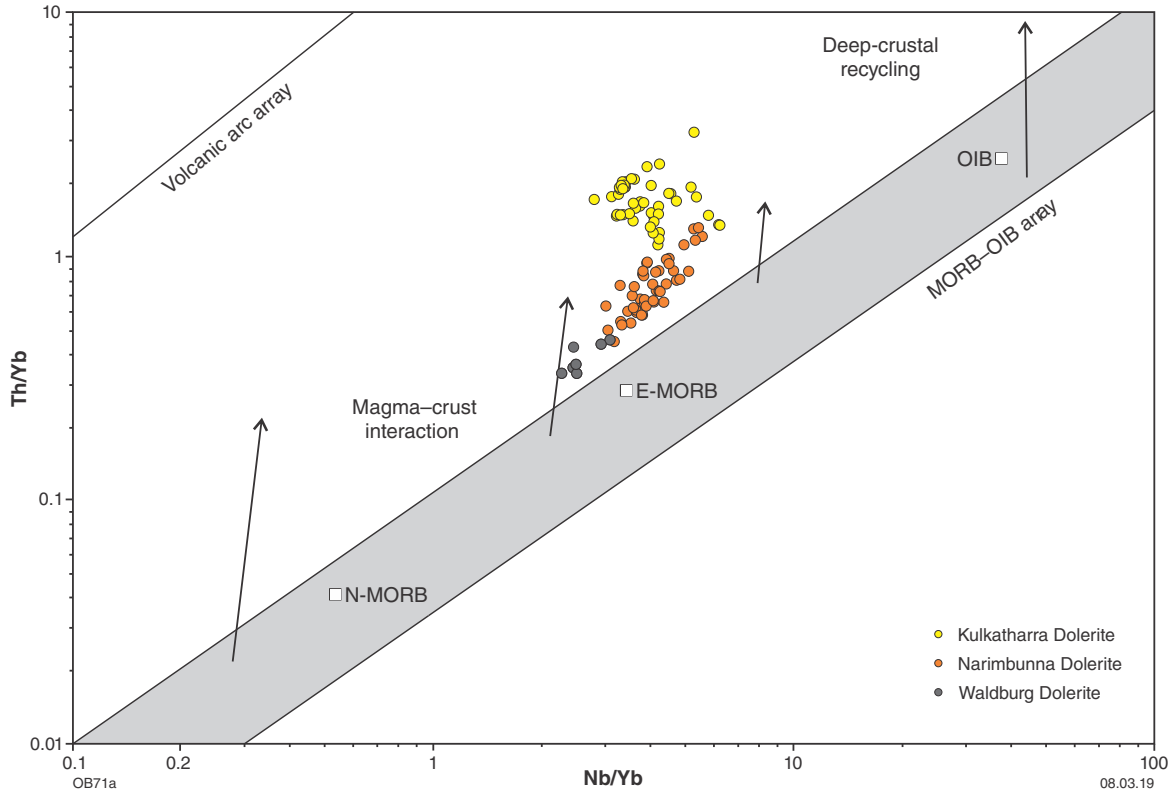

Figure 19. Discrimination diagram (Th/Yb vs Nb/Yb, Pearce, 2008) to separate subduction-related basalts from subduction-unrelated basalts. Dolerite samples are plotted relative to the MORB–OIB (ocean basalt) array, whereas the Th/Nb ratio is a crustal input proxy indicating a subduction, magma–crust interaction, or crustal recycling environment. Abbreviations: E-MORB, enriched mid-ocean ridge basalt; N-MORB, normal mid-ocean ridge basalt; OIB, ocean island basalt

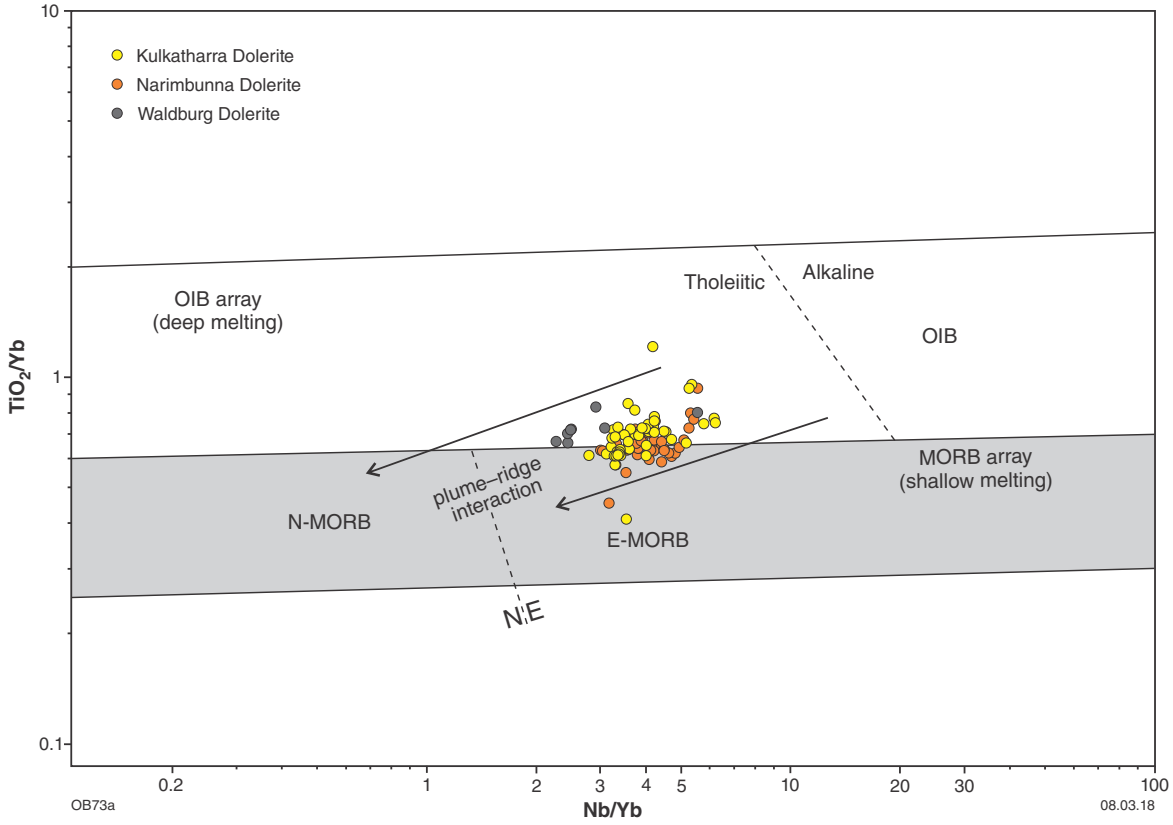

Figure 20. Discrimination diagram (TiO_2/Yb vs Nb/Yb) showing dolerite samples relative to MORB and OIB fields. The diagram reflects melting depth (hence mantle temperature and lithospheric thickness). Abbreviations: E-MORB, enriched mid-ocean ridge basalt; N-MORB, normal mid-ocean ridge basalt; OIB, ocean island basalt (Pearce, 2008)

Narimbunna Dolerite chemistry has been modified by interaction with evolved crustal material during transport or emplacement. The Narimbunna samples also trend parallel to the MORB–OIB array, continuing the Waldburg Dolerite trend. Hence, mafic rocks of the Waldburg and Narimbunna Dolerite were likely sourced from slightly different depths within a mildly heterogeneous subduction-modified lithospheric mantle.

The Kulkatharra Dolerite has both the highest values and largest range in Th/Yb ratios (Fig. 19; Appendix 1), suggesting that the composition of these rocks has been significantly modified by crustal material. The dolerite also has some $\varepsilon_{Nd(i)}$ trends that show progressive contamination; for example, decreasing $\varepsilon_{Nd(i)}$ with increasing SiO_2 and decreasing Nb/La (Fig. 13). The mafic rocks have highly variable, generally negative $\varepsilon_{Nd(i)}$ compositions between 3.07 and –2.51, accompanied by the most radiogenic $^{143}Nd/^{144}Nd_{(i)}$ ratios between 0.511129 and 0.511273 (Appendix 4) compared to the Waldburg and Narimbunna Dolerites. These rocks also have variable zircon $\varepsilon_{Hf(i)}$ compositions (Appendix 5) and the most radiogenic zircon Hf compositions (some similar to the depleted-mantle model, Fig. 15a). Figure 19 indicates that the Kulkatharra Dolerite has the highest and most dispersed Th/Yb ratios, as well as the largest deviation from the MORB–OIB array, which implies that these rocks are more contaminated by crustal material.

However, there appears to be a decoupling between major element chemistry and isotope composition in these rocks. The Sm–Nd isotope data (Appendix 4) suggest that the Kulkatharra Dolerite is the least crustally contaminated of the dolerite suites, whereas in trace element plots Th/Yb vs Nb/Yb and TiO_2/Yb vs Nb/Yb (Figs 19, 20) the Kulkatharra Dolerite is the most evolved. This raises the question: does the Th/Yb ratio represent melt generated from the most subduction-modified mantle rather than being a proxy for crustal contamination? If this is the case, the primary control on the Th/Yb content in these mafic rocks might have been the composition of the source region rather than alteration or incorporation of evolved crustal material. This in turn suggests that the rocks were most likely derived from a radiogenic source similar to depleted mantle, with only minor interaction with crustal material.

Both the 1514–1505 Ma Waldburg and the 1465–1450 Ma Narimbunna Dolerite were generated and emplaced during periods of orogenic quiescence. It is proposed here that these two events were related to minor intracontinental rifting. In contrast, and as noted above, the 1083–1075 Ma Kulkatharra Dolerite is part of the Warakurna LIP, itself associated with the 1085–1040 Ma Giles Event in the Musgrave Province of central Australia (Howard et al., 2011, 2015, 2016; Smithies et al., 2015).

The early history of the Capricorn Orogen records the assembly of the West Australian Craton through subduction-collision/accretion processes during the 2215–2145 Ma Ophthalmia and 2005–1950 Ma Glenburgh Orogenies (e.g. Sheppard, 2004; Cawood and Tyler, 2004; Sheppard et al., 2005, 2007, 2010; Rasmussen et al., 2005; Johnson et al., 2010, 2011a,b, 2017). These events would have most likely resulted in the metasomatization and subduction-modification of the subcontinental lithospheric mantle (Johnson et al., 2017) beneath the orogen. The compositions of the Waldburg and Narimbunna Dolerites suggest derivation from this mildly heterogeneous subduction-modified lithospheric mantle at shallow depths.

Conclusion

Mafic sills within the Capricorn Orogen were previously divided into two distinct suites, the c. 1465 Ma Narimbunna and c. 1070 Ma Kulkatharra Dolerite. Based on new field mapping, geochronology, whole-rock geochemistry and isotopic data; a third suite, the Waldburg Dolerite, has been identified. The discovery of this new magmatic event contributes to a better understanding of dynamic processes and the complex geological history of the Capricorn Orogen.

This new assessment of previous and new geochronology better defines the ages of the c. 1514 Ma Waldburg, c.1450 Ma Narimbunna and c. 1075 Ma Kulkatharra Dolerites. However, the results for each dolerite suite include a significantly older or younger outlier, at 1505, 1465 and 1083 Ma, respectively (Fig. 3; Table 1). Although the differences in age of 8–15 Ma are significant, the absence of obvious petrographic, geochemical or isotopic differences between each outlying sample and others in that suite suggest that each sill suite originated from the same magma source and that the range of ages reflects episodic or intermittent changes in the regional or local stress regime.

The Waldburg, Narimbunna and Kulkatharra Dolerites are high-Fe tholeiites and were sourced from slightly different depths within a mildly heterogeneous subduction-modified lithospheric mantle. Major differences between suites in petrography, whole-rock geochemistry and isotope compositions probably reflect varying degrees of interaction with evolved crustal material and by fractionation during melt transport and emplacement.

The Waldburg Dolerite has limited exposure and intrudes only the lower to middle parts of the Edmund Group, within the western Capricorn Orogen. Waldburg sills were emplaced in a structural corridor between two major faults: the Lyons River Fault and the Ti Tree Shear Zone. The Waldburg Dolerite can be distinguished geochemically and isotopically from the Narimbunna and Kulkatharra Dolerites. Insignificant Nb anomalies, minor REE (particularly heavy REE) fractionation and uniformly positive $\varepsilon_{Nd(i)}$ values indicate that the Waldburg Dolerite is the most primitive in composition compared with the other dolerites in the region and did not have significant interaction with evolved crustal material during its transport and emplacement history.

References

Blay, OA, Johnson, SP and Thorne, AM 2015a, Narimbunna Dolerite (P_-_nr-od): Geological Survey of Western Australia, WA Geology Online, Explanatory Notes extract, viewed 23 November 2017, <www.dmp.wa.gov.au/ens>.

Blay, OA, Johnson, SP, Thorne, AM and Cutten, HNC 2016, Waldburg Dolerite (P_-_wa-od): Geological Survey of Western Australia, WA Geology Online, Explanatory Notes extract, viewed 23 November 2017, <www.dmp.wa.gov.au/ens>.

Blay, OA, Johnson, SP, Wingate, MTD and Thorne, AM 2015b, Kulkatharra Dolerite (P_-WKku-od): Geological Survey of Western Australia, WA Geology Online, Explanatory Notes extract, viewed 23 November 2017, <www.dmp.wa.gov.au/ens>.

Blichert-Toft, J and Albarède, F 1997, The Lu–Hf isotope geochemistry of chondrites and the evolution of the mantle–crust system: Earth and Planetary Science Letters, v. 148, p. 243–258.

Blundy, I and Wood, B 2003, Partitioning of trace elements between crystals and melts: Earth and Planetary Science Letters, v. 210, p. 383–397.

Cann, JR 1970, Rb, Sr, Y, Zr, and Nb in some ocean floor basaltic rocks: Earth and Planetary Science Letters, v. 10, no. 1, p. 7–11.

Cawood, PA and Tyler, IM 2004, Assembling and reactivating the Proterozoic Capricorn Orogen: lithotectonic elements, orogenies, and significance: Precambrian Research, v. 128, p. 201–218.

Champion, DC 2013, Neodymium depleted mantle model age map of Australia: explanatory notes and user guide. Record 2013/44: Geoscience Australia, Canberra.

Champion, DC and Cassidy, KF 2008, Geodynamics: Using geochemistry and isotopic signatures of granites to aid mineral systems studies: an example from the Yilgarn Craton, *in* New perspectives: The foundations and future of Australian exploration. Abstracts for the June 2008 pmd*CRC Conference Record 2008/09, 7–16 *edited by* RJ Korsch and AC Barnicoat: Geoscience Australia, Canberra, 2008, p. 7–16.

Cutten, HN, Johnson, SP, Thorne, AM, Wingate, MTD, Kirkland, CL, Belousova, EA, Blay, OA and Zwingmann, H 2016, Deposition, provenance, inversion history and mineralization of the Proterozoic Edmund and Collier Basins, Capricorn Orogen: Geological Survey of Western Australia, Report 127, 74p.

Daniels, JL (compiler) 1969, Edmund, Western Australia: Geological Survey of Western Australia, 1:250 000 Geological Series Explanatory Notes, 18p.

Ernst, RE and Buchan, KL (editors) 2001, Mantle plumes: their identification through time: Geological Society of America, Special Paper 352, 593p.

Farmer, GL 2005, Continental Basaltic Rocks, *in* Treatise on Geochemistry, Volume 3, The Crust, 2005 *edited by* RL Rudnick, Elsevier, Amsterdam, p. 85–121.

Gelinas, L, Mellinger, M and Trudel, P 1982, Archean mafic metavolcanics from the Rouyn–Noranda district, Abitibi Greenstone Belt, Quebec. 1, Mobility of the major elements: Canadian Journal of Earth Sciences, v. 19, p. 2258–2275.

GeoChemExtract 2017, Geochemistry database, Geological Survey of Western Australia.

Glikson, AY, Stewart, AJ, Ballhaus, CG, Clarke, GL, Feeken, EHJ, Leven, JH, Sheraton, JW and Sun, S-S 1996, Geology of the western Musgrave Block, central Australia, with particular reference to the mafic–ultramafic Giles Complex: Australian Geological Survey Organisation, Bulletin 239, 206p.

Goldstein, SL, O'Nions, RK and Hamilton, PJ 1984, A Sm–Nd isotopic study of atmospheric dusts and particulates from major river systems: Earth and Planetary Science Letters, no. 70, p. 221–236.

Griffin, WL, Belousova, EA, Shee, SR, Pearson, NJ and O'Reilly, SY 2004, Archean crustal evolution in the northern Yilgarn Craton: U–Pb and Hf-isotope evidence from detrital zircons: Precambrian Research, v. 131, p. 231–282.

Griffin, WL, Pearson, NJ, Belousova, EA, Jackson, SE, O'Reilly, SY, van Achterbergh, E and Shee, SR 2000, The Hf isotope composition of cratonic mantle: LAM-MC-ICPMS analysis of zircon megacrysts in kimberlites: Geochimica et Cosmochimica Acta, v. 64, p. 133–147.

Haines, PW, Kirkland, CL, Wingate, MTD, Allen, H, Belousova, EA and Gréau, Y 2016, Tracking sediment dispersal during orogenesis: a zircon age and Hf isotope study from the western Amadeus Basin, Australia: Gondwana Research, v. 37, p. 324–347, doi:10.1016/j.gr.2015.08.011.

Hancock, EA, Green, AA, Huntington, JF, Schodlok, MC and Whitbourn, LB 2013, HyLogger-3: Implications of adding thermal-infrared sensing: Geological Survey of Western Australia, Record 2013/3, 24p.

Hanski, E, Mertanen, S, Rämö, T and Vuollo, J (editors) 2006, Dyke swarms — time markers of crustal evolution: CRC Press, Taylor & Francis Group, London, UK, 273p.

Howard, HM, Smithies, RH, Evins, PM, Kirkland, CL, Werner, M and Wingate, MTD 2016, Warakurna Supersuite (P_-WK-xo-f): Geological Survey of Western Australia, WA Geology Online, Explanatory Notes extract, viewed 29 March 2017, <www.dmp.wa.gov.au/ens>.

Howard, HM, Smithies, RH, Evins, PM and Werner, M 2011, Geological interpretation of the west Musgrave Province — Wingellina to Jameson (1:250 000) *in* The geology of the west Musgrave Province and the Bentley Supergroup — a field guide *by* HM Howard, M Werner, RH Smithies, PM Evins, CL Kirkland, DE Kelsey, M Hand, AS Collins, F Pirajno, MTD Wingate, WD Maier and T Raimondo: Geological Survey of Western Australia, Record 2011/4, Plate 1.

Howard, HM, Smithies, RH, Kirkland, CL, Kelsey, DE, Aitken, A, Wingate, MTD, Quentin de Gromard, R, Spaggiari, CV and Maier, WD 2015, The burning heart — the Proterozoic geology and geological evolution of the west Musgrave Region, central Australia: Gondwana Research, v. 27, no. 1, p. 64–94.

Howard, HM, Smithies, RH and Pirajno, F 2007, Geochemical and Nd isotopic signatures of mafic dykes in the western Musgrave Complex, *in* Geological Survey of Western Australia Annual Review 2005–06: Geological Survey of Western Australia, p. 64–71.

Hynes, A 1980, Carbonatization and mobility of Ti, Y, and Zr in Ascot Formation metabasalts, SE Quebec: Contributions to Mineralogy and Petrology, v. 75, p. 79–87.

Irvine, TN and Baragar, WRA 1971, A guide to the chemical classification of the common volcanic rocks: Canadian Journal of Earth Sciences, v. 8, p. 523–548.

Jensen, LS 1976, A new cation plot for classifying subalkalic volcanic rocks: Ontario Geological Survey, Miscellaneous paper 66.

Johnson, SP, Cutten, HN, Tyler, IM, Korsch, RJ, Thorne, AM, Blay, OA, Kennett, BLN, Blewett, RS, Joly, A, Dentith, MC, Aitken, ARA, Goodwin, JA, Salmon, M, Reading, A, Boren, G, Ross, J, Costelloe, RD and Fomin, T 2011a, Preliminary interpretation of deep seismic reflection lines 10GA–CP2 and 10GA–CP3: crustal architecture of the Gascoyne Province, and Edmund and Collier Basins, *in* Capricorn Orogen seismic and magnetotelluric (MT) workshop 2011: extended abstracts *edited by* SP Johnson, AM Thorne and IM Tyler: Geological Survey of Western Australia, Record 2011/25, p. 49–60.

Johnson, SP, Korhonen, FJ, Kirkland, CL, Cliff, JB, Belousova, EA and Sheppard, S 2017, From subduction magmatism to cratonization: an isotopic perspective from the Capricorn Orogen, *in* GSWA 2017 Extended abstracts: promoting the prospectivity of Western Australia: Geological Survey of Western Australia, Record 2017/2, p. 9–13.

Johnson, SP, Sheppard, S, Rasmussen, B, Wingate, MTD, Kirkland, CL, Muhling, JR, Fletcher, IR and Belousova, E 2010, The Glenburgh Orogeny as a record of Paleoproterozoic continent–continent collision: Geological Survey of Western Australia, Record 2010/5, 54p.

Johnson, SP, Sheppard, S, Rasmussen, B, Wingate, MTD, Kirkland, CL, Muhling, JR, Fletcher, IR and Belousova, EA 2011b, Two collisions, two sutures: punctuated pre-1950 Ma assembly of the West Australian Craton during the Ophthalmian and Glenburgh Orogenies: Precambrian Research, v. 189, no. 3–4, p. 239–262, doi:10.1016/j.precamres.2011.07.011.

Johnson, SP, Sheppard, S, Thorne, AM, Rasmussen, B, Fletcher, IR, Wingate, MTD and Cutten, HN 2011c, The role of the 1280–1250 Ma Mutherbukin Tectonic Event in shaping the crustal architecture and mineralization history of the Capricorn Orogen, *in* GSWA 2011 extended abstracts: promoting the prospectivity of Western Australia: Geological Survey of Western Australia, Record 2011/2, p. 1–3.

Johnson, SP, Thorne, AM, Tyler, IM, Korsch, RJ, Kennett, BLN, Cutten, HN, Goodwin, J, Blay, OA, Blewett, RS, Joly, A, Dentith, MC, Aitken, ARA, Holzschuh, J, Salmon, M, Reading, A, Heinson, G, Boren, G, Ross, J, Costelloe, RD and Fomin, T 2013, Crustal architecture of the Capricorn Orogen, Western Australia and associated metallogeny: Australian Journal of Earth Sciences, v. 60, no. 6–7, p. 681–705, doi:10.1080/08120099.2013.826735.

Kirkland, CL, Spaggiari, CV, Pawley, MJ, Wingate, MTD, Smithies, RH, Howard, HM, Tyler, IM, Belousova, EA and Poujol, M 2011, On the edge: U–Pb, Lu–Hf, and Sm–Nd data suggests reworking of the Yilgarn Craton margin during formation of the Albany–Fraser Orogen: Precambrian Research, v. 187, p. 223–247.

Korhonen, FJ, Johnson, SP, Fletcher, IR, Rasmussen, B, Sheppard, S, Muhling, JR, Dunkley, DJ, Wingate, MTD, Roberts, MP and Kirkland, CL 2015, Pressure–temperature–time evolution of the Mutherbukin Tectonic Event, Capricorn Orogen: Geological Survey of Western Australia, Report 146, 64p.

Korhonen, FJ, Johnson, SP, Wingate, MTD, Kirkland, CL, Fletcher, IR, Dunkley, DJ, Roberts, MP, Sheppard, S, Muhling, JR and Rasmussen, B 2017, Radiogenic heating and craton–margin plate stresses as drivers for intraplate orogeny: Journal of Metamorphic Geology, v. 35, no. 6, p. 631–661, doi:10.1111/jmg.12249.

Li, X-H, Li, Z-X, Wingate, MTD, Chung, S-L, Liu, Y, Lin, G-C and Li, W-X 2006, Geochemistry of the 755 Ma Mundine Well dyke swarm, northwestern Australia: part of a Neoproterozoic mantle superplume beneath Rodinia?: Precambrian Research, v. 146, no. 1–2, p. 1–15, doi:10.1016/j.precamres.2005.12.007.

Ludden, J, Gelinas, L and Trudel, P 1982, Archaean metavolcanics from the Rouyn–Noranda district, Abitibi greenstone belt, Quebec. 2. Mobility of trace elements and petrogenetic constraints: Canadian Journal of Earth Sciences, v. 19, p. 2276–2287.

Maier, WD, Howard, HM, Smithies, RH, Yang, S, Barnes, S-J, O'Brien, H, Huhma, H and Gardoll, S 2014, Mafic–ultramafic intrusions of the Giles Event, Western Australia: petrogenesis and prospectivity for magmatic ore deposits: Geological Survey of Western Australia, Report 134, 82p.

Martin, DMcB 2003, Peperite in the Backdoor Formation and its significance to the age and tectonic evolution of the Bangemall Supergroup, *in* Geological Survey of Western Australia Annual Review 2002–03: Geological Survey of Western Australia, p. 53–59.

Martin, DMcB, Sheppard, S and Thorne, AM 2005, Geology of the Maroonah, Ullawarra, Capricorn, Mangaroon, Edmund, and Elliott Creek 1:100 000 sheets: Geological Survey of Western Australia, 1:100 000 Geological Series Explanatory Notes, 65p.

Martin, DMcB, Sheppard, S, Thorne, AM, Farrell, TR and Groenewald, PB 2007, Proterozoic geology of the western Capricorn Orogen — a field guide: Geological Survey of Western Australia, Record 2006/18, 43p.

Martin, DMcB, Sircombe, KN, Thorne, AM, Cawood, PA and Nemchin, AA 2008, Provenance history of the Bangemall Supergroup and implications for the Mesoproterozoic paleogeography of the West Australian Craton, *in* Assembling Australia: Proterozoic building of a continent *edited by* PA Cawood and RJ Korsch: Precambrian Research v. 166, no. 1–4, p. 93–110.

Martin, DMcB and Thorne, AM 2004, Tectonic setting and basin evolution of the Bangemall Supergroup in the northwestern Capricorn Orogen: Precambrian Research, v. 128, no. 3–4, p. 385–409.

Mole, DR, Fiorentini, ML, Cassidy, KF, Kirkland, CL, Thebaud, N, McCuaig, TC, Doublier, MP, Duuring, P, Romano, SS, Maas, R, Belousova, EA, Barnes, SJ and Miller, J 2013, Crustal evolution, intra-cratonic architecture and the metallogeny of an Archaean craton: Geological Society, *in* Ore Deposits in an Evolving Earth *edited by* GRT Jenkin, PAJ Lusty, I Mcdonald, MP Smith, AJ Boyce and JJ Wilkinson: Geological Society, London, Special Publications, v. 393, p. 23–80, doi:10.1144/SP393.8.

Morris, PA 2000, Composition of Geological Survey of Western Australia geochemical reference materials: Geological Survey of Western Australia, Record 2000/11, 33p.

Morris, PA and Pirajno, F 2005, Mesoproterozoic sill complexes in the Bangemall Supergroup, Western Australia: geology, geochemistry, and mineralization potential: Geological Survey of Western Australia, Report 99, 75p.

Morris, PA and Pirajno, F 2009, Chemical fingerprinting of the multiple large-scale magmatic events in the Mesoproterozoic Bangemall Supergroup, Western Australia: Australian Journal of Earth Sciences, v. 56, p. 985–1001.

Muhling, PC and Brakel, AT 1985, Geology of the Bangemall Group: the evolution of a Proterozoic intracratonic sedimentary basin: Geological Survey of Western Australia, Bulletin 128, 266p.

Nelson, DR 2001a, 156750: granophyric quartz dolerite, Curran Well; Geochronology Record 261: Geological Survey of Western Australia, 3p.

Nelson, DR 2001b, 156751: coarse dolerite, Coolinbah Well; Geochronology Record 242: Geological Survey of Western Australia, 4p.

Nelson, DR 2001c, 169011: quartz dolerite, Strama Gap; Geochronology Record 150: Geological Survey of Western Australia, 5p.

Nesbitt, RW, Walker, IW and Blight, DF 1984, Geochemistry of Archaean metabasaltic lavas, Diemals, Western Australia, *in* Professional papers for 1982: Geological Survey of Western Australia, Report 12, p. 15–26.

Payne, JL, McInerney, DJ, Barovich, KM, Kirkland, CL, Pearson, NJ and Hand, M 2016, Strengths and limitations of zircon Lu–Hf and O isotopes in modelling crustal growth: Lithos, v. 248–251, p. 175–192.

Pearce, JA 1975, Basalt geochemistry used to investigate past tectonic environments in Cyprus: Tectonophysics, v. 25, p. 41–67.

Pearce, JA 1996, A user's guide to basalt discrimination diagrams, *in* Trace element geochemistry of volcanic rocks: applications for massive sulphide exploration *edited by* DA Wyman: Geological Association of Canada, Short Course Notes, v. 12, p. 79–113.

Pearce, JA 2008, Geochemical fingerprinting of oceanic basalts with applications to ophiolite classification and the search for Archean oceanic crust: Lithos, v. 100, p. 14–48.

Pearce, JA and Cann, JR 1973, Tectonic setting of basic volcanic rocks determined using trace element analyses: Earth and Planetary Science Letters, v. 19, p. 290–300.

Peng, P and Ernst, R 2016, Dyke swarms: keys to paleogeographic reconstructions, preface for IDC7 2016, *in* Abstracts of the Seventh International Dyke Conference, 'Dyke Swarms': Keys to Paleogeographic Reconstruction: Acta Geologica Sinica, v. 90, supp. 1, Beijing, China, 18 August 2016, 447p.

Pirajno, F and Hoatson, DM 2012, A review of Australia's large igneous provinces and associated mineral systems: implications for mantle dynamics through geological time: Ore Geology Reviews, v. 48, p. 2–54.

Pirajno, F and Santosh, M 2015, Mantle plumes, supercontinents, intracontinental rifting and mineral systems: Precambrian Research, v. 259, p. 243–261, doi:10.1016/j.precamres.2014.12.016.

Rasmussen, B, Fletcher, IR and Sheppard, S 2005, Isotopic dating of the migration of a low-grade metamorphic front during orogenesis: Geology, v. 33, no. 10, p. 773–776.

Rollinson, HR 1993, Using geochemical data: evaluation, presentation, interpretation: Pearson Education Ltd, Harlow, England, 352p.

Scherer, EE, Münker, C, Mezger, K 2001, Calibration of the lutetium–hafnium clock: Science 293, p. 683–687.

Schmitz, MD, Vervoort, JD, Bowring, SA and Patchett, PJ 2004, Decoupling of the Lu–Hf and Sm–Nd isotope systems during the evolution of granulitic lower crust beneath southern Africa: Geology, v. 32, no. 5 p. 405–408.

Sheppard, S 2004, Unravelling the complexity of the Gascoyne Complex, *in* GSWA 2004 extended abstracts: promoting the prospectivity of Western Australia: Geological Survey of Western Australia, Record 2004/5, p. 26–28.

Sheppard, S, Bodorkos, S, Johnson, SP, Wingate, MTD and Kirkland, CL 2010, The Paleoproterozoic Capricorn Orogeny: intracontinental reworking not continent–continent collision: Geological Survey of Western Australia, Report 108, 33p.

Sheppard, S, Occhipinti, SA and Nelson, DR 2005, Intracontinental reworking in the Capricorn Orogen, Western Australia: the 1680–1620 Ma Mangaroon Orogeny: Australian Journal of Earth Sciences, v. 52, p. 443–460.

Sheppard, S, Rasmussen, B, Muhling, JR, Farrell, TR and Fletcher, IR 2007, Grenvillian-aged orogenesis in the Palaeoproterozoic Gascoyne Complex, Western Australia: 1030–950 Ma reworking of the Proterozoic Capricorn Orogen: Journal of Metamorphic Geology, v. 25, p. 477–494.

Smithies, RH, Kirkland, CL, Korhonen, FJ, Aitken, ARA, Howard, HM, Maier, WD, Wingate, MTD, Quentin de Gromard, R and Gessner, K 2015, The Mesoproterozoic thermal evolution of the Musgrave Province in central Australia — plume vs. the geological record: Gondwana Research, v. 27, p. 1419–1429.

Srivastava, RK (editor) 2011, Dyke swarms: keys for geodynamic interpretation: SpringerVerlag Science, Berlin, 605p.

Stern, RA 2001, A new isotopic and trace-element standard for the ion microprobe: preliminary thermal ionization mass spectrometry (TIMS) U–Pb and electron microprobe data: Geological Survey of Canada, Report 2001-F1, 11p.

Stracke, A, Zindler, A, Salters, V, McKenzie, D, Blichert-Toft, J, Albarède, F and Gronvold, K 2003, Theistareykir revisited: Geochemistry, Geophysics, Geosystems, v. 4, no. 2, p. 1–49, doi:10.1029/2001GC000201.

Sun, S-S and McDonough, WF 1989, Chemical and isotopic systematics of oceanic basalts: implications for mantle composition and processes, *in* Magmatism in the Ocean Basins *edited by* AD Saunders and MJ Norry: Geological Society, London, Special Publication 42, p. 313–345.

Tarney, J 1992, Geochemistry and significance of mafic dyke swarms in the Proterozoic, *in* Proterozoic Crustal Evolution *edited by* KC Condie: Elsevier Science, Amsterdam, Developments in Precambrian Geology 10, p. 151–179.

Thorne, AM 2015a, Edmund Group, Depositional package 1 (P_-MEP1-kt): Geological Survey of Western Australia, WA Geology Online, Explanatory Notes extract, viewed 29 March 2017, <www.dmp.wa.gov.au/ens>.

Thorne, AM 2015b, Edmund Group, Depositional package 2 (P_-MEP2-sk): Geological Survey of Western Australia, WA Geology Online, Explanatory Notes extract, viewed 29 March 2017, <www.dmp.wa.gov.au/ens>.

Thorne, AM 2015c, Edmund Group, Depositional package 3 (P_-MEP3-sk): Geological Survey of Western Australia, WA Geology Online, Explanatory Notes extract, viewed 29 March 2017, <www.dmp.wa.gov.au/ens>.

Thorne, AM 2015d, Edmund Group, Depositional package 4 (P_-MEP4-xs-k): Geological Survey of Western Australia, WA Geology Online, Explanatory Notes extract, viewed 29 March 2017, <www.dmp.wa.gov.au/ens>.

Thorne, AM 2016a, Collier Group, Depositional package 5 (P_-MCP5-s): Geological Survey of Western Australia, WA Geology Online, Explanatory Notes extract, viewed 29 March 2017, <www.dmp.wa.gov.au/ens>.

Thorne, AM 2016b, Collier Group, Depositional package 6 (P_-MCP6-s): Geological Survey of Western Australia, WA Geology Online, Explanatory Notes extract, viewed 29 March 2017, <www.dmp.wa.gov.au/ens>.

Thorne, AM and Martin, DMcB 2007, Peedawarra, WA Sheet 2349: Geological Survey of Western Australia, 1:100 000 Geological Series.

Wang, X-C, Li, Z-X, Li, J, Pisarevsky, SA and Wingate, MTD 2014, Genesis of the 1.21 Ga Marnda Moorn large igneous province by plume–lithosphere interaction: Precambrian Research, v. 241, p. 85–103.

Wilson, M 1989, Igneous petrogenesis: a global tectonic approach: Chapman and Hall, London, England, 466p.

Winchester, JA and Floyd, PA 1976, Geochemical magma type discrimination: application to altered and metamorphosed basic igneous rocks: Earth and Planetary Science Letters, v. 28, no. 3, p. 459–469.

Wingate, MTD 2002, Age and palaeomagnetism of dolerite sills of the Bangemall Supergroup on the Edmund 1:250 000 sheet, Western Australia: Geological Survey of Western Australia, Record 2002/4, 48p.

Wingate, MTD 2003, Age and palaeomagnetism of dolerite intrusions of the southeastern Collier Basin and the Earaheedy and Yerrida Basins, Western Australia: Geological Survey of Western Australia, Record 2003/3, 34p.

Wingate, MTD 2017, Mafic dyke swarms and large igneous provinces in Western Australia get a digital makeover, *in* GSWA 2017 Extended abstracts: promoting the prospectivity of Western Australia: Geological Survey of Western Australia, Record 2017/2, p. 4–8.

Wingate, MTD and Bodorkos, S 2007, 156602: granophyric dolerite sill, No. 36 Well; Geochronology Record 695, *in* Compilation of geochronology data: Geological Survey of Western Australia, 5p.

Wingate, MTD, Lu, Y, Kirkland, CL, Blay, O and Johnson, SP 2017, 207259: dolerite sill, Maranoo Well; Geochronology Record 1434: Geological Survey of Western Australia, 4p.

Wingate, MTD, Kirkland, CL, Blay, OA and Johnson, SP 2013a, 207259: dolerite sill, Maranoo Well; Geochronology Record 1123: Geological Survey of Western Australia, 4p.

Wingate, MTD, Kirkland, CL, Blay, OA and Johnson, SP 2015a, 206916: metadolerite sill, Swamp Well; Geochronology Record 1262: Geological Survey of Western Australia, 4p.

Wingate, MTD, Kirkland, CL, Blay, OA and Johnson, SP 2015b, 206991: metadolerite sill, Gap Well; Geochronology Record 1263: Geological Survey of Western Australia, 4p.

Wingate, MTD, Kirkland, CL, Blay, OA and Johnson, SP 2015c, 206994: altered dolerite sill, Eden Bore; Geochronology Record 1264: Geological Survey of Western Australia, 4p.

Wingate, MTD, Kirkland, CL, Blay, OA and Johnson, SP 2015d, 206995: altered dolerite sill, Eden Bore; Geochronology Record 1265: Geological Survey of Western Australia, 4p.

Wingate, MTD, Kirkland, CL and Cutten, HN 2012a, 143440: felsic metavolcaniclastic rock, Nicken Bore; Geochronology Record 1029: Geological Survey of Western Australia, 6p.

Wingate, MTD, Kirkland, CL and Cutten, HN 2013b, 189223: dolerite sill, Mount Arapiles; Geochronology Record 1118: Geological Survey of Western Australia, 4p.

Wingate, MTD, Kirkland, CL and Cutten, HN 2014, 189224: dolerite sill, Sawback Range; Geochronology Record 1211: Geological Survey of Western Australia, 4p.

Wingate, MTD, Kirkland, CL, Cutten, HN and Thorne, AM 2012b, 143445: dolerite sill, Waldburg Homestead; Geochronology Record 1077: Geological Survey of Western Australia, 4p.

Wingate, MTD, Kirkland, CL, Cutten, HN and Thorne, AM 2012c, 143450: dolerite sill, Top Camp Well; Geochronology Record 1078: Geological Survey of Western Australia, 4p.

Wingate, MTD and Lu, Y 2017, Introduction to geochronology information released in 2017: Geological Survey of Western Australia, 5p.

Wingate, MTD, Pirajno, F and Morris, PA 2004, Warakurna large igneous province: a new Mesoproterozoic large igneous province in west-central Australia: Geology, v. 32, no. 2, p. 105–108.

Wyborn, LAI, Page, RW and McCulloch, MT 1988, Petrology, geochronology and isotope geochemistry of the post-1820 Ma granites of the Mount Isa Inlier: mechanisms for the generation of Proterozoic anorogenic granites: Precambrian Research, 40–41, 509–541.

Zhao, JX, McCulloch, MT and Korsch, RJ 1994, Characterisation of a plume-related ~800 Ma magmatic event and its implications for basin formation in central-southern Australia: Earth and Planetary Science Letters, v. 121, no. 3–4, p. 349–367, doi:10.1016/0012-821X(94)90077-9.

Appendices*

* Appendix 1 can be found on the accompanying ZIP file

Appendix 2

Bivariate plots of LOI and Zr vs LILE as a proxy of trace element mobility

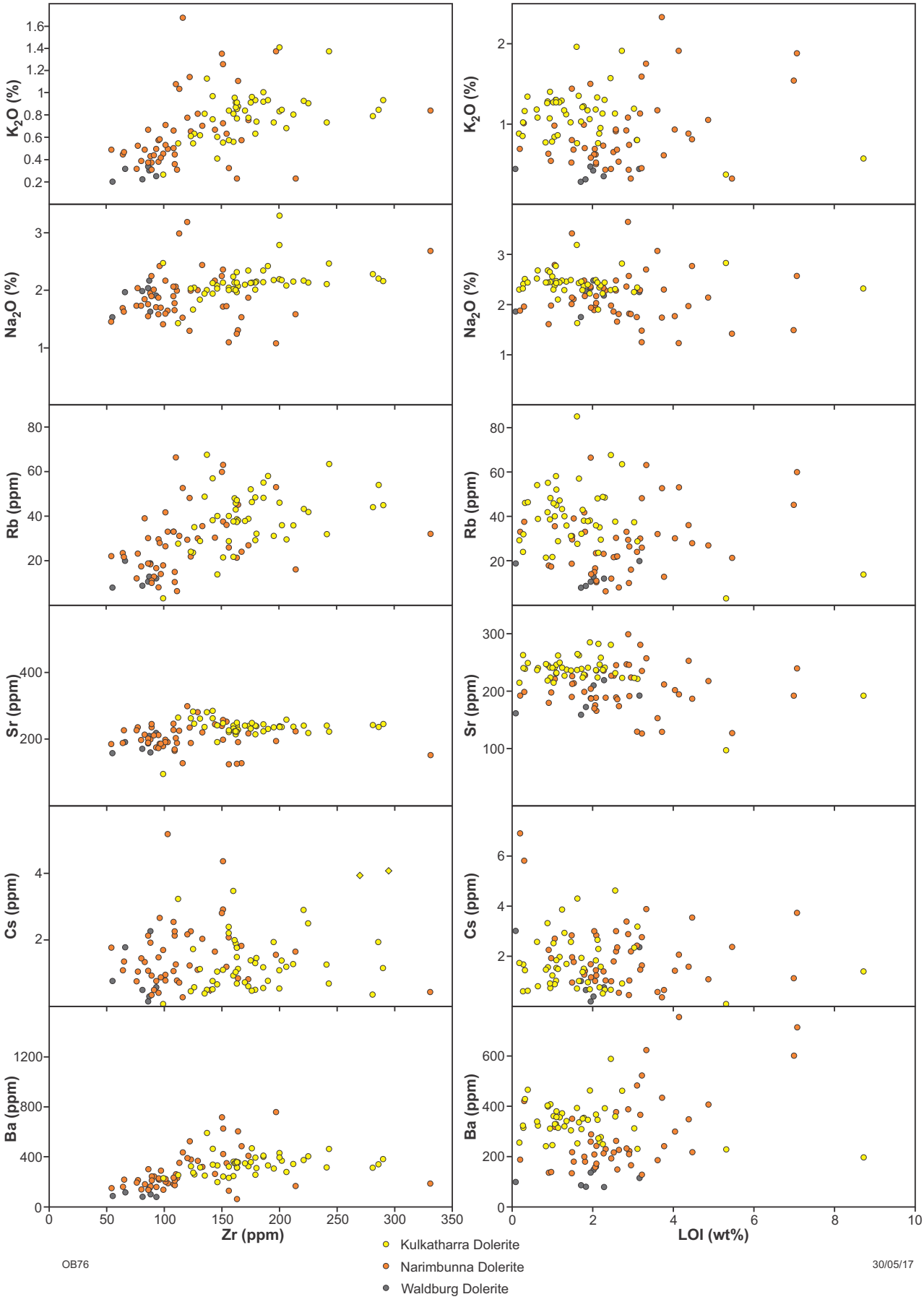

Appendix 3a

Binary variation plots of selected trace element concentrations and ratios

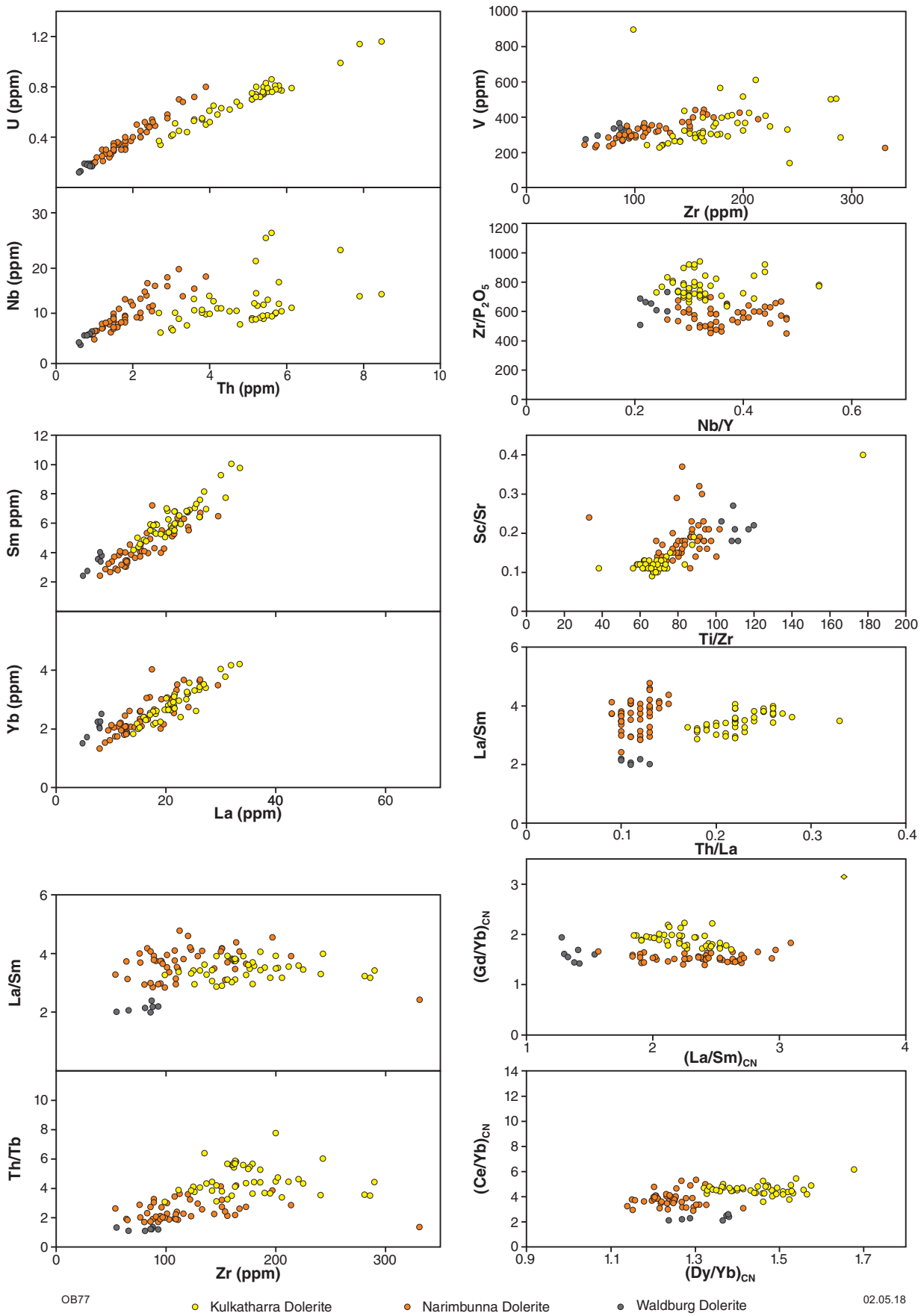

Appendix 3b

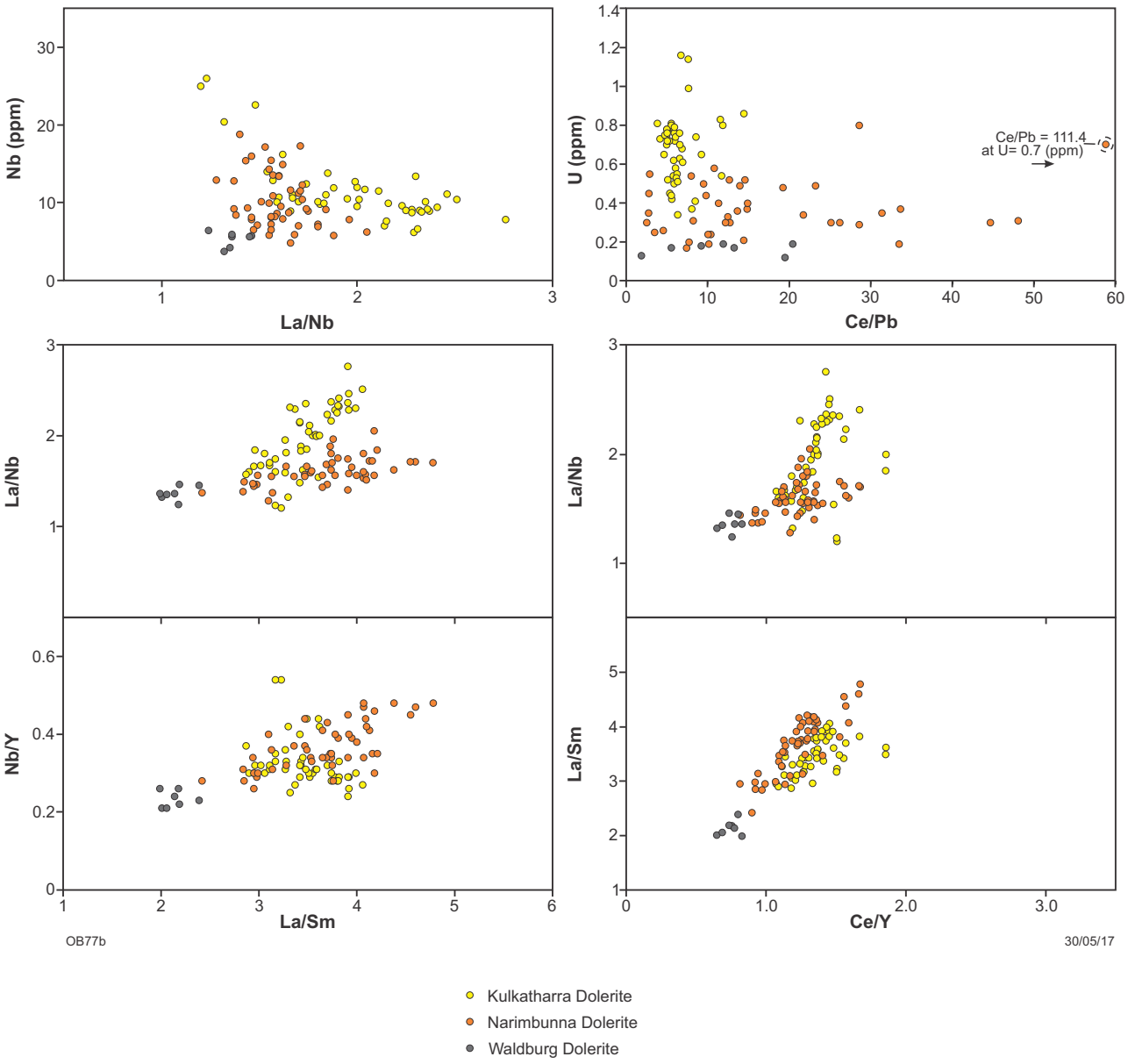
Nb (ppm)
La/Nb
U (ppm)
Ce/Pb
Ce/Pb = 111.4
at U= 0.7 (ppm)
La/Nb
La/Nb
Nb/Y
La/Sm
La/Sm
Ce/Y
OB77b
30/05/17
Kulkatharra Dolerite
Narimbunna Dolerite
Waldburg Dolerite

Appendix 4

Sm–Nd isotope analyses of whole-rock dolerite samples

Sample ID	Age (Ma)	Sm (ppm)	Nd (ppm)	$^{147}Sm/^{144}Nd$	$^{143}Nd/^{144}Nd$ measured	$^{143}Nd/^{144}Nd$ 2σ	$^{143}Nd/^{144}Nd_{(i)}$	$\varepsilon_{Nd(i)}$	T_{DM}^2 (Ga)	Method	Lab.
Kulkatharra Dolerite											
127277	1070	4.7	19.4	0.146271	0.512176	0.000004	0.511148	-2.13	1.78	IDTIMS	UQ
127298	**1067**	5.3	23.7	0.138432	0.512134	0.000007	0.511182	-1.54	1.73	MC-ICPMS	CU
180705	**1068**	5.4	23.8	0.140842	0.512145	0.000006	0.511177	-1.62	1.74	MC-ICPMS	CU
152927	1070	6.2	26.3	0.145274	0.512413	0.000071	0.511414	3.07	1.38	MC-ICPMS	CU
152927	1070	6.5	26.6	0.147000	0.512309	0.000012	0.511203	-1.04	1.70	MC-ICPMS	SU
152928	1070	6.6	28.7	0.141465	0.512214	0.000008	0.511242	-0.28	1.64	MC-ICPMS	CU
152928	1070	6.8	28.6	0.142000	0.512220	0.000012	0.511218	-0.76	1.68	MC-ICPMS	SU
156543	1070	5.3	22.3	0.146268	0.512295	0.000009	0.511290	0.65	1.57	MC-ICPMS	CU
156723	1070	5.5	24.1	0.138000	0.512100	0.000023	0.511129	-2.49	1.81	MC-ICPMS	SU
156681	**1084**	6.1	23.6	0.159552	0.512385	0.000009	0.511273	0.68	1.57	MC-ICPMS	CU
160185	1070	6.8	28.6	0.143000	0.512199	0.000011	0.511188	-1.34	1.72	MC-ICPMS	SU
160195	**1071**	5.7	24.2	0.140970	0.512159	0.000006	0.511158	-1.90	1.77	IDTIMS	UQ
160195	1070	5.6	24.5	0.138000	0.512104	0.000010	0.511129	-2.51	1.81	MC-ICPMS	SU
180706	1070	5.1	23.6	0.129000	0.512178	0.000019	0.511268	0.22	1.60	MC-ICPMS	SU
Narimbunna Dolerite											
127297	1465	5.3	22.1	0.145000	0.511969	0.000014	0.510566	-3.50	2.19	MC-ICPMS	SU
127292	1465	4.2	16.9	0.148630	0.512045	0.000005	0.510599	-2.85	2.14	IDTIMS	UQ
148983	1465	4.6	21.7	0.131828	0.511752	0.000006	0.510510	-4.58	2.28	MC-ICPMS	CU
143450	**1452**	3.8	16.2	0.143130	0.512019	0.000005	0.510655	-2.07	2.07	IDTIMS	UR
156684	1465	5.3	23.1	0.138622	0.511907	0.000006	0.510572	-3.38	2.18	IDTIMS	UQ
160183	1465	3.1	14.1	0.130000	0.511803	0.000014	0.510540	-4.00	2.23	MC-ICPMS	SU
160187	1465	4.1	19.9	0.124000	0.511706	0.000007	0.510507	-4.64	2.28	MC-ICPMS	SU
160189	**1449**	5.1	23.1	0.137413	0.511939	0.000025	0.510656	-2.14	2.08	MC-ICPMS	CU
160190	1465	3.2	14.4	0.133000	0.511848	0.000011	0.510567	-3.47	2.19	MC-ICPMS	SU
180701	1465	4.1	18.5	0.134000	0.511805	0.000019	0.510515	-4.48	2.27	MC-ICPMS	SU
180712	**1465**	2.8	13.2	0.128000	0.511838	0.000009	0.510604	-2.76	2.14	MC-ICPMS	SU
180714	**1465**	3.3	15.1	0.131000	0.511809	0.000011	0.510537	-4.05	2.24	MC-ICPMS	SU
Waldburg Dolerite											
143446	1505	3.5	12.8	0.168416	0.512385	0.000007	0.510750	1.13	1.86	MC-ICPMS	CU
143445	**1505**	2.2	7.9	0.168046	0.512440	0.000005	0.510782	1.76	1.81	IDTIMS	UR
143445	**1505**	2.8	9.9	0.168889	0.512392	0.000006	0.510701	0.16	1.94	IDTIMS	UQ
180717	1513	2.6	9.5	0.166029	0.512412	0.000006	0.510767	1.66	1.83	IDTIMS	UR
180717	1513	2.3	8.2	0.172324	0.512430	0.000007	0.510744	1.21	1.86	IDTIMS	UQ
207259	**1513**	2.8	10.1	0.166281	0.512437	0.000006	0.510788	2.08	1.80	IDTIMS	UR
206917	1513	3.2	12.0	0.163955	0.512376	0.000005	0.510753	1.39	1.85	IDTIMS	UR

NOTES: T_{DM}^2, two-stage depleted-mantle model age; 2σ, two sigma; (i), initial

Ages in bold are dated samples; other ages are inferred

Lab, laboratory: CU (John de Laeter Centre, Curtin University); UR, University of Rennes; UQ, University of Queensland; SU, Shimane University (Morris and Pirajno, 2005, 2009).

Appendix 5

Lu–Hf isotope analyses of zircon and baddeleyite from dolerite samples

Spot no.	$^{207}Pb/^{206}Pb$ date (Ma)	1s (Ma)	$^{176}Hf/^{177}Hf$ measured	$^{176}Lu/^{177}Hf$ measured	$^{176}Yb/^{177}Hf$ measured	$^{176}Hf/^{177}Hf_{initial}$	1s	$\varepsilon_{Hf(i)}$	1s	T_{DM} (Ga)
Kulkatharra Dolerite										
GSWA 156750										
Zircon										
1.2	1110	63	0.282083	0.000923	0.02990	0.282064	0.000074	-0.5	2.6	1.64
3.1	1061	48	0.282416	0.000927	0.02894	0.282397	0.000071	10.2	2.5	1.18
4.1	1045	72	0.282449	0.001165	0.03664	0.282426	0.000110	10.9	3.9	1.14
4.2	1056	66	0.282091	0.001214	0.03401	0.282067	0.000094	-1.6	3.3	1.65
5.2	1157	59	0.282261	0.000859	0.02905	0.282242	0.000160	6.9	5.6	1.39
6.1	1089	32	0.282394	0.001285	0.04487	0.282368	0.000096	9.8	3.4	1.22
6.2	1086	26	0.282163	0.001489	0.05125	0.282133	0.000100	1.4	3.5	1.56
7.1	1026	36	0.282218	0.001000	0.03365	0.282199	0.000110	2.4	3.9	1.46
7.2	1071	34	0.282225	0.001001	0.03637	0.282205	0.000064	3.6	2.2	1.45
8.1	1106	119	0.282200	0.001216	0.03348	0.282175	0.000070	3.4	2.5	1.49
9.1	1106	54	0.282184	0.001119	0.03705	0.282161	0.000140	2.9	4.9	1.51
10.1	1025	60	0.282430	0.001124	0.03718	0.282408	0.000080	9.8	2.8	1.17
11.1	1099	22	0.282367	0.001929	0.05704	0.282327	0.000110	8.6	3.9	1.28
14.1	1098	25	0.282284	0.001766	0.05229	0.282247	0.000057	5.8	2.0	1.40
15.1	1084	51	0.282164	0.001039	0.03253	0.282143	0.000086	1.7	3.0	1.54
17.1	1061	53	0.282293	0.001093	0.04094	0.282271	0.000250	5.8	8.8	1.36
18.1	1093	51	0.281975	0.001274	0.04353	0.281949	0.000180	-4.9	6.3	1.81
19.1	1029	95	0.282189	0.000690	0.01990	0.282176	0.000078	1.7	2.7	1.49
GSWA169011										
Zircon										
1.1	2946	5	0.281177	0.001266	0.03370	0.281106	0.000140	7.4	4.9	2.91
2.1	2944	6	0.280807	0.001593	0.04479	0.280717	0.000078	-6.4	2.7	3.45
3.1	1995	13	0.281334	0.000400	0.00926	0.281319	0.000026	-6.9	0.9	2.64
4.1	1994	11	0.281279	0.000298	0.01075	0.281268	0.000040	-8.8	1.4	2.70
5.1	1997	8	0.281384	0.000845	0.02869	0.281352	0.000018	-5.7	0.6	2.60
6.1	1083	7	0.282385	0.004062	0.16648	0.282302	0.000057	7.4	2.0	1.33
6.2	1064	8	0.282224	0.004048	0.16744	0.282143	0.000040	1.3	1.4	1.58
7.1	1069	7	0.282329	0.007612	0.26223	0.282176	0.000079	2.6	2.8	1.58
8.1	1071	6	0.282311	0.006041	0.22650	0.282189	0.000063	3.1	2.2	1.53
Baddeleyite										
1.1	1065	24	0.282210	0.000710	0.02105	0.282196	0.000029	3.2	1.0	1.46
2.1	1064	48	0.282240	0.001009	0.02966	0.282220	0.000100	4.0	3.5	1.43
3.1	1096	35	0.282117	0.001224	0.04025	0.282092	0.000059	0.2	2.1	1.61
GSWA 156602										
Zircon										
2.1	1059	8	0.282581	0.007860	0.30243	0.282424	0.000120	11.1	4.2	1.16
5.1	1079	3	0.282414	0.007376	0.29748	0.282264	0.000048	5.9	1.7	1.43
10.1	1068	7	0.282612	0.008922	0.46736	0.282433	0.000079	11.6	2.8	1.15
11.1	1071	4	0.282698	0.011510	0.56930	0.282466	0.000044	12.9	1.5	1.09
13.1	1057	5	0.282489	0.008202	0.41328	0.282326	0.000033	7.6	1.2	1.33
14.1	1082	8	0.282560	0.007495	0.37665	0.282407	0.000057	11.1	2.0	1.18
15.1	1073	18	0.282552	0.007218	0.36506	0.282406	0.000045	10.8	1.6	1.19
16.1	1072	4	0.282638	0.011544	0.50822	0.282405	0.000052	10.8	1.8	1.21
17.1	1078	11	0.282379	0.005895	0.28205	0.282259	0.000031	5.7	1.1	1.42
18.1	1067	5	0.282483	0.006393	0.34447	0.282355	0.000019	8.9	0.7	1.27
19.1	1085	13	0.282416	0.005998	0.31451	0.282293	0.000039	7.1	1.4	1.36
20.1	1083	12	0.282439	0.007016	0.34293	0.282296	0.000038	7.1	1.3	1.37

Spot no.	$^{207}Pb/^{206}Pb$ date (Ma)	1s (Ma)	$^{176}Hf/^{177}Hf$ measured	$^{176}Lu/^{177}Hf$ measured	$^{176}Yb/^{177}Hf$ measured	$^{176}Hf/^{177}Hf_{initial}$	1s	$\varepsilon_{Hf(i)}$	1s	T_{DM} (Ga)
Narimbunna Dolerite										
GSWA156751										
Zircon										
1.1	1478	9	0.281901	0.003285	0.14026	0.281809	0.00003	-1.2	1.1	2.02
3.1	1459	5	0.281869	0.002909	0.12905	0.281789	0.000011	-2.4	0.4	2.05
5.1	1471	6	0.281903	0.003705	0.15844	0.281800	0.000012	-1.7	0.4	2.04
6.1	1455	6	0.281825	0.002313	0.09146	0.281761	0.000007	-3.5	0.2	2.08
7.1	1466	4	0.281823	0.002621	0.10730	0.281750	0.000034	-3.6	1.2	2.10
8.1	1451	4	0.281811	0.003828	0.14195	0.281706	0.000013	-5.5	0.5	2.19
9.1	1463	5	0.281849	0.003305	0.15210	0.281758	0.000017	-3.4	0.6	2.10
10.1	1463	5	0.281805	0.002206	0.08083	0.281744	0.000008	-3.9	0.3	2.10
11.1	1455	5	0.281880	0.003557	0.12411	0.281782	0.00002	-2.7	0.7	2.07
13.1	1465	4	0.281862	0.002348	0.10024	0.281797	0.000025	-2.0	0.9	2.03
15.1	1465	4	0.281879	0.002779	0.10497	0.281802	0.000022	-1.8	0.8	2.02
16.1	1460	4	0.281853	0.002172	0.08934	0.281793	0.000019	-2.2	0.7	2.03
17.1	1465	4	0.282050	0.004699	0.21256	0.281920	0.000026	2.4	0.9	1.88
Baddeleyite										
1.1	1446	61	0.281880	0.000844	0.03200	0.281857	0.000048	-0.3	1.7	2.23
2.1	1482	70	0.281836	0.000812	0.02964	0.281813	0.000054	-1.0	1.9	2.30
3.1	1549	48	0.281971	0.000904	0.03456	0.281945	0.000056	5.2	2.0	1.96
4.1	1607	53	0.281960	0.000698	0.02522	0.281939	0.000035	6.3	1.2	1.94
5.1	1451	25	0.281853	0.000869	0.03654	0.281829	0.000068	-1.1	2.4	2.29
6.1	1444	22	0.282007	0.000814	0.03581	0.281985	0.000064	4.2	2.2	1.94
7.1	1389	60	0.281776	0.000447	0.01722	0.281764	0.000057	-4.8	2.0	2.48
8.1	1470	35	0.281974	0.000861	0.03008	0.281950	0.000051	3.6	1.8	2.00
9.1	1494	51	0.281894	0.000868	0.02817	0.281869	0.000087	1.3	3.0	2.17
GSWA143450										
Zircon										
2.1	1445	7	0.282021	0.005039	0.19340	0.281883	0.000010	0.6	0.4	2.17
3.1	1452	11	0.281988	0.004115	0.15445	0.281875	0.000025	0.5	0.9	2.18
5.1	1458	9	0.282063	0.005997	0.22227	0.281898	0.000012	1.4	0.4	2.13
6.1	1452	9	0.281957	0.003798	0.15025	0.281853	0.000013	-0.3	0.5	2.23
8.1	1455	8	0.281951	0.002795	0.08962	0.281874	0.000019	0.5	0.7	2.18
11.1	1438	11	0.282033	0.004113	0.14346	0.281921	0.000029	1.8	1.0	2.09
12.1	1445	7	0.282089	0.005538	0.21762	0.281938	0.000022	2.6	0.8	2.05
13.1	1459	9	0.281947	0.001711	0.04898	0.281900	0.000022	1.5	0.8	2.12
16.1	1475	13	0.281977	0.002289	0.10402	0.281913	0.000032	2.4	1.1	2.08
Baddeleyite										
1.1	1447	18	0.281820	0.000821	0.02227	0.281798	0.000042	-2.4	1.5	2.00
2.1	1504	24	0.281829	0.000664	0.01977	0.281810	0.000048	-0.6	1.7	1.98
3.1	1359	47	0.281864	0.000881	0.02489	0.281841	0.000044	-2.8	1.5	1.95
5.1	1437	52	0.281851	0.000547	0.01709	0.281836	0.000058	-1.2	2.0	1.95
6.1	1513	39	0.281860	0.000819	0.02219	0.281837	0.000024	0.5	0.8	1.95
9.1	1443	18	0.281776	0.001107	0.03855	0.281746	0.000033	-4.3	1.2	2.08
10.2	1462	14	0.281638	0.001161	0.03686	0.281606	0.000077	-8.8	2.7	2.27
11.1	1448	10	0.281778	0.000495	0.01856	0.281764	0.000022	-3.5	0.8	2.04
14.1	1423	60	0.281447	0.000531	0.01243	0.281433	0.000036	-15.8	1.3	2.49
16.1	1374	34	0.281820	0.001087	0.03145	0.281792	0.000066	-4.2	2.3	2.02
18.1	1436	28	0.281895	0.000624	0.01942	0.281878	0.000049	0.3	1.7	1.89
19.1	1478	16	0.281845	0.000807	0.02382	0.281822	0.000150	-0.8	5.3	1.97
21.1	1414	63	0.281773	0.000446	0.01206	0.281761	0.000047	-4.4	1.6	2.05
22.1	1482	22	0.281768	0.000342	0.01095	0.281758	0.000073	-3.0	2.6	2.05
23.1	1444	11	0.281975	0.000933	0.03304	0.281950	0.000110	3.0	3.9	1.79
24.1	1455	21	0.281998	0.000480	0.01579	0.281985	0.000110	4.5	3.9	1.74

Spot no.	$^{207}Pb/^{206}Pb$ date (Ma)	1s (Ma)	$^{176}Hf/^{177}Hf$ measured	$^{176}Lu/^{177}Hf$ measured	$^{176}Yb/^{177}Hf$ measured	$^{176}Hf/^{177}Hf_{initial}$	1s	$\varepsilon_{Hf(i)}$	1s	T_{DM} (Ga)
Waldburg Dolerite GSWA143445										
Zircon										
1.1	1529	11	0.281947	0.001111	0.04011	0.281915	0.000012	3.7	0.4	1.84
3.1	1496	13	0.281981	0.002098	0.07162	0.281922	0.000010	3.2	0.4	1.84
4.1	1507	6	0.282018	0.001715	0.06534	0.281969	0.000012	5.1	0.4	1.77
7.1	1494	19	0.281997	0.001228	0.03702	0.281962	0.000014	4.6	0.5	1.78
10.1	1494	41	0.282009	0.001605	0.06247	0.281964	0.000010	4.6	0.4	1.78
11.1	1500	7	0.282049	0.002685	0.09615	0.281973	0.000011	5.1	0.4	1.77
12.1	1503	8	0.282050	0.001654	0.06782	0.282003	0.000010	6.2	0.4	1.72
17.1	1514	7	0.282062	0.002169	0.08189	0.282000	0.000013	6.3	0.5	1.73
23.1	1493	10	0.281987	0.001627	0.05548	0.281941	0.000011	3.8	0.4	1.81
24.1	1500	9	0.282020	0.002054	0.06873	0.281962	0.000010	4.7	0.3	1.78
25.1	1490	8	0.282064	0.002244	0.07916	0.282001	0.000007	5.8	0.2	1.73
26.1	1500	6	0.282093	0.002594	0.08973	0.282019	0.000015	6.7	0.5	1.71

NOTES: Initial $^{176}Hf/^{177}Hf$ calculated using the ^{176}Lu decay constant ($1.867 \times 10^{-11}yr^{-1}$) of Scherer et al., 2001

$\varepsilon_{Hf(i)}$ values calculated using the decay constant of Scherer at al. (2001) and CHUR values of Blichert-Toft and Albarède (1997)

RECORD 2018/4

A NEW MESOPROTEROZOIC MAFIC INTRUSIVE EVENT IN THE CAPRICORN OROGEN

Blay et al.

This Record is published in digital format (PDF) and is available as a free download from the DMIRS website at <www.dmp.wa.gov.au/GSWApublications>.

Further details of geological products produced by the Geological Survey of Western Australia can be obtained by contacting:

Information Centre
Department of Mines, Industry Regulation and Safety
100 Plain Street
EAST PERTH WESTERN AUSTRALIA 6004
Phone: +61 8 9222 3459 Fax: +61 8 9222 3444
www.dmp.wa.gov.au/GSWApublications